Banner Cloud Dynamics at the Matterhorn: From Idealized Simulations to Real-World Observations

Dissertation
zur Erlangung des Grades
"Doktor der Naturwissenschaften"

am Fachbereich Physik, Mathematik und Informatik
der Johannes Gutenberg-Universität Mainz

Marius Levin Thomas
geboren in Wiesbaden-Dotzheim

Mainz, den 04.04.2025

Tag der mündlichen Prüfung: 11.11.2025

Abstract

Banner clouds are a phenomenon that occur on the leeward side of steep mountains or sharp ridges on otherwise cloud free days. Investigating their formation mechanisms helps to improve our understanding of flow response in complex orography. Previous studies have identified key mechanisms and conducive atmospheric conditions primarily based on theoretical considerations and idealized simulations. However, it remains unclear to what extent these findings are valid in complex terrain under realistic atmospheric conditions. This thesis aims to bridge the gap between idealized model experiments and the real-world conditions by investigating the key mechanisms of banner cloud formation at the Matterhorn in the Swiss Alps. Therefore, Large-Eddy Simulations with a progressive transition from idealized to fully realistic Matterhorn orography are combined with observations from the dedicated MatterHEX field campaign. MatterHEX provides the first systematic observations of banner cloud conditions, including radiosonde upwind profiles, Doppler lidar scans of the lee-side flow, and webcam footage capturing cloud evolution. To ensure consistency in the direct comparison, the model inflow profiles were tuned to match the ambient flow to the radiosonde observations. The simulations show that increased terrain complexity alters flow symmetry, yet strong lee-side upwelling is still a predominant flow feature. The upwelling is no longer confined to the leeward side, but extends to the spanwise slopes, where most parcels ascend before entering the banner cloud. Weak stratification in the lee emerges as an important prerequisite for banner cloud formation at the Matterhorn, either reflecting ambient conditions or turbulence induced by terrain-flow interaction at high wind speeds or wind shear. The direct comparison of observed and simulated lidar scans during two contrasting banner cloud episodes confirms lee-side separation associated with recirculating flow and strong upwelling as the key mechanisms. Furthermore, a classification of all observed ambient flow conditions using a theoretical flow regime framework reveals that the necessary lee-side flow separation occurs more frequently than the actual banner cloud observation would suggest. These findings confirm that previous results from model-based investigations are applicable under realistic conditions, at least at a steep mountain like the Matterhorn. Moreover, lee-side separation seems to be a robust flow response that may occur under a wide range of ambient flow conditions, promoting banner cloud occurrence given suitable moisture conditions. This thesis highlights the value of combining high-resolution simulations with targeted observations to investigate turbulent flows in complex terrain.

Contents

List of Publications and Manuscripts

- Thomas, M. L., and V. Wirth, 2023: Sensitivity of Banner Cloud Formation to Orography and the Ambient Atmosphere: Transition from Idealized to More Realistic Scenarios. J. Atmos. Sci., 80, 2653–2668, https://doi.org/10.1175/JAS-D-23-0106.1

  Contributions: MLT conceptualized, drafted and revised the manuscript, carried out the data analysis, created all figures, and maintained the data. VW gave guidance throughout the writing process and helped review the manuscript.

- Thomas, M. L., Hoch, S. W., Huwald, H., Lehning, M., van Schaik, B. J. A., Rentel, D. S., Imbert, P., and V. Wirth: Banner Cloud Formation at the Matterhorn: Measurements versus Large-Eddy Simulations. J. Atmos. Sci. [Under Review]

  Contributions: MLT conceptualized, drafted and revised the manuscript, carried out the data analysis, created all figures, and maintained the data. SWH and VW gave guidance throughout the writing process and helped review the manuscript. HH, MH, and BJAvS provided feedback on the paper.

- Hoch, S. W., Thomas, M. L., Huwald, H., Lehning, M., van Schaik, B. J. A., Rentel, D. S., Imbert, P., and V. Wirth: The MatterHEX Experiment – Investigating Atmospheric Flow Patterns in Highly Complex Terrain Related to Banner Cloud Formation. J. Atmos. Sci. [Under Review]

  Contributions: SWH and MLT conceptualized and drafted the manuscript. MLT carried out the data analysis, created the figures 2, 3, 4, 5, 7, 8, 9, 11., and maintained the data. SWH created the figures 1 and 6. VW gave guidance throughout the writing process and helped review the manuscript. HH, MH, and BJAvS provided feedback on the paper.

Sections and figures from the publications and manuscripts have been renumbered for integration into the thesis.

1 Introduction

1.1 Flow Past Mountains

Mountainous regions cover a significant portion of the Earth's surface and play an important role in atmospheric dynamics and exchange processes. Their interaction with atmospheric flow generates diverse meteorological phenomena that influence weather and climate across multiple scales (Teixeira et al., 2016). On the synoptic scale, mountains modify air mass advection and generate Rossby waves (Smith, 1979). At meso- and microscales, mountains generate regional and local wind systems, playing an important role in determining the dynamical and thermodynamical atmospheric structure (De Wekker & Kossmann, 2015). Their effects can be further categorized as active or passive (Geiger, 2013). Active effects arise from diurnal thermal and radiative exchanges, leading to differential heating over complex terrain. This generates thermally induced flows, particularly in fair-weather conditions with weak synoptic forcing (Whiteman, 2000). These flows impact horizontal transport and vertical exchange of heat, mass, moisture, and pollutants on the scale of individual slopes to entire mountain ranges through along-valley breezes, cross-valley wind systems, and circulations between plains and mountain massifs (Whiteman, 2000; Serafin et al., 2018).

The relevant mechanisms examined in this thesis are related to passive, mechanically driven interactions that lead to various dynamically forced flows (De Wekker & Kossmann, 2015). These include flow blocking with cold pool formation, barrier jets, gap winds, wind speed increases at crests, downslope windstorms, mountain waves and lee waves further downstream, turbulent eddies and wakes, and flow separation on the windward or leeward side (Whiteman, 2000). Some of these phenomena have significant impact: strong downslope windstorms can cause severe damage to infrastructure or mountain forest and enhance wildfire risk, while mountain wave breaking and lee wave rotors pose hazards to aviation (Whiteman, 2000; Teixeira et al., 2016).

The specific flow response depends on three key parameters: the stratification of the incoming flow, the wind speed of the incoming flow, and the mountain's topography. Stably stratified flow resists lifting over the mountain, increasing the likelihood of blocking and deflection around the mountain (Whiteman, 2000). In contrast, strong winds and a weak stratification promote flow separation on the leeward side of steep mountains, forming turbulent wakes with enhanced mixing (Baines, 1995; Whiteman, 2000). Flow separation is often related to a recirculating flow with reversed wind direction due to an adverse pressure gradient (Ambaum & Marshall, 2005).

Observations from laboratory experiments with a two-dimensional hill (Baines & Hoinka, 1985) and linear theory (Ambaum & Marshall, 2005) provide a theoretical framework that utilizes the steepness of the mountain and the flow conditions to predict lee-side flow separation through the non-dimensional mountain aspect ratio $\mathscr{A}$ and the inverse Froude number $\mathscr{N}$ (Baines, 1995):

$$\mathscr{A} := \frac{h_0}{A_d} \tag{1.1}$$

$$\mathscr{N} := \frac{N \cdot h_0}{U_0} \tag{1.2}$$

Here, h_0 is the mountain height, A_d is the lee-side mountain half-width, N the Brunt-Väisälä frequency, and U_0 the wind speed.

This framework allows a systematic classification of flow regimes. Baines (1995) distinguishes between three flow regimes: no separation, lee-side separation and post-wave separation. No separation is expected for a weakly stratified flow with high wind speeds (small $\mathscr{N}$) past a gentle mountain (small $\mathscr{A}$). In contrast, for a much steeper mountain (large $\mathscr{A}$), the flow separates at the summit and a recirculating flow occurs on the leeward side. For increased stratification and smaller wind speeds (large $\mathscr{N}$) the occurrence of mountain waves and the resulting restoring forces suppress the separation on the leeward slope. As a result, the flow closely follows the terrain, strong downslope winds can occur, and the location of flow separation shifts downstream. This is called post-wave separation and is observed for both gentle and steep mountains (Baines, 1995). These dependencies and the corresponding flow regimes are summarized in a regime diagram by Baines (1995), as shown in adapted form in Figure 3.2.

In addition to both scaling parameters, surface roughness and the distinct shape of the mountain strongly impact flow separation. According to linear theory by Ambaum & Marshall (2005), surface friction decelerates the flow, promoting flow separation. Numerical simulations confirm that increased surface roughness enhances separation, even for smaller mountain aspect ratios in neutrally stratified flows (e.g., Wood, 1995; Sogachev et al., 2004). Moreover, the resulting adverse pressure gradient and wind shear in the viscous boundary layer generate vorticity, which separates from the surface and is transported downstream in a turbulent, unsteady wake. This friction-driven flow separation and vortex shedding particularly occur at salient edges (Scorer, 1955). Another mechanism for lee-side vortex generation is the tilting of horizontally oriented vorticity, generated baroclinically at mountain edges due to isentrope deformation in a stably stratified flow (Smolarkiewicz & Rotunno, 1989; Smith, 1989; Rotunno & Smolarkiewicz, 1991; Rotunno et al., 1999; Epifanio & Rotunno, 2005).

1.2 Banner Cloud Formation

Dynamically forced flows often give rise to different intriguing cloud formations, including Foehn cloud walls, rotor clouds, mountain wave clouds, billow clouds, cap clouds, and banner clouds (Whiteman, 2000). Among these, this thesis focuses on banner clouds, which form, rather counter-intuitively, in the lee of steep mountains or sharp ridges, resembling a banner flying in the wind. They are most commonly observed under fair-weather conditions with minimal cloud cover (Glickman, 2000). Figure 1.1 shows an exemplary banner cloud at the Matterhorn in the Swiss Alps. A formal definition was established by Schween et al. (2007) based on webcam observations at the Zugspitze in the Bavarian Alps. They defined banner clouds as forming exclusively on the leeward side, while the windward side remains cloud-free. Additionally, they must be persistent, non-convective, and not consist of blowing snow. Further in-situ measurements by (Wirth et al., 2012) revealed that banner clouds at the Zugspitze follow a diurnal cycle and preferentially occur under south-easterly winds, with little sensitivity to wind speed. These observations were later validated through simulations incorporating realistic orography of the Zugspitze by (Prestel, 2018).

FIGURE 1.1: Webcam image of a banner cloud on the Matterhorn at 1652 UTC 29 September 2023 during the MatterHEX field campaign. The wind is blowing from the right to the left.

The formation of banner clouds indicates that lee-side vertical displacement dominates over the lifting on the windward side. To better understand the physical mechanisms behind banner cloud formation, a range of modeling and experimental studies have been conducted in the past decades. These studies indicate that banner clouds are closely linked to flow separation associated with a recirculating flow and strong upwelling on the leeward side of steep mountains.

In a neutral or weakly stratified flow, the lee-side separation wake exhibits considerable unsteadiness, with asymmetric flow patterns dominated by alternating vortices shedding downstream (Baines, 1995). However, time-averaged results from both laboratory experiments (e.g., Hunt & Snyder, 1980; Martinuzzi & AbuOmar, 2003) and idealized simulations (e.g., Smolarkiewicz & Rotunno, 1989; Voigt & Wirth, 2013; Prestel & Wirth, 2016; Wirth et al., 2020) with pyramid-shaped mountains and azimuthally symmetric hills consistently show two counterrotating vortices in the horizontal plane and an overturning eddy in the vertical plane. These features can be interpreted as footprints of a single three-dimensional bow-shaped vortex, which is associated with strong upwelling close to the leeward mountain slope (Voigt & Wirth, 2013; Wirth et al., 2020). Further sensitivity experiments by Wirth et al. (2020), with a neutrally stratified flow below the summit of a pyramid-shaped mountain and stable stratification above, showed that the lee-side flow geometry remains largely independent of flow speed. However, wind shear causes the bow-shaped vortex to tilt and separate into two branches. As a result, the region of strong upwelling shifts further downstream and is confined to a narrow region (Wirth et al., 2020). Under suitable moisture conditions, this vertical motion lifts air parcels to the condensation level, forming a cloud in the immediate lee at the summit: the banner cloud (Reinert & Wirth, 2009).

While cloud formation is ultimately a moist process, recent modeling studies have shown that the Lagrangian vertical displacement (Δz) of air parcels — a purely dynamical quantity — serves as a reliable proxy for banner cloud occurrence.

Reinert & Wirth (2009) demonstrated that banner cloud formation at a pyramid-shaped mountain coincides with a pronounced windward-leeward asymmetry in Δz, with a plume of particularly large values in the immediate lee at the summit. This simulated Δz plume showed a high structural similarity to the simulated moist banner cloud. Accordingly, banner cloud formation was directly related to the adiabatic cooling of air parcels in the dynamically forced upwelling on the leeward side, while moist-microphysics (e.g., latent heat release) only plays a minor role (Reinert & Wirth,

2009). For this reason, the numerical simulations in this thesis are also limited to dry flows. Schappert & Wirth (2015) found that parcels entering the banner cloud predominantly flow around the pyramid before they experience the strong uplift on the leeward side. A systematic investigation of flow conditions conducive to banner cloud formation with cosine-shaped mountain by Prestel & Wirth (2016) revealed that they preferentially occur for a weakly stratified flow past a steep mountain. This result supports the idea that banner cloud formation is closely linked to lee-side flow separation induced by surface friction (see section 1.1).

1.3 Research Objectives

Previous observational and numerical studies have provided insight into the key mechanisms and preferred flow conditions for banner cloud formation. These findings suggest that banner clouds can be understood as a visible manifestation of lee-side separation and vortex dynamics, associated with recirculating flow and strong upwelling on the leeward side of a steep mountain under weakly stratified flow. However, existing research is primarily based on idealized Large-Eddy Simulations (LES), leaving uncertainty about the validity of these findings under real-world conditions with complex orography.

This thesis aims to bridge the gap between theoretical and idealized considerations and their verification with observations. The overarching objective is to evaluate the robustness of previously identified key mechanisms of banner cloud formation under realistic conditions. To this end, Large-Eddy Simulations (LES) using the EULAG model with realistic orography of the Matterhorn are compared with observations from the MatterHorn EXperiment (MatterHEX). Details of the EULAG model and the specific configuration used in this work are given in Appendix A. MatterHEX provides the first systematic observations of upwind flow conditions from radiosondes, leeside flow patterns captured by a Doppler lidar, and the evolution of banner clouds monitored by webcams. The Matterhorn is particularly well-suited for the evaluation – not only is it renowned for its iconic banner clouds (see Fig. 1.1), but its pyramidal summit shape closely resembles the isolated mountain forms used in prior laboratory experiments and idealized studies. At the same time, its surrounding terrain introduces more complexity that is expected to alter local flow structures.

The combination of high-resolution modeling and dedicated in-situ observations offers the opportunity to verify the reliability of model-based results on banner cloud formation mechanisms under realistic conditions. In this way, the synergetic use of LES and observations enables a more comprehensive understanding of banner cloud formation in complex terrain.

The investigation follows a three-step strategy. First, chapter 2 presents a sensitivity study using LES with idealized inflow profiles to examine how increasing orographic complexity affects the key mechanisms of banner cloud formation. Flow structures are systematically compared across simulations with model orography ranging from an idealized pyramid-shaped mountain to the Matterhorn summit protruding from a flat plain, and finally to the fully realistic Matterhorn orography. Particular attention is given to changes in regions of strong upwelling, vortex structures, and their sensitivity to wind shear, as previously noticed for an idealized pyramid-shaped mountain by Wirth et al. (2020). In addition, backward trajectory analysis is used to identify differences in the dominant parcel pathways leading into the banner cloud, by categorizing them based on their position relative to the summit during the uplift phase along the mountain slopes. For the fully realistic Matterhorn orography, the study also evaluates how ambient flow conditions with a neutral boundary layer below the summit affect banner cloud formation.

In the next step, chapter 3 evaluates the capability of modern Doppler lidar techniques to observe the relevant lee-side flow features during banner cloud episodes in high-altitude, complex

terrain. Furthermore, the geometry of the Matterhorn, together with radiosonde observations of wind profiles and stratification, is used to estimate how frequently lee-side flow separation — the necessary condition for banner cloud formation — occurs, applying the theoretical flow regime framework developed by Baines (1995).

Subsequently, chapter 4 presents a case study that integrates observations from two contrasting banner cloud episodes with semi-idealized LES, allowing a systematic comparison to assess the real-world relevance of model-based results. To ensure consistency, model inflow conditions are tuned so that time-averaged ambient flow profiles represent upwind conditions derived from radiosonde measurements. Lidar retrievals are optimized using a combination of conventional threshold filtering and a density-based clustering algorithm, followed by the computation of time-averaged composites. In addition, model-based radial velocities are derived from the time-averaged flow fields to allow direct comparison with observed lidar data. These lidar scan retrievals are further contextualized into the fully three-dimensional ambient flow conditions provided by the LES. Furthermore, the Lagrangian vertical displacement used as a banner cloud proxy is evaluated in terms of structural similarity to banner cloud observations via webcam photography.

Finally, the key findings are summarized and conclusions are drawn in chapter 5.

2 Sensitivity of Banner Cloud Formation to Orography and the Ambient Atmosphere: Transition From Idealized to More Realistic Scenarios

This chapter has previously been published:

Thomas, M. L., and V. Wirth, 2023: Sensitivity of Banner Cloud Formation to Orography and the Ambient Atmosphere: Transition from Idealized to More Realistic Scenarios. J. Atmos. Sci., 80, 2653–2668, https://doi.org/10.1175/JAS-D-23-0106.1

2.1 Abstract

Banner clouds are clouds in the lee of steep mountains or sharp ridges on otherwise cloud-free days. Previous studies investigated various aspects of banner cloud formation in numerical simulations, most of which were based on idealized orography and a neutrally stratified ambient atmosphere. The present study extends these simulations in two important directions by 1) examining the impact of various types of orography ranging from an idealized pyramid to the realistic orography of Mount Matterhorn, and 2) accounting for an ambient atmosphere that turns from neutral to stably stratified below the mountain summit. Not surprisingly, realistic orography introduces asymmetries in the spanwise direction. At the same time, banner cloud occurrence remains associated with a coherent area of strong uplift, although this region does not have to be located exclusively in the lee of the mountain any longer. In the case of Mount Matterhorn with a westerly ambient flow, a large fraction of air parcels rises along the southern face of the mountain, before they reach the lee and are lifted into the banner cloud. The presence of a shallow boundary layer with its top below the mountain summit introduces more complex behavior compared to a neutrally stratified boundary layer; in particular, it introduces a dependence on wind speed, because strong wind is associated with strong turbulence that is able to raise the boundary layer height and, thus, facilitates the formation of a banner cloud.

2.2 Introduction

Banner clouds are clouds in the lee of steep mountains or sharp ridges on otherwise cloud-free days (Glickman, 2000). They appear like a banner attached to the leeside face of the mountain flapping in the wind, hence their name (Schween et al., 2007; Wirth et al., 2012). Their formation requires a region of strong uplift on the leeward side of the mountain; given suitable moisture

conditions, this may then lead to banner cloud formation (Voigt & Wirth, 2013). Banner clouds are noteworthy, because flow past orography usually implies uplift and, hence, cloud formation on the windward rather than the leeward side of the orography. This suggests that they occur under special conditions only, which would explain why they are a fairly rare phenomenon. Prestel & Wirth (2016) have argued that favourable conditions for banner cloud formation formation include a rather steep mountain and weak stratification of the ambient atmosphere.

During the past decades aspects of banner cloud formation were investigated with the help of numerical simulations (Voigt & Wirth, 2013; Schappert & Wirth, 2015; Prestel & Wirth, 2016; Wirth et al., 2020). In all these studies, the orography was represented by a square Pyramid with a vertical aspect ratio of around 1 protruding from a plain. In addition, in most of these studies the ambient atmosphere was chosen to be neutrally stratified up to the summit of the orography. On the one hand this allowed the authors to clarify a number of fundamental questions regarding key mechanisms and preferred flow conditions of banner cloud formation; on the other hand, it remained unclear to what extent the results depended on the idealized nature of the model configuration.

This state of affairs motivates the present study, in which we consider flow past realistic rather than idealized orography. In addition, we also account for a shallow bounday layer with its top lying below the summit of the mountain, since this is a situation that may occur in nature. The geographic region that we consider is the Mount Matterhorn in the Swiss Alps including its near environment. The Matterhorn is one of the most suitable mountains in the Alps to study the phenomenon, as it features a relatively frequent occurrence of banner clouds with sometimes near-iconic appearance (e.g., Fig. 1 in Wirth et al., 2020). We will carry through Large Eddy Simulations similar to previous studies, except that the use of realistic orography requires a considerably larger model domain, which makes the simulations computationally more expensive. In addition we consider two configurations with more idealized orography: the top-most part of the Matterhorn orography protruding from a flat surface, and a quadratic Pyramid protruding from a flat surface. The former represents an intermediate stage, allowing us to study the transition from a highly idealized Pyramid to the realistic Matterhorn orography. We will investigate the differences of the flow associated with these three orographies in order to identify features that are generic to any steep mountain and distinguish them from features that are special due to particular properties of the orography. We pay particular attention to the existence and properties of leeward vortices, to the windward-leeward asymmetry in uplift, and to the flow path of streamlines reaching the banner cloud. Another focus will be on the question to what extent the stratification of the ambient atmosphere influences banner cloud formation, and whether the mountain, in turn, has an impact on the stratification. We intend to learn to what extent the results from previous studies with idealized model configurations carry over to more realistic scenarios.

The paper is organized as follows. First, in section 2.3 we present the setup of the numerical model. Subsequently, our diagnostic tools will be introduced in section 2.4, and the results of our analysis are presented in section 2.5. Finally, section 2.6 provides a summary and our conclusions.

2.3 Numerical Model and Model Configuration

We simulate three-dimensional turbulent flow of dry air in a non-rotating atmosphere. In our earlier work, we used for this purpose the nonhydrostatic anelastic version of the EULAG model (Prusa et al. (2008)). Unfortunately, this model version turned out to be unsuitable in connection with the very steep and complex orography of the Matterhorn region, presumably due the existence of complex orography at the boundaries of the domain. We, therefore, switched to the compressible version of EULAG (Smolarkiewicz et al., 2014; Kurowski et al., 2014, 2015; Smolarkiewicz et al.,

2016). This model version incorporates a semi-implicit integrator, which allows for a variable integration step size constrained by the CFL stability criterion independent of the propagation of sound waves.

Our general model setup closely follows the approach used in previous work (Schappert & Wirth, 2015; Wirth et al., 2020). For the representation of sub-grid scale turbulence we apply a TKE prognostic equation closure based on Schumann's parametrization (Schumann, 1991). Orography is represented through an immersed boundary approach (Mittal & Iaccarino, 2005; Smolarkiewicz et al., 2007), which is effectively like a no-slip condition (Goldstein et al., 1993; Smolarkiewicz et al., 2007). In the flat portion of the lower boundary, which only exists for the idealized mountain configurations, the surface stress is parameterized as $\boldsymbol{\tau} = \rho_0 C_d \sqrt{u_0^2 + v_0^2}\, \boldsymbol{v_0}$, where $\boldsymbol{v_0} = (u_0, v_0)$ is the horizontal velocity at the surface, $C_d = 0.01$ is the drag coefficient, and ρ_0 is the air density at the surface. There are no surface heat fluxes.

We use three distinct configurations of the model domain and its orography, ranging from highly idealized to fully realistic (Fig. 2.1). The configuration with realistic orography will be referred to as "Reference Matterhorn". The domain was extracted from a Cartesian topographic dataset of the region around the Matterhorn at a native resolution of 25 meters (swisstopo, 2017). The orography within the model domain ranges from the Zermatt valley at $z_{\min} = 1615.9$ m to the Matterhorn top with $z_{\max} = 4478$ m. At the other extreme we consider a Pyramid protruding from a flat elevated plain (called "Pyramid") like in several previous publications. As our intermediate configuration, we use the realistic orography from the Matterhorn summit protruding from a flat plain, and this configuration will be referred to as "Isolated Matterhorn". The Pyramid and Isolated Matterhorn have the same mountain height of $H = 1478$ m and range from $z_{\min} = 3000$ m to $z_{\max} = 4478$ m. The geometry of the Pyramid was chosen such that its cross-sectional profile along the center of the mountain ($y = 0$) has a slope of $\alpha \approx 48.7°$, which roughly corresponds to the average slope of the Mt. Matterhorn along this axis. For the Pyramid and Isolated Matterhorn, the model domain extends 11.6 km in the streamwise direction (coordinate x), 9.2 km in the spanwise direction (coordinate y), and 4.5 km in the vertical direction (coordinate z). Sensitivity studies regarding larger domain sizes show negligible effects on the results. The Reference Matterhorn configuration covers a slightly larger domain with extensions of 12.8 km $\times$ 9.6 km $\times$ 7 km in the x-, y-, and z-direction, respectively. This domain size represents a reasonable compromise between domain size and impact of the surrounding orography. To be sure, there is no "correct" domain size for the realistic orography due to the fact that the complex orography continues in each direction for many dozens of kilometers. However, it turned out to be important to ensure that the high ridges located west of Mt. Matterhorn are included within the domain. We slightly smoothed the orography at the northern boundary to avoid numerical instabilities. For all three configurations the grid spacing is equidistant with $\delta x = \delta y = \delta z = 25$ m. We are aware that large-eddy simulations of the atmospheric boundary layer depend on resolution. However, we assume that for our purpose the grid spacing is small enough because we only study neutral boundary layers without surface heat fluxes and the flow is highly resolved.

The inflow boundary is located at $x_{\text{in}} = -4550$ m for the Pyramid and the Isolated Matterhorn case, and at $x_{\text{in}} = -6325$ m for the Reference Matterhorn case. At the inflow boundary we prescribe profiles of wind $\mathbf{u} = (u, v, w)$ and potential temperature $\theta = T(p_0/p)^{\kappa}$, where p denotes pressure, $p_0 = 1000$ hPa is a constant reference pressure, $\kappa = R/c_p$, R is the gas constant for dry air, and c_p is the specific heat at constant pressure. The inflow wind profiles have a component $u_{\text{in}}(z)$ in the x- direction only. They are organized into two groups as in Wirth et al. (2020) (see our Fig. 2.2a): 1) profiles with a constant wind of strength $U = 5$, 10, 20 m s^{-1}; and 2) profiles with linear shear, defined through vanishing wind at lowest point of the inflow boundary and increasing to a magnitude of $U = 5$, 10, or 20 m s^{-1} at the summit of the mountain ($z = H$); the shear extends

another 500 m above the summit and transits into a constant wind at higher altitudes.

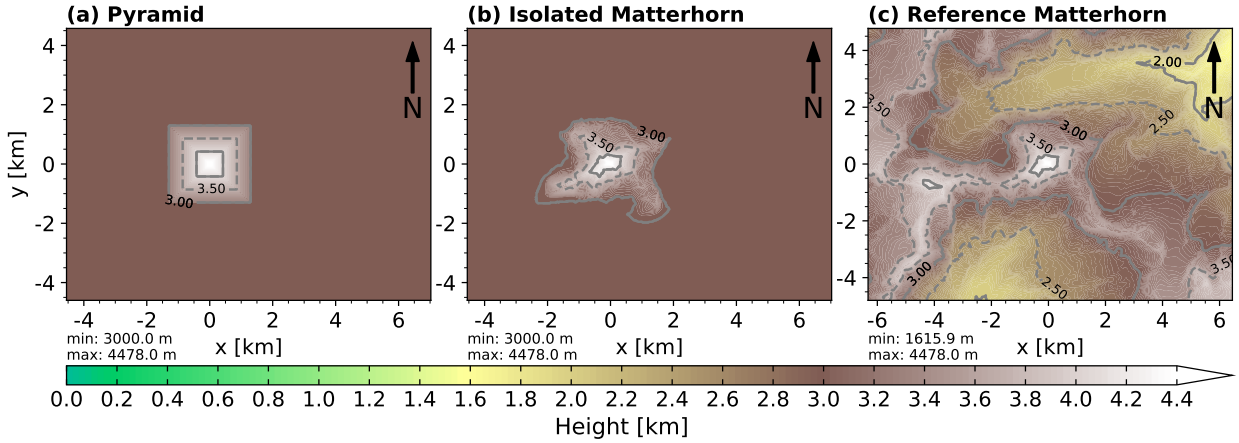

FIGURE 2.1: Model orography for (a) the "Pyramid" configuration, (b) the "Isolated Matterhorn" configuration, and (c) the "Reference Matterhorn" configuration.

We define our standard potential temperature profile at the inflow boundary to correspond to neutral stratification ($\partial\theta/\partial z = 0\,\mathrm{K\,km^{-1}}$) up to the mountain summit ($z = H$), and stable stratification ($\partial\theta/\partial z = 4\,\mathrm{K\,km^{-1}}$) above (see Fig. 2.2b). For the Reference Matterhorn configuration we consider, in addition, profiles in which the top of the neutrally stratified part is lowered by 500 and 800 m below the summit. In the following, we refer to the level at which the stratification changes from neutral to stable as the top of the boundary layer and denote it by z_{ABL}. The additional profiles were introduced because we suspect that in reality very high mountains often reach into the stably stratified free atmosphere. Unfortunately, we are not aware of any systematic observations, so in this study we consider the variation of the boundary layer height as a sensitivity experiment.

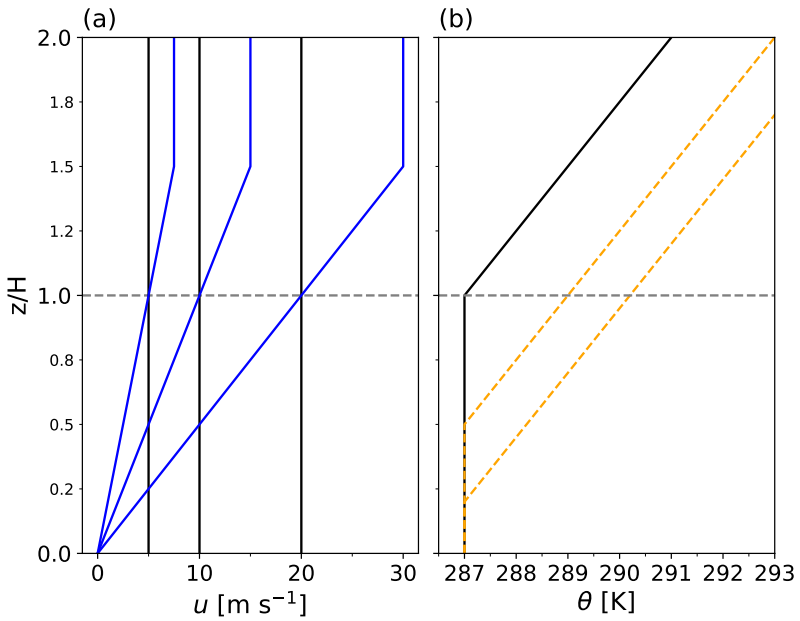

FIGURE 2.2: Inflow profiles for the numerical experiments: (a) streamwise wind component $u_{\mathrm{in}}(z)$ and (b) potential temperature $\theta_{\mathrm{in}}(z)$. The profile in (a) distinguishes two groups of profiles: one group with a constant wind (black), and another group with vertical shear (blue). In (b), the solid black line depicts the "standard" profile, while the dashed orange lines depict two additional profiles with shallower boundary layers. In both panels, the horizontal dashed line marks the top of the mountain.

In all simulations, we apply a rigid-lid condition at the upper boundary. For the Pyramid and Isolated Matterhorn we use open conditions at the streamwise boundaries and periodic conditions at the spanwise boundaries. For the Reference Matterhorn configuration all boundaries are open. In all three mountain configurations a sponge layer was added at the model top in order to minimize wave reflections. For the Reference Matterhorn case, we used additional sponge layers at the streamwise and spanwise boundaries. We tested our main results for robustness and found that they are qualitatively independent of the exact sponge design.

Each model run is split into two parts, a spin-up period of duration t_{su} and a period of analysis of duration t_{an}. The duration of the spin-up period and the total simulation time $t_{sim} = t_{su} + t_{an}$ are given in Tab. 4.2 for the different configurations. The spin-up period was made just long enough such as to reach a statistically stationary state. The initial conditions for the spin-up period are identical to the inflow conditions, with a zero wind extension below the altitude of the lowest point of the inflow boundary. For our analysis, we consider only the time-averaged fields of the period of analysis t_{an}, which increases with decreasing wind speed; using considerably shorter averaging intervals for low wind speeds would result in differences in the exact pattern of the flow geometry.

In the Pyramid setup, we eliminated small spanwise asymmetries in the y direction by computing the arithmetic mean between field values north and south of $y = 0$ (for details see Schappert & Wirth 2015).

TABLE 2.1: EULAG model details for the three different mountain configurations.

		Pyramid	**Isolated Matterhorn**	**Reference Matterhorn**
Domain		$11.6 \times 9.2 \times 4.5$ km	$11.6 \times 9.2 \times 4.5$ km	$12.8 \times 9.6 \times 7.0$ km
δx, δy, δz		25 m	25 m	25 m
Δt		CFL criterion	CFL criterion	CFL criterion
z_{min}, z_{max}		3000.0 m, 4478.0 m	3000.0 m, 4478.0 m	1615.9 m, 4478.0 m
	$u_{in}(z = H)$	Constant and shear	Constant and shear	Constant and shear
	$5\,\mathrm{m\,s^{-1}}$	120 min	120 min	120 min
t_{su}	$10\,\mathrm{m\,s^{-1}}$	60 min	60 min	60 min
	$20\,\mathrm{m\,s^{-1}}$	30 min	30 min	30 min
	$5\,\mathrm{m\,s^{-1}}$	300 min	300 min	300 min
t_{sim}[a]	$10\,\mathrm{m\,s^{-1}}$	180 min	180 min	180 min
	$20\,\mathrm{m\,s^{-1}}$	90 min	90 min	90 min

[a] The exact simulation time can deviate by less than 2 s due to the variable integration time step.

2.4 Diagnostic Tools

2.4.1 Cloud Occurrence

The formation of a banner cloud in the real atmosphere depends, amongst others, on moisture availability. Hence, a general prediction of banner cloud occurrence would require knowledge of both the flow properties and the moisture conditions. However, here we take a somewhat simplified perspective based on the results from previous investigations. Voigt & Wirth (2013) found that the key mechanism for banner cloud occurrence is uplift in the immediate lee of the mountain. Correspondingly, we use as our key diagnostic the vertical displacement Δz that a parcel has experienced along its trajectory since it has entered the model domain. For the computation of Δz we utilize a Eulerian technique, which has proven to be a useful and simple alternative to a fully Lagrangian

approach based on trajectories (Schappert & Wirth, 2015). More specifically, we introduce a tracer $\chi(\mathbf{x},t)$ which evolves according to

$$\frac{D\chi}{Dt} = M_\chi \approx 0, \tag{2.1}$$

where D/Dt denotes the material rate of change following the flow and M_χ represents material nonconservation owing to the parameterized subgrid-scale turbulence. The tracer χ is initialized as $\chi = z$, and specified at the inflow boundary with $\chi = z$. Following earlier studies (Reinert & Wirth, 2009; Voigt & Wirth, 2013; Schappert & Wirth, 2015; Prestel & Wirth, 2016; Wirth et al., 2020), the vertical displacement is then computed as

$$\Delta z = z - \chi. \tag{2.2}$$

Large positive values of Δz are associated with an increased likelihood of cloud formation owing to the uplift and related adiabatic cooling. This motivates us to estimate cloud occurrence through a positive threshold on Δz.

The field of Δz was also used to define a diagnostic that broadly estimates the potential for banner cloud occurrence. The defining characteristic of a banner cloud event is the existence of a cloud in the lee, but the absence of any cloudiness on the windward side of the mountain (see Schween et al., 2007). This means that a given flow field has a high potential for banner cloud formation whenever there is a large windward-leeward asymmetry of Δz with a plume of positive values of Δz on the leeward side. We follow the approach of Prestel & Wirth (2016) and quantify this asymmetry through a single number as follows:

$$P = \frac{\int_{\text{lee}} \langle \Delta z \rangle dxdz}{\int_{\text{lee}} dxdz} - \frac{\int_{\text{ww}} \langle \Delta z \rangle dxdz}{\int_{\text{ww}} dxdz}\,. \tag{2.3}$$

The integral is taken on the surface $y = 0$ with "lee" referring to a leeward area and "ww" referring to a windward area. The specific division into the windward and leeward sections will be outlined later (Fig. 2.5). Large positive values of P indicate a high potential for the formation of a cloud on the leeward side (given suitable moisture conditions). By contrast, negative values of P represent a situation with increased likelihood of cloud formation on the windward side, which is opposite to the banner cloud definition. $P \approx 0$ means that we can expect cloud formation on the windward or leeward side with approximately the same likelihood.

2.4.2 Vortex Geometry

Previous studies have established that the strong leeward uplift in case of banner cloud occurrence is associated with specific vortical flow structures (e.g., Fig. 4 in Voigt & Wirth, 2013). In addition, in the case of idealized orography the exact shape of these lee vortices turned out to depend sensitively on the wind profile specified at the inflow boundary (Wirth et al., 2020). This result motivates us to diagnose the three-dimensional vortex structures in the immediate vicinity of our three mountain configurations, allowing us to determine whether the occurrence of lee vortices is pyramid-specific or a general feature for any orography.

Visualizing and diagnosing vortices in turbulent flow is a thorny issue, which has been discussed extensively in the literature (e.g. Jeong & Hussain (1995)). For the configuration with an idealized pyramid we have tried several of these methods, including the standard Eulerian metrics involving vorticity or variants of the Okubo-Weiss criterion (Haller, 2005). None of these produced a coherent picture of vortices even for idealized model configurations. We, therefore, decided to apply the Lagrangian technique used in Wirth et al. (2020) which turned out to be useful for our

purposes. In this technique we consider all grid points in the volume of interest and compute both forward and backward streamlines of the time mean wind using the classical Runge-Kutta fourth-order scheme with a time step of $\Delta t = 0.25$ s for all three mountain configurations. The respective integration is extended to a length of 500 m both in the forward and the backward direction, resulting in a total length of 1000 m. We then compute the curvature K along the streamline through

$$K = \frac{\left| \frac{d\boldsymbol{r}}{dt} \times \frac{d^2\boldsymbol{r}}{dt^2} \right|}{\left| \frac{d\boldsymbol{r}}{dt} \right|^3}, \tag{2.4}$$

where $\boldsymbol{r}(t)$ represents the streamline. For a grid point to belong to a vortex we require that the mean curvature $\langle K \rangle$ must exceed a threshold K_0, where $\langle \ldots \rangle$ denotes the average along the streamline associated with the respective grid point.

2.4.3 Parcel Pathway

As detailed above, the occurrence of a banner cloud is estimated through a threshold on Δz. Depending on the flow regime, one may obtain a coherent cloud volume in the lee of the mountain (Prestel & Wirth, 2016). However, a more detailed investigation by Schappert & Wirth (2015) indicated that even in that case different parcels contained in the diagnosed cloud volume may have traveled along very different paths and, hence, have very different origins. This motivates us to compute backward trajectories starting in the "cloud volume" as diagnosed from Δz. These backward trajectories correspond to streamlines, because we limit ourselves to the time-averaged flow in this study. The streamlines are integrated backward in time using the classical Runge-Kutta fourth-order scheme with a time step of $\Delta t = 0.25$ s for the three mountain configurations. Eventually, in section 2.5.4 we identify different classes of streamlines that distinguish various pathways of parcels that end up in the banner cloud.

2.4.4 Turbulent Kinetic Energy Budget

In our analysis we also considered the turbulent kinetic energy (TKE). Using output from our LES, the resolved TKE was directly calculated from the velocity variances

$$\overline{e} = \frac{1}{2}\left(\overline{u'^2} + \overline{v'^2} + \overline{w'^2}\right), \tag{2.5}$$

where the overbars $(\overline{\ })$ denote the time average and the primes $(')$ denote the turbulent fluctuations as deviation from the time average. Generally, the full TKE budget equation can be written as follows (Stull, 1988)

$$\underbrace{\frac{1}{2}\frac{\partial \overline{e}}{\partial t} + \overline{u}_j \frac{\partial \overline{e}}{\partial x_j}}_{\text{I}} = \underbrace{+\delta_{i3}\frac{g}{\overline{\theta}}\overline{u_i'\theta'}}_{\text{II}} \underbrace{-\overline{u_i'u_j'}\frac{\partial \overline{u_i}}{\partial x_j}}_{\text{III}} \underbrace{-\frac{1}{2}\frac{\partial \overline{u_j' u_i'^2}}{\partial x_j}}_{\text{IV}} \underbrace{-\frac{1}{\overline{\rho}}\frac{\partial \overline{u_i' p'}}{\partial x_i}}_{\text{V}} \underbrace{-\overline{\varepsilon}}_{\text{VI}}, \tag{2.6}$$

where $i = 1,2,3$ and $j = 1,2,3$ represent the three Cartesian coordinates (x,y,z); $\overline{u_j}$ is the mean wind, g is the gravitational acceleration, ρ is the air density. Term I is the advection of TKE by the mean wind, II is the buoyancy production/loss term, III the shear production/loss term, IV the TKE turbulent transport term, V the redistribution of TKE by pressure perturbations, and VI the dissipation of TKE by transfer of energy from resolved scales to the subgrid scales. We separate

the turbulent fluctuations from the mean flow via Reynolds decomposition. The required Reynolds decomposition is approximated by a time average, since a spatial average is not straightforward in complex orography. Following the Reynolds averaging rules, the second-order moments are given by:

$$\overline{a'b'} = \overline{ab} - \overline{a}\,\overline{b}. \tag{2.7}$$

Higher-order turbulent moments are calculated in the same way with the help of second-order moments:

$$\overline{a'b'c'} = \overline{abc} - \overline{a}\,\overline{bc} - \overline{a}\,\overline{b'c'} - \overline{b}\,\overline{a'c'} - \overline{c}\,\overline{a'b'}. \tag{2.8}$$

In our model setup without surface heat fluxes, shear production is the main source of resolved TKE. In section 2.5.3, we use profiles of the TKE and the shear production/loss term to provide an explanation for vertical shifts of the boundary layer top on the leeward side of the Matterhorn.

2.5 Results

2.5.1 Vortex Structure and Flow Geometry

First, we investigate the changes in the flow past the mountain as we move from the idealized Pyramid towards the fully realistic Matterhorn orography. We pay particular attention to vortical structures in the immediate vicinity of the mountain and their relation to regions of strong upwelling.

Figure 2.3 visualizes the vertical wind field w and the vortical structures through our curvature measure $\langle K \rangle$ for either a constant or a sheared wind profile with an amplitude of $20\,\mathrm{m\,s^{-1}}$. First, we consider the Pyramid configuration (left column in Fig. 2.3). In agreement with Wirth et al. (2020), a sheared inflow profile (Fig. 2.3a) results in two forwardly tilted vortices. A footprint of these two counterrotating vortices also appears in the patterns of the streamlines in Fig. 2.4a. The same panel also depicts the vertical wind, indicating a volume of strong upwelling on the axis of symmetry in the lee of the mountain. That same volume can be seen in Fig. 2.3d. It transpires that air parcels being caught in the leeward recirculation region experience a direct vertical transport into the banner cloud (white volume in Fig. 2.3a). By contrast, for the constant inflow profile the leeside flow pattern and vortex geometry have a considerably different character. Combining Figs. 2.3g and 2.4d we can detect an arc-shaped vortex with a strong recirculation between its two counterrotating vortex feet. The vortex is orientated along the leeward face of the mountain which means that it is slightly tilted upstream with altitude. In addition, the region of upwelling is very close to the mountain, which is in strong contrast to the previous behavior for the sheared inflow profile. Taken together, this results in a spiraling upward transport of air parcels into the banner cloud.

Next we consider the Isolated Matterhorn configuration (middle column in Figs. 2.3 and 2.4). Overall, our simulations indicate rather substantial differences in the vortex geometry and upwelling structure between the Pyramid and the Isolated Matterhorn configuration. We start our discussion with the sheared inflow profile. There are no coherent, distinct vortex structures in the lee of the mountain (Fig. 2.3b). Instead, several individual vortex tubes exist whose axes are mostly aligned in streamwise direction. Therefore, in contrast to the pyramid, no vortex feet can be seen in the patterns of streamlines in Fig. 2.4b. Compared to the Pyramid configuration (Fig. 2.4a), the leeward recirculation is much closer to the mountain slope. At the same time, there are areas of strong upwelling on the southeast and northeast ridges of the mountain (Figs. 2.3e and 2.4b). In these regions, air parcels are lifted and transported to the leeward side before they are engulfed into the banner cloud. The simulation for the constant inflow profile reveals a more distinct geometry of

vortex structures and upwelling regions (Figs. 2.3h,k). A lobe of strong upwelling extends upwards from the southeast mountain ridge to the leeward side (Fig. 2.3k). This dominant upwind region is also visible in Fig. 2.4e. The streamline patterns shows a considerable spanwise asymmetry, with the leeward recirculation shifted to the south. Consequently, air parcels are mainly transported upwards into the banner cloud from the southeastern mountain ridge.

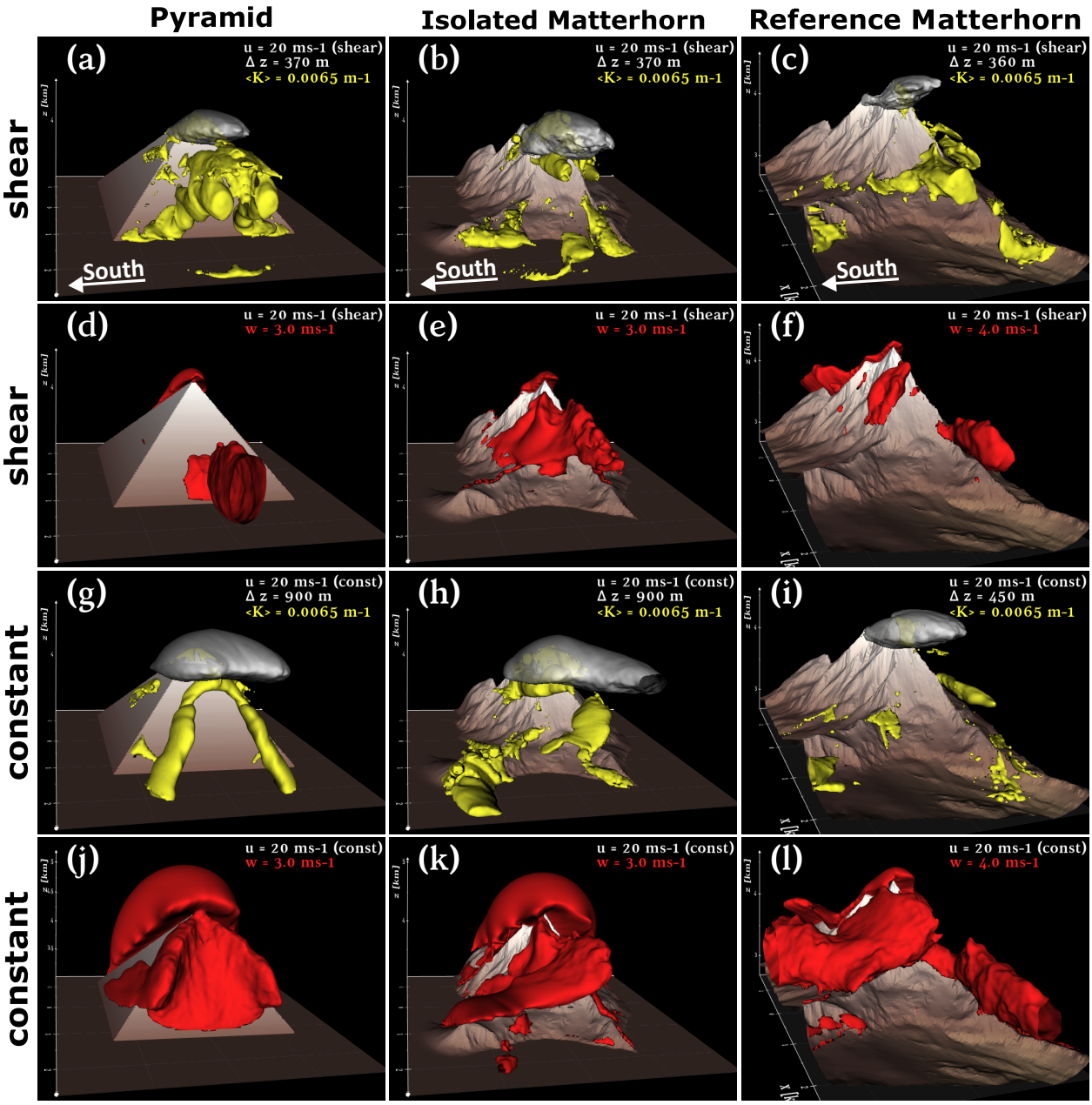

FIGURE 2.3: Three-dimensional visualizations of vortical structures (yellow) and the vertical wind field (red) in relation to the banner cloud (white). The vortical structures are displayed via the Gaussian-smoothed ($\sigma = 0.6$ grid distance) isosurface of $\langle K \rangle$ in the lee of the mountain. The banner cloud volume is defined through a threshold on Δz. The respective thresholds for isosurfaces of w, K, and Δz are given in the upper right corner of the panels. The three columns represent the three different orography configurations: (left) Pyramid, (center) Isolated Matterhorn, and (right) Reference Matterhorn. (a)-(f) Sear inflow and (g)-(l) constant inflow wind setup.

Finally, we turn to the orography of the fully realistic Reference Matterhorn configuration (right columns in Figs. 2.3 and 2.4). Overall, the leeward flow geometry is again considerably different from the previous two configurations and illustrates the important role of the ambient

orography. For both the sheared and the constant wind simulation, there is a region of strong upwelling on the northern side of the Matterhorn orography (Figs. 2.3f,l). However, air parcels lifted in this region are not carried into the banner cloud (not shown). Instead, the volume of upwelling relevant for banner cloud formation extends from the southern flank into the immediate lee of the Matterhorn. The broad independence of the location of the upwelling region to inflow wind shear is in distinct contrast to the two more idealized orographies discussed before. This feature probably results from the unique and very specific orography in the realistic mountain configuration that serve to channel the flow. For example, the ridges to the southwest and southeast of the Matterhorn extend much further in the Reference Matterhorn configuration compared to the Isolated Matterhorn configuration (Fig. 2.1c versus Fig. 2.1b). The flow pattern in the direct vicinity of the Matterhorn is quite similar for both inflow wind profiles (Figs. 2.4c,f). The only difference is that the leeward recirculation flow extends much farther downwind for the sheared inflow profile. Consequently, air parcels from the south flow into the banner cloud either via the large upwelling region or they enter the recirculation flow on the leeward side, where they are transported upward into the banner cloud. Overall, it is difficult to identify a clear vortex structure in the lee of the mountain for the Reference Matterhorn configuration. To be sure, our measure for curvature indicates a leeward vortical volume for the sheared wind profile in Fig. 2.3c, but this is not associated with substantial upwelling and does, therefore, most likely not contribute to the formation of the banner cloud.

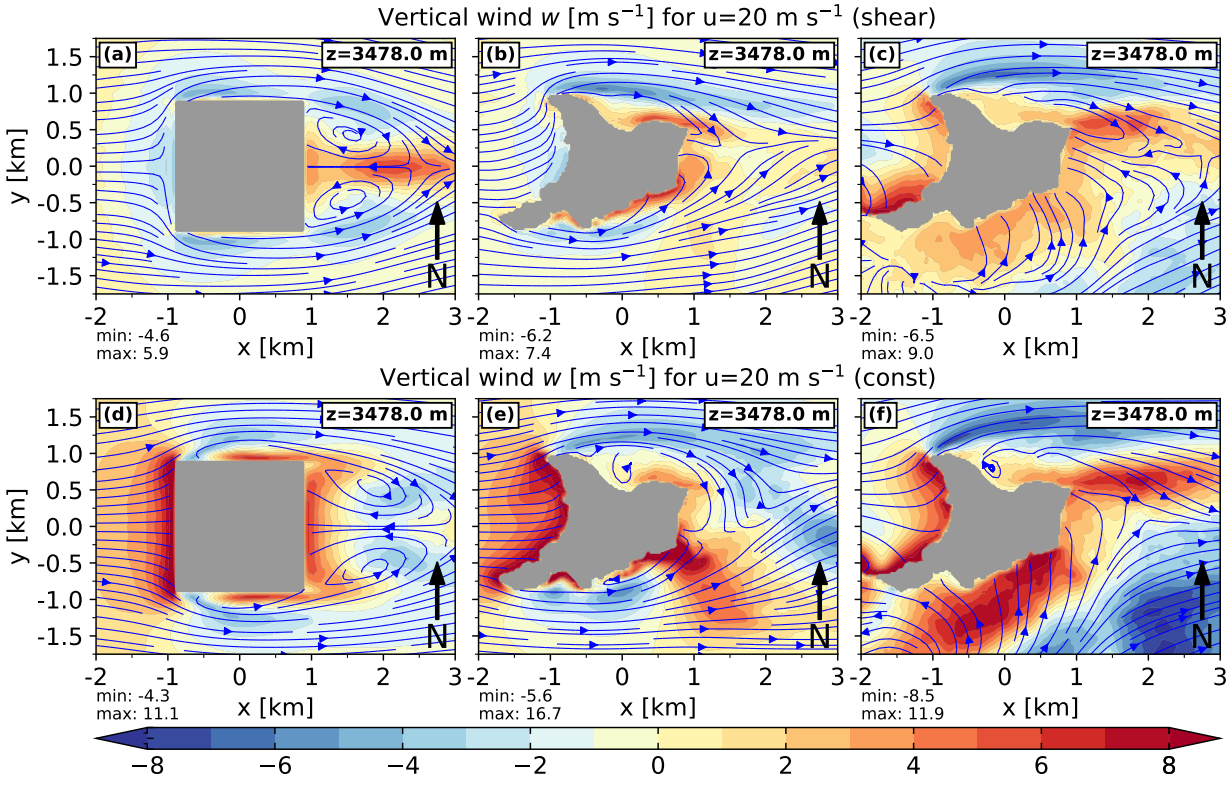

FIGURE 2.4: Vertical wind w (color; $\mathrm{m\,s^{-1}}$) and streamlines (blue lines) in a horizontal cross section for (left) the Pyramid, (center) the Isolated Matterhorn, and (right) the Reference Matterhorn configuration. The section is located at $z = H - 1000$ m for all three mountain configurations. Results are shown for the (top) sheared and (bottom) constant wind profile, both with $U = 20\,\mathrm{m\,s^{-1}}$.

2.5.2 Leeside Plume of Vertical Displacement

Next, we consider the dependence of the vertical uplift on the upstream wind profile. Figure 2.5 shows cross sections of Δz through the center of the mountain for the three orography configurations. For all simulations a plume of large Δz is visible on the leeward side. The maximum value of Δz is always larger for the constant inflow profile (bottom row) in comparison with the sheared inflow profile (top row). However, the sheared inflow profile promotes a visually more pronounced windward-leeward asymmetry compared to the constant inflow profile. For the Pyramid and the Isolated Matterhorn configurations, the potential P [see Eq. 2.3] for constant wind speeds of $5\,\mathrm{m\,s^{-1}}$ and $10\,\mathrm{m\,s^{-1}}$ is much smaller than P for $20\,\mathrm{m\,s^{-1}}$ (Fig. 2.6); it even becomes negative at $U = 10\,\mathrm{m\,s^{-1}}$. The reason for this is strong uplift close to the windward face of the mountain which leads to a shallow layer of large Δz (Figs. 2.5d,e). This results in a very small windward-leeward asymmetry of vertical displacement in terms of our metric P. At the same time, there is a well-defined plume of large Δz on the leeward side in Fig. 2.5d and Fig. 2.5e, that does have an appearance which is similar to a banner cloud. We conclude that our simple diagnostic P is not perfect for the idealized orographies. The strongest windward-leeward asymmetry is found in the Reference Matterhorn configuration (right column). Correspondingly, the potential P exhibits the largest values for the Reference Matterhorn configuration for each of the six colored tiles (Fig. 2.6c) compared to the other two configurations (Figs. 2.6a,b). We conclude that 1) the realistic Matterhorn orography is particularly conducive to banner cloud formation, that 2) the actual ambient orography is important for this property, and 3) that in this case the banner cloud formation potential is broadly independent of wind shear.

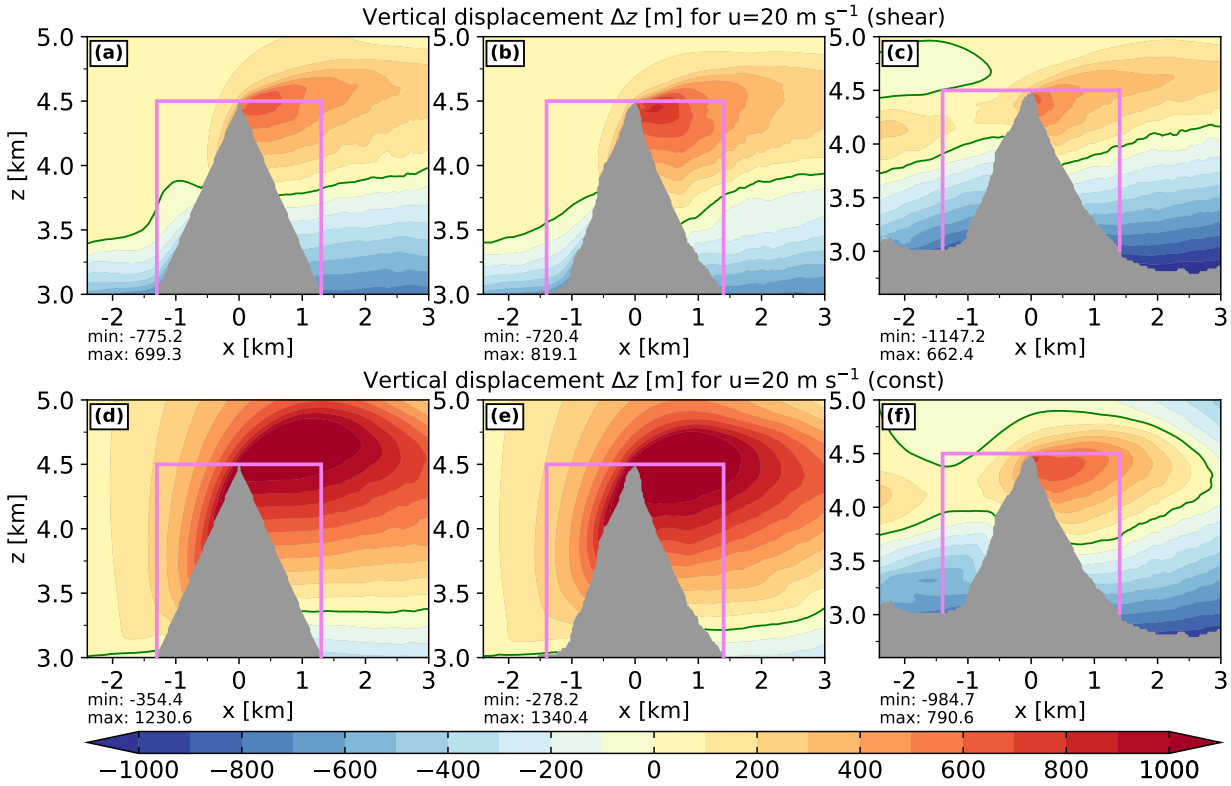

FIGURE 2.5: Vertical displacement Δz (color; m) in a vertical section through the center of the mountain (dark gray) for (left) the Pyramid, (center) the Isolated Matterhorn, and (right) the Reference Matterhorn configuration. Results are shown for the (top) sheared and (bottom) constant wind profile, both with $U = 20\,\mathrm{m\,s^{-1}}$. The green line depicts the zero contour. The purple lines delineate areas on the windward and leeward side of the mountain, which are subsequently used to compute the diagnostic P (see text for details).

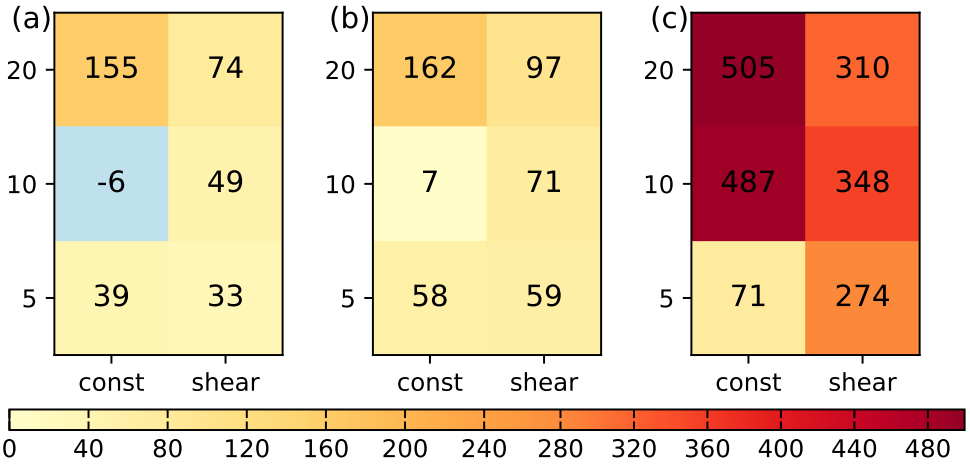

FIGURE 2.6: Banner cloud formation potential P (color; m) for (a) the Pyramid, (b) Isolated Matterhorn, and (c) Reference Matterhorn configuration with the standard potential temperature profile. The colored tiles represent the value of P for six different combinations of wind shear and wind strength; the wind strength U is given along the vertical axis (in $\mathrm{m\,s^{-1}}$). The diagnostic P is calculated via Eq. 2.3, where the windward and leeward integrals are computed in the respective regions delineated by the purple lines in Fig. 2.5.

2.5.3 Sensitivity to the Top of the Boundary Layer

So far, we have only examined simulations with neutral stratification up to the mountain top. This was motivated by the results of Prestel & Wirth (2016), which suggested that banner cloud formation with idealized orography is generally associated with weak stratification. However, this may exclude important realistic situations, in which the summit of the mountain extends above the boundary layer top and protrudes into the stably stratified free atmosphere. Therefore, we extended the set of potential temperature inflow profiles and lowered the boundary layer top to an altitude below the mountain summit as shown in Fig. 2.2b. This allows us to investigate to what extent the ambient stratification has an impact on banner cloud occurrence at Mt. Matterhorn.

First, we compare the potential P [see Eq. 2.3] for banner cloud occurrence for the different inflow profiles in the top row of Fig. 2.7. While for the standard potential temperature profile (Fig. 2.7a) almost all considered combinations of wind shear and wind strength are associated with large positive values of P, this is not the case any longer for the shallower boundary layers in Figs. 2.7b and 2.7c; rather, we obtain considerably smaller and even negative values of P in case of a constant wind profile with wind speeds lower than $U = 20\,\mathrm{m\,s^{-1}}$.

This result prompts a more detailed discussion about our diagnostic P for banner clouds occurrence. For this purpose, we consider Fig. 2.7d and 2.7e, which show cross sections of the vertical displacement Δz for the configuration with $U = 5\,\mathrm{m\,s^{-1}}$ and a boundary layer top located 500 m below the mountain summit, both for the sheared (Fig. 2.7d) and the constant wind profile (Fig. 2.7e). For both configurations, the value of P is about equal with a fairly low value (Fig. 2.7b). By definition, this corresponds to a weak potential for banner cloud formation for both simulations. However, it is immediately noticeable that for the constant wind profile (Fig. 2.7e), the key mechanism for banner cloud formation, namely positive vertical displacement on the leeward side, is completely absent. This is in sharp contrast to the results for a sheared wind profile shown in Fig. 2.7d. Here, we see high positive values of Δz just below the summit with a weak windward-leeward asymmetry favoring banner cloud occurrence. The comparison shows that despite the positive values of P for a constant wind profile, no cloud formation can be expected. Similarly, our metric P provides a misleading prediction for the configuration with a boundary layer top 800 m

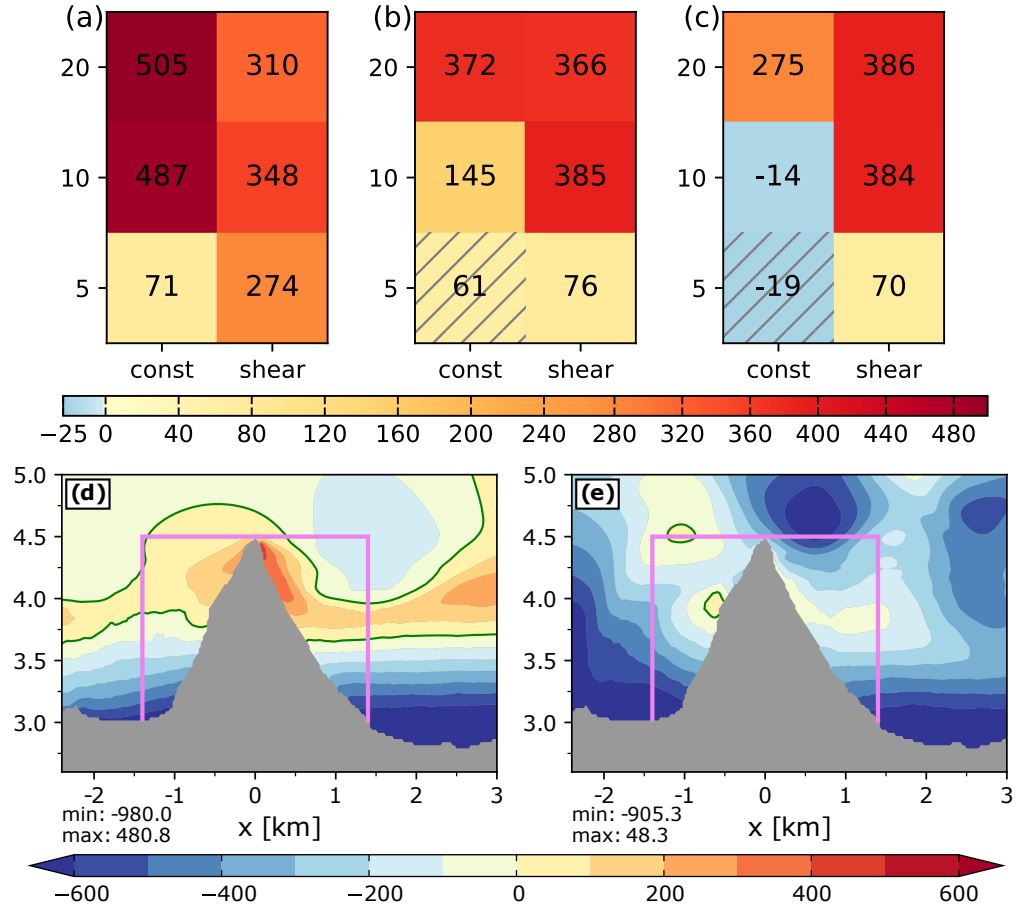

FIGURE 2.7: (top) Banner cloud formation potential P (color; m) for the Reference Matterhorn configuration with (a) $z_{ABL} = H$, (b) $z_{ABL} = H - 500$ m, and (c) $z_{ABL} = H - 800$ m. The numbers in the colored tiles represent the value of P for six different combinations of wind shear and wind strength; the wind strength U is given along the vertical axis (in $\mathrm{m\,s^{-1}}$). The diagnostic P is calculated via Eq. 2.3, where the windward and leeward integrals are computed in the respective regions delineated by the purple lines in Fig. 2.5. (bottom) The vertical displacement Δz (color; m) in a vertical section through the center of the mountain (dark gray) for the (d) sheared and (e) constant inflow profile with $U = 5\,\mathrm{m\,s^{-1}}$ of the configuration with $z_{ABL} = H - 500$ m.

below the summit for the constant wind profile with $U = 5\,\mathrm{m\,s^{-1}}$ (Fig. 2.7c), because no positive vertical displacement is found at the summit (not shown). In both cases the interpretation of our metric P is problematic, and this is indicated by hatching the colored tiles in Fig. 2.7.

For all other simulations, the results indicate that there is a considerable dependence of P on wind speed in situations in which the boundary layer top of the ambient atmosphere is located below the mountain summit. The question is: why?

We hypothesize that the underlying reason for this sensitivity to wind speed lies in the fact that the complex orography of the Matterhorn and its immediate environment has a non-negligible impact on the stratification profile, and that the strength of the impact depends on the wind speed of the incoming flow. To test this hypothesis, we show vertical profiles of potential temperature slightly upstream and downstream of the Matterhorn summit in Fig. 2.8. First, we can see that in the case of the standard potential temperature profile (darkest color hue in each panel of Fig. 2.8), the boundary layer extends to higher altitudes on the leeward side than on the windward side independent of the inflow wind profile.

By contrast, for the shallower boundary layer inflow profiles, the difference between windward and leeward side shows a more complex behavior. In the particular case of $U = 20\,\mathrm{m\,s^{-1}}$ with wind shear (right column of Fig. 2.8), the boundary layer in the lee is much deeper than on the

windward side and extends to just above the mountain summit. In this case our hypothesis verifies in the sense that the orography has substantially modified the stratification while the air has passed the mountain. Looking at the vertical profile of the resolved TKE and the corresponding shear production/loss in Figs. 2.9c and 2.9f, we can interpret the modified stratification as the result of shear production of TKE near the Matterhorn summit, which leads to mixing at the top of the boundary layer and consequently to erosion of the lowest part of the free atmosphere; the net effect is an upward shift of the boundary layer top all the way to the summit level.

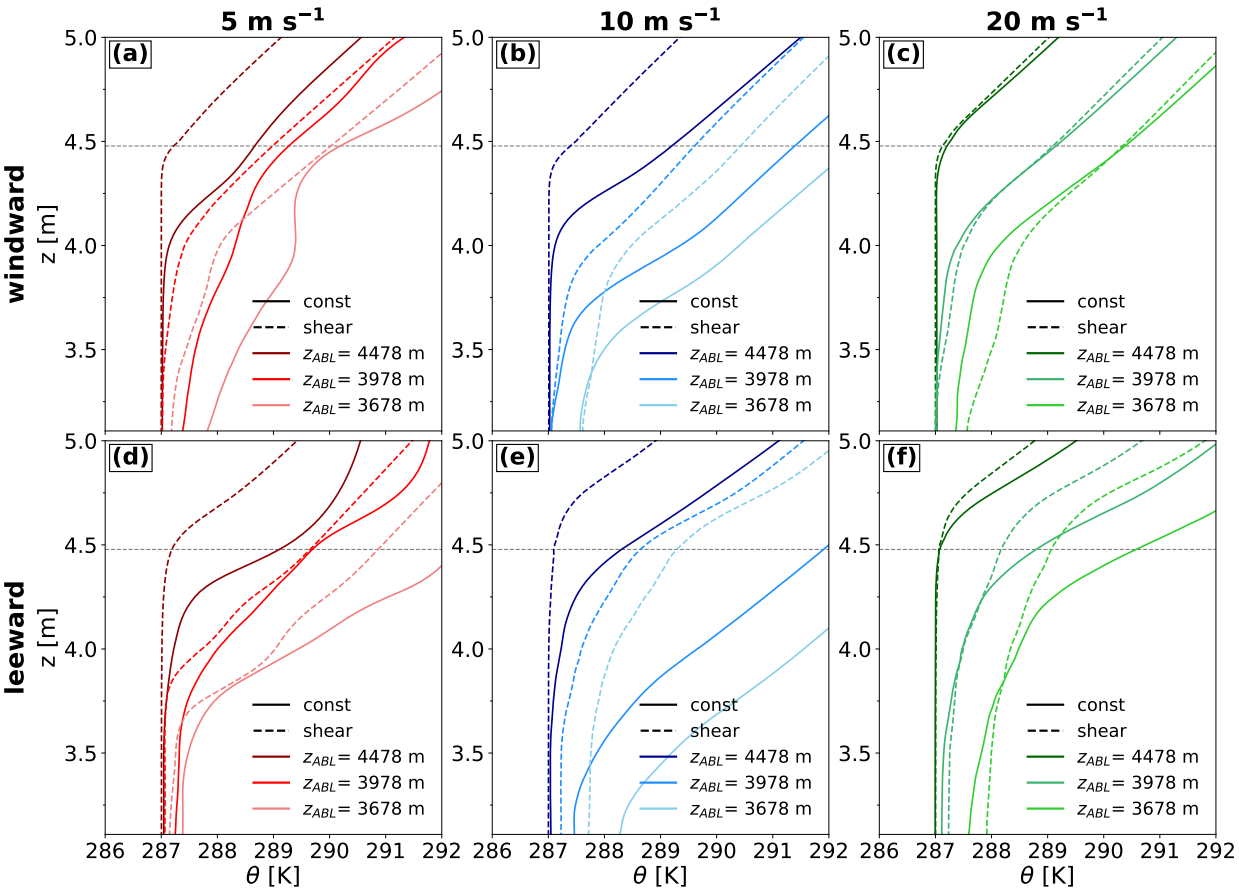

FIGURE 2.8: Profiles of potential temperature (top) on the windward side ($x = -1500$ m) and (bottom) on the leeward side ($x = +1500$ m) averaged along $y = \pm 250$ m for the Reference Matterhorn configuration. In each panel the three color hues represent the three different boundary layer tops as shown in Fig. 2.2b. The results for the constant and sheared inflow profiles are drawn as solid and dashed, respectively. The horizontal dashed line marks the mountain top. The different columns represent different wind speeds: (left) $U = 5\,\mathrm{m\,s^{-1}}$, (center) $U = 10\,\mathrm{m\,s^{-1}}$, and (right) $U = 20\,\mathrm{m\,s^{-1}}$.

The question is whether this effective erosion depends on the strength of the turbulence and, hence, on the wind speed of the ambient flow. To answer this question, we turn to the left column in Fig. 2.8 corresponding to $U = 5\,\mathrm{m\,s^{-1}}$. In this simulation there is much less of a clear upward shift of the boundary layer top as a result of the flow past the mountain. Rather, we see a slightly lower boundary layer top, but at the same time the boundary layer itself turns more neutral. Fig. 2.9a and 2.9d shows that the weaker wind is associated with considerably less turbulence and, hence, less erosion of the free atmosphere. This would explain the rather small or even negative values of P in Fig. 2.7 for $U = 5\,\mathrm{m\,s^{-1}}$, given that banner cloud formation prefers weak stratification all the way up to the summit level (Prestel & Wirth, 2016).

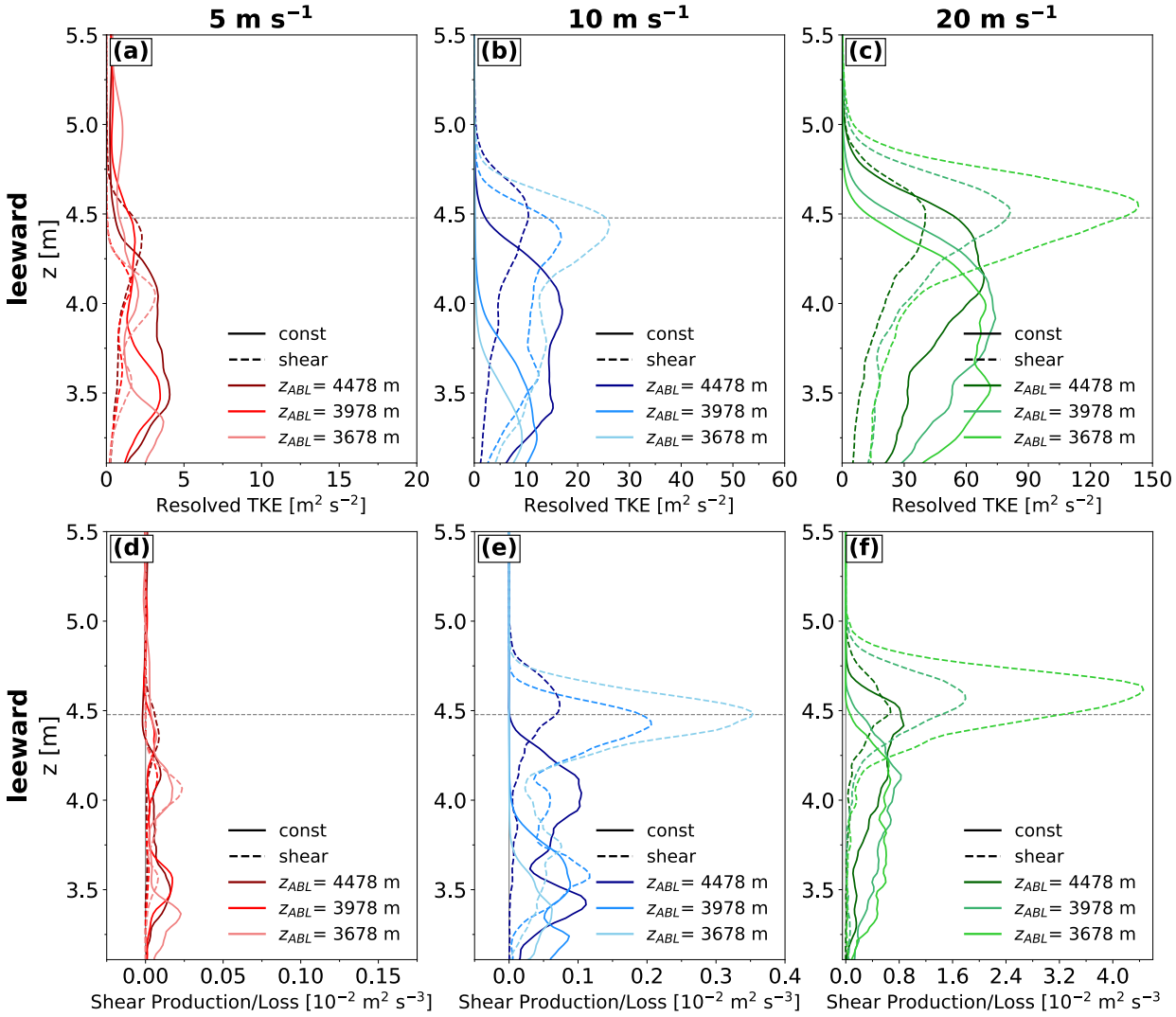

FIGURE 2.9: Profiles of the (top) resolved TKE and (bottom) TKE shear production/loss on the leeward side ($x = +1500$ m) and averaged along $y = \pm 250$ m for the Reference Matterhorn configuration. The three color hues represent the three different inflow boundary layer tops. The results of the constant and sheared inflow profiles are are shown as solid and dashed curves, respectively. The horizontal dashed line marks the mountain top. The different columns represent different wind speeds: (left) $U = 5\,\mathrm{m\,s^{-1}}$, (center) $U = 10\,\mathrm{m\,s^{-1}}$, and (right) $U = 20\,\mathrm{m\,s^{-1}}$.

It is also interesting to consider $U = 10\,\mathrm{m\,s^{-1}}$, which is intermediate between the previous two cases. In both Figs. 2.7b and 2.7c, there is a strong contrast between the constant and the sheared wind profiles, with much lower or even negative values for the constant wind profile and high positive values for the sheared wind profile. It follows that in this case the wind shear plays an important role for banner cloud occurrence. This is consistent with the profiles of potential temperature in Fig. 2.8 (middle column) and strong shear production of resolved TKE in Fig. 2.9e. They show a considerable upward shift of the boundary layer top (Figs. 2.8b,c) with strong turbulence production at the summit level (Fig. 2.9e) for the sheared inflow wind profiles only. For the configuration with the boundary layer top located 500 m below the mountain summit and the constant wind profile of $U = 10\,\mathrm{m\,s^{-1}}$, the boundary layer top remains well below the summit on the leeward side (Fig. 2.8e). In this case the boundary layer top does not experience a vertical shift because (weak) shear production of TKE is confined to the lower part of the boundary layer (Fig. 2.9e). Accordingly, the relatively low positive potential of the banner cloud occurrence (Fig. 2.7b) corresponds to a banner cloud that is located very close to the mountain summit and cannot extend far downstream because the boundary layer is too shallow.

There is another way to test our hypothesis regarding the importance of vertical mixing for banner cloud formation in the case of shallow boundary layer height. Whenever there is strong mixing below the mountain summit, the leeward wind profile should be approximately constant with altitude; as a result, one would expect rather strong wind shear close to the summit level, because the wind profile has to continuously join the ambient wind above the mountain. We, therefore, consider profiles of the streamwise wind component in the lee of the mountain (Fig. 2.10). The figure suggests that we can distinguish two classes of profiles, one with strong shear and one with near constant wind close to the summit level. As it turns out, those profiles that have strong shear at summit level correspond to a large positive value of P. As argued above, this is consistent with our hypothesis.

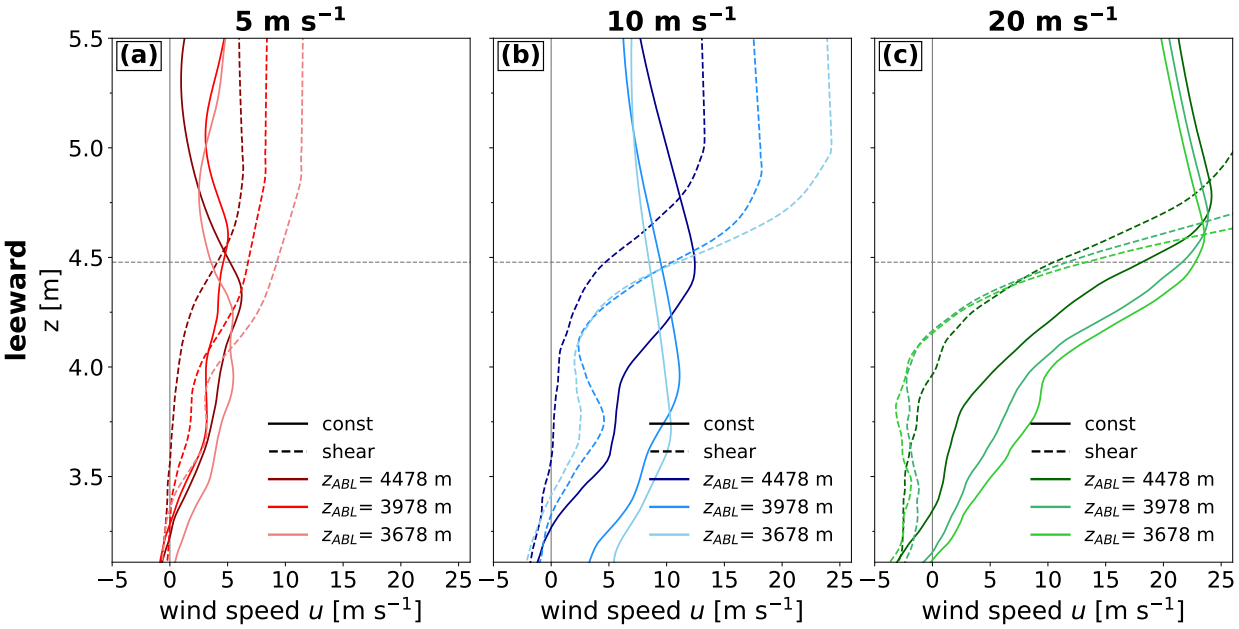

FIGURE 2.10: Streamwise wind profiles on the leeward side of the mountain at $x = 1500$ m averaged along $y = \pm 250$ m for the Reference Matterhorn configuration. The three color hues represent the three different inflow boundary layer tops. The results of the constant and sheared inflow profiles are shown as solid and dashed curves, respectively. The horizontal dashed line marks the mountain top. The different columns represent different wind speeds: (a) $U = 5\,\mathrm{m\,s^{-1}}$, (b) $U = 10\,\mathrm{m\,s^{-1}}$, and (c) $U = 20\,\mathrm{m\,s^{-1}}$.

2.5.4 Pathways into the Banner Cloud

In section 2.5.1 we found that the step from the highly idealized Pyramid to the Isolated Matterhorn configuration was associated with considerable differences in the flow geometry in the direct vicinity of the mountain. Furthermore, the fully realistic Reference Matterhorn configuration featured a unique region of upwelling on the southern face of the Matterhorn, which extends to the leeward side. One can assume that these differences have a pronounced impact on the Lagrangian behavior of air parcels flowing into the banner cloud. This subsection is meant to shed some light into the issue.

Pathways of air parcels leading into the banner cloud were previously investigated by Schappert & Wirth (2015) using an idealized pyramid. They identified two distinct classes. The first class was associated with parcels flowing directly past the mountain summit and into the banner cloud; the second class was associated with parcels that take a much longer path around the mountain, recirculate towards the leeward face, and finally get lifted into the cloud. We perform a

similar analysis using our three configurations for the model orography with the standard potential temperature inflow profile.

The banner cloud is diagnosed using a subjectively chosen, case-specific threshold of Δz, namely 900 m (370 m) for the Pyramid and the Isolated Matterhorn, and 450 m (360 m) for the Reference Matterhorn configuration for a constant (sheared) inflow profile. These threshold values, which are independent of wind speed, were motivated by the desire to obtain a situation where the cloud is broadly confined the leeward side with only very little cloudiness on the windward side — since this corresponds best with the definition of a banner cloud (Schween et al., 2007). To distinguish the different pathways, we computed backward trajectories as described in section 2.4.3; thereafter we classified them according to the orientation of the parcels' path relative to the mountain summit during the uplift phase on their way into the cloud. The backward integration was limited to 200 minutes, and we eliminated those trajectories which terminated within the orography or were caught in regions of near-zero wind speed. The fraction of "survived" trajectories for each model configuration is given in Table 2.2. On average, 83.9 % of the trajectories for the Pyramid, 77.3 % for the Isolated Matterhorn, and 81 % for the Reference Matterhorn configuration were retained by our algorithm.

TABLE 2.2: Overview of the number of backward trajectories used in the analysis for various model configurations with the standard potential temperature inflow profile. No backward trajectories were calculated for the Matterhorn reference orography with a constant inflow wind profile of $U = 5\,\mathrm{m\,s^{-1}}$, because in this case the maximum vertical displacement Δz was well below the selected threshold of 450 m.

	$u_{\mathrm{in}}(z = H)$	**Pyramid**	**Isolated Matterhorn**	**Reference Matterhorn**
Constant	$5\,\mathrm{m\,s^{-1}}$	7793 (79.6 %)	14766 (69.9 %)	– (-)
	$10\,\mathrm{m\,s^{-1}}$	12783 (81.9 %)	18132 (71.7 %)	3036 (82.5 %)
	$20\,\mathrm{m\,s^{-1}}$	70162 (86.2 %)	70403 (84.9 %)	16625 (83.3 %)
		$\mu = 82.6$ %	$\mu = 75.5$ %	$\mu = 82.9$ %
Shear	$5\,\mathrm{m\,s^{-1}}$	7190 (88.6 %)	13735 (75.9 %)	2966 (76.1 %)
	$10\,\mathrm{m\,s^{-1}}$	11391 (82.3 %)	19117 (78.1 %)	5727 (78.5 %)
	$20\,\mathrm{m\,s^{-1}}$	21886 (84.8 %)	32562 (82.9 %)	6504 (82.3 %)
		$\mu = 85.2$ %	$\mu = 79.0$ %	$\mu = 79.0$ %

An example for the Reference Matterhorn configuration is shown in Fig. 2.11. Apparently, there are different classes of pathways referred to as "Windward", "Lee", and "South". A corresponding pathway "North" does not exist in this case.

We now present a systematic comparison of the relative importance of the pathways between the different mountain configurations in Fig. 2.12, where "relative importance" is measured by the fraction of backward trajectories that belong to a certain class. First, we have a look at the idealized Pyramid configuration (left column). In accordance with Schappert & Wirth (2015) only the classes "Windward" and "Lee" make substantial contributions, while the classes "South" and "North" are much less important by comparison. For a constant inflow wind profile (Fig. 2.12a), the "Windward" class contributes the largest fraction for $U = 20\,\mathrm{m\,s^{-1}}$, while the "Lee" class is the largest fraction for $U = 5\,\mathrm{m\,s^{-1}}$ and $10\,\mathrm{m\,s^{-1}}$. There is a very clear dominance of the "Lee" class in case of the sheared inflow wind profile independent of the wind speed (Fig. 2.12d).

Turning next to the isolated Matterhorn configuration, we see a significant increase in the classes "South" and "North" for a constant wind profile (Fig. 2.12b). Although the "Windward" class remains the most important for a wind speed of $U = 20\,\mathrm{m\,s^{-1}}$, the classes "South" and "North" together contribute the highest proportion for lower wind speeds, mostly at the expense of class "Lee". In contrast, class "North" is not relevant for the sheared wind field, and class

"South" alone represents the most important class (Fig. 2.12e). In comparison with the Pyramid configuration, the fraction of class "Lee" is significantly reduced.

Finally, the pathway analysis for Reference Matterhorn (right column in Fig. 2.12) results in a quite different behavior which contrasts the behavior in the previous two (more idealized) mountain configurations. The most striking difference is the fact that now the "South" class dominates independent of the wind speed and shear. Furthermore, the "Lee" class is even less important compared to the Isolated Matterhorn configuration. This result can directly be related to the unique feature of the large region of upwelling on the southern face of the Matterhorn in Fig. 2.3f and 2.3l. The underlying reason for this behavior must be attributed to the unique topographic conditions of the orography. In particular the ridges connected to the Matterhorn to the southwest and southeast serve to effectively channel the parcels along their trajectories. Presumably, this is also the reason why air currents are strongly separated from each other, as can be seen in Fig. 2.11. The "North" class that we found mainly for the Isolated Matterhorn configuration does not play a role here at all (see Figs. 2.12c,f).

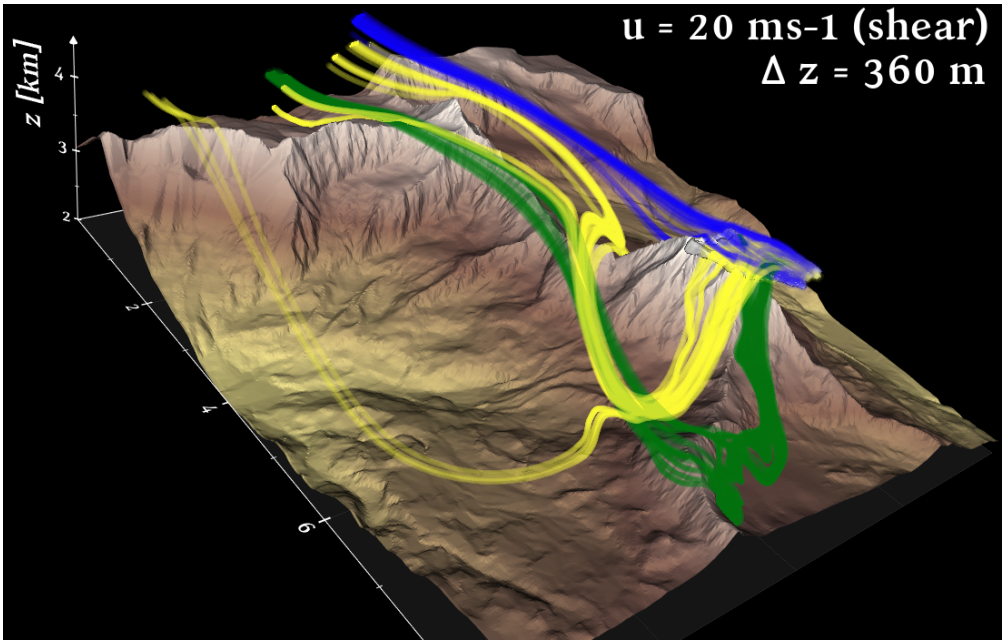

FIGURE 2.11: Pathways of parcels on their way into the banner cloud for the Reference Matterhorn orography with a sheared inflow wind profile with $U = 20\,\mathrm{m\,s^{-1}}$. The color distinguishes different classes of pathways: "Windward" (blue), "Lee" (green), and "South" (yellow). For reasons of clarity the figure shows only a limited selection of trajectories for each pathway.

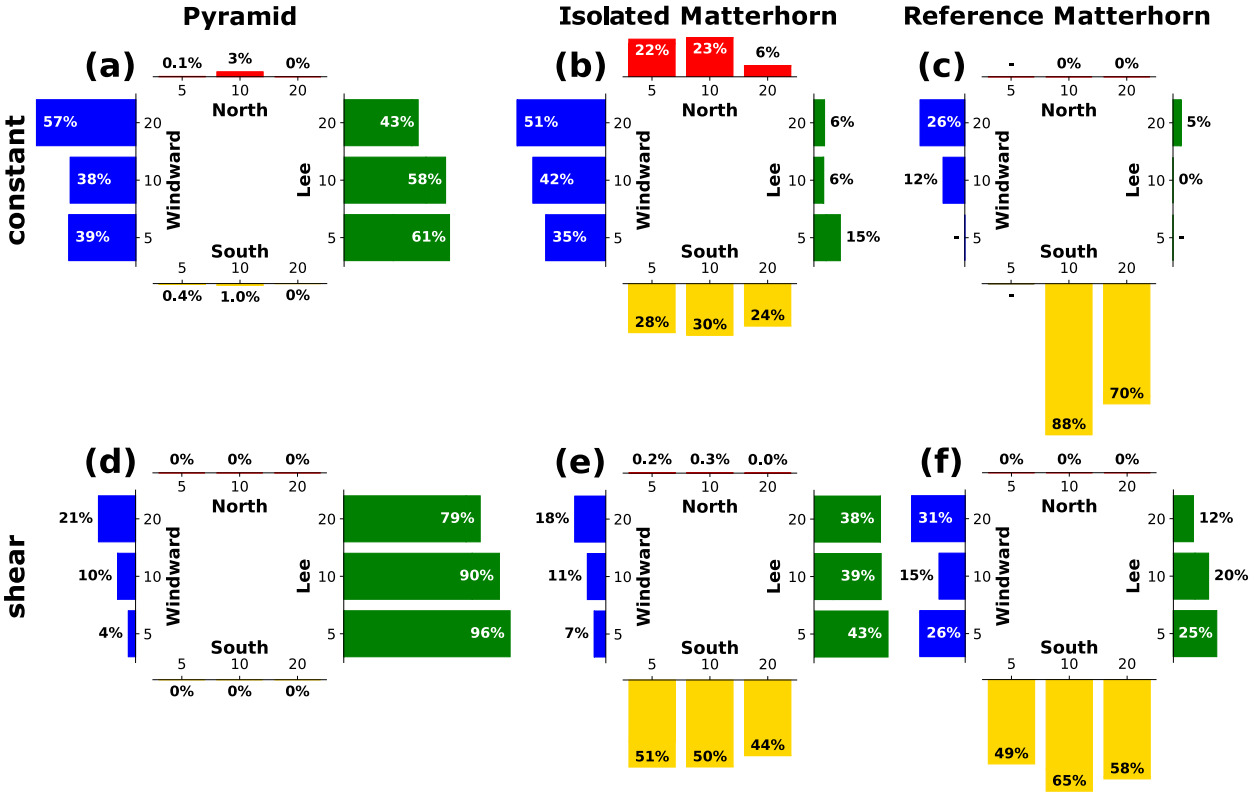

FIGURE 2.12: Relative importance of the different pathways of air parcels entering the banner cloud for the (left) Pyramid, (center) Isolated Matterhorn, and (right) Reference Matterhorn configuration. (top) Constant wind profiles; (bottom) sheared wind profiles. The colored bars quantify the fraction of trajectories entering the banner cloud from the different directions. The numbers at the base of the color bars indicate the value of U (in $\mathrm{m\,s^{-1}}$). No backward trajectories were calculated for the Reference Matterhorn configuration with a constant inflow wind profile of $U = 5\,\mathrm{m\,s^{-1}}$, because the maximum vertical displacement Δz was well below the selected threshold of 450 m.

2.6 Summary and Conclusions

In this study we carried through numerical simulations in order to investigate the formation of banner cloud formation, i.e., clouds in the lee of a steep mountain. To this end we followed previous studies and used the vertical displacement as a proxy for the propensity of cloud formation. A flow field is associated with an increased likelihood of leeward cloud occurrence whenever there is a large windward-leeward asymmetry of vertical displacement with a plume of large values on the leeward side. We quantified this asymmetry by a single number P. In contrast with earlier studies that were exclusively based on idealized orography, we considered three model configurations that differed in the complexity of the underlying orography: 1) a quadratic Pyramid, 2) realistic orography from the top-most 1478 m of Mt. Matterhorn protruding from a flat plain, and 3) fully realistic orography of the Matterhorn and its environment. In addition, we considered a range of inflow conditions that differed in the depth of the boundary layer. For all cases, we analyzed the structure and the properties of the time-averaged flow. Our main goal was to find out to what extent the results of earlier studies with idealized model configurations carry over to more realistic conditions.

As expected, more realistic orography is associated with more complex flow patterns. In particular, the spanwise symmetry from the idealized Pyramid configuration is broken on the leeward side. At the same time, the vortical structures appear to be much less coherent to an extent that those trajectories that reach the banner cloud were sometimes unrelated to these vortical features. Nevertheless, in all cases with banner cloud formation there are well-defined regions of uplift,

although these are not necessarily confined any longer to the leeward side of the mountain.

For situations in which the ambient atmosphere is neutral up to the mountain summit, we found that the impact of the inflow wind profile is less pronounced for realistic orography in comparison with idealized orography. There is banner cloud formation for any wind speed, consistent with Wirth et al. (2020). We interpret this as a result of the upstream orography, which modifies the wind profiles such that the mountain "does not see" the inflow profile any longer. This is in stark contrast to earlier studies with flat terrain in the upstream region, in which we found rather strong sensitivity to the inflow wind profile.

At the same time, we obtained important new results for ambient atmospheric profiles that have a shallow boundary layer with the top of the mountain protruding into the stably stratified free atmosphere. For these cases we found a strong dependence of banner cloud formation on the wind speed, which is in stark contrast with the results of Wirth et al. (2020) for a deep boundary layer. By analyzing profiles of potential temperature, TKE, and the shear production of TKE, we found that the underlying reason for this behavior is the fact that stronger turbulence in case of stronger wind tends to create a more neutral stratification. The latter is conducive to banner cloud formation according to Prestel & Wirth (2016). Interestingly, the wind speed needed to get a more neutral boundary layer turned out to be considerably lower in the case of a sheared ambient wind profile. The latter result is consistent with the fact that it is easier to create turbulence in shear flow than in a constant flow.

Finally, we investigated the different pathways along which parcels reach the banner cloud. Not surprisingly, more realistic orography breaks the spanwise symmetry and adds novel pathways that were not existent in case of idealized orography used in earlier studies. In particular, there are new pathways on the spanwise faces of the mountain. In case of the fully realistic Matterhorn orography, the fraction of the southern pathway dominates by a large margin. We argued that this is due to the existence of pronounced ridges connecting the Matterhorn summit to the surrounding terrain.

Overall, we conclude that even extremely complex orography allows the formation of banner clouds. Similar as for more idealized orography, the main mechanism involves the existence of a region with strong uplift, although the latter is not necessarily confined to the leeward side of the mountain any longer. In addition, weak stratification all the way up to the mountain summit is very important for banner cloud formation; the weak stratification must be either a property of the ambient atmosphere, or it can be self-created through turbulence arising from the interaction between the atmosphere and the orography in case of strong wind speeds.

2.7 Acknowledgments

We are grateful to Zbigniew Piotrowski for his support during our transition from the anelastic to the compressible EULAG version and expert advice on numerous technical aspects. We also thank our colleagues Elmar Schömer und Ronja Schnur from the Institute of Computer Science for providing the python package pygranite for GPU based trajectory calculation (Schnur, 2022). All figures and animations were generated with the Python matplotlib package (Hunter, 2007) and vedo package (Musy et al., 2020). This research was funded by the German Research Foundation through Grant WI-1685/13-1.

2.8 Data Availability Statement

The simulation data necessary for reproducing figures in this study are available at https://zenodo.org/record/8171107

3 The MatterHEX Experiment – Investigating Atmospheric Flow Patterns in Highly Complex Terrain Related to Banner Cloud Formation

This chapter is taken from a manuscript which is currently under review:

Hoch, S. W., Thomas, M. L., Huwald, H., Lehning, M., van Schaik, B. J. A., Rentel, D. S., Imbert, P., and V. Wirth: The MatterHEX Experiment – Investigating Atmospheric Flow Patterns in Highly Complex Terrain Related to Banner Cloud Formation. J. Atmos. Sci. [Under Review]

3.1 Abstract

Orographic clouds typically form on the windward side of a topographic barrier when approaching air is cooled as it is lifted, and moisture condenses into cloud droplets. Under special conditions, however, clouds can appear on the leeward side of a mountain. Attached to leeside mountain slopes below the summit like a banner to a mast, these cloud formations are known as "banner clouds". They are often seen on steep singular mountains such as the Matterhorn (Cervino) of the European Alps. Their formation indicates that vertical displacement in the lee dominates over the lifting occurring upwind. Past investigations of the flow conditions associated with banner clouds have mostly relied on numerical simulations, as observations are difficult in the often extremely complex or inaccessible mountainous terrain. This article summarizes the main findings of the MatterHorn EXperiment, MatterHEX, that was conducted at the Matterhorn near Zermatt, Switzerland, in fall 2023. The experiment was designed to overcome observational challenges due to topography and to collect the minimum data necessary to assess the flow conditions conducive to banner cloud formation. Upwind flow and stability conditions were observed with radiosondes; cloud conditions were monitored with webcams; and leeward flow patterns were remotely sensed with Doppler lidar from the best possible location still accessible by foot. Time-averaged lidar scans reveal strong leeside ascent associated with banner cloud formation, while individual scans resolve the turbulent features associated with leeside flow separation. Our analysis shows that flow conditions around the Matterhorn are frequently conducive to banner cloud occurrence, but that a lack of moisture can prevent their formation.

3.2 Significance Statement

Understanding weather in mountainous terrain is of high relevance owing to its sometimes-extreme character. Yet, observations are often very challenging due to the complexity of the terrain. The field campaign described in this paper addresses this challenge with the combination of careful campaign design and state-of-the-art instrumentation. Our focus lies on the leeside flow structures of an isolated steep mountain, the Matterhorn of the European Alps. Analysis of the data indicates leeside flow reversal and upwelling, consistent with theory. Our observations allow us to be the first to test existing theories on the formation of leeside banner clouds. The data is well-suited for the evaluation of corresponding Large-Eddy Simulations that resolve similar spatiotemporal scales in highly complex terrain.

3.3 Capsule

Meteorological observations in the highly complex terrain around the Matterhorn test existing theories of banner cloud formation.

3.4 Introduction

Flow past orography is a classic topic in mountain meteorology (Whiteman, 2000). In recent decades, associated processes such as gravity waves (Smith, 1979; Durran, 2003), orographic drag (Fritts et al., 2016), and orographic precipitation (Roe, 2005) have been specific foci of research and field campaigns. Most of these studies have dealt with the meso- or larger-scale flow over large mountains or mountain ranges rather than a single mountain. One reason may be the challenges in obtaining field observations in highly complex and steep terrain, but there are also challenges in performing highly resolved numerical simulations of flow past steep orography (e.g. Lundquist et al., 2012; Connolly et al., 2021). At scales smaller than a mountain, flow separation and the associated influence on particle dynamics and snow deposition have been investigated over idealized and real complex terrain (Lehning et al., 2008; Comola et al., 2019; Reynolds et al., 2024a; Gerber et al., 2017; Lehner et al., 2019; Reynolds et al., 2024b; Berg et al., 2024). These studies focus on near surface boundary layer flow features such as speed-up and flow separation.

One phenomenon on the scale of a typical mountain has received some attention recently: orographic banner clouds. These clouds form, somewhat counter-intuitively, in the lee of steep mountains, often under otherwise cloud-fee conditions (Glickman, 2000). They are closely attached to the lee slopes, and the combination of strong flow past the mountain's summit and the associated wind shear let them appear like a banner flying in the wind (Fig. 3.1). Schween et al. (2007) used time-lapse movies for a first systematic study of these clouds forming on Mount Zugspitze, Germany, which were then combined with complementary meteorological observations to reveal some of their properties (Wirth et al., 2012). The first Large-Eddy Simulations (LES) of banner clouds were conducted by Reinert & Wirth (2009) and Voigt & Wirth (2013). Their simulations were based on idealized topography; they resolved a bow-shaped vortex in the lee of the obstacle and highlighted the role of the extensive leeside vertical uplift for banner cloud formation. Subsequently, trajectory calculations by Schappert & Wirth (2015) illustrated that most air parcels that reach the banner cloud have previously traveled around the mountain before ascending on the lee side. Prestel & Wirth (2016) systematically examined the conditions that are conducive to banner cloud formation, stressing the importance of a weakly stratified ambient atmosphere as well as the steepness of the mountain. More recently, Thomas & Wirth (2023) [chapter 2] investigated the

transition from idealized to realistic orography of the Matterhorn region in LES and discussed the implications.

FIGURE 3.1: Banner cloud on the Matterhorn (Cervino), 1540 UTC 29 September 2023.

Substantial theoretical guidance exists on terrain-flow interactions. Generally, the flow response to a topographic obstacle depends on the wind speed, the ambient static stability (resistance to lift), as well as the height and the width of the obstacle (Whiteman, 2000). Based on laboratory experiments with two-dimensional flow over an isolated obstacle, Baines (1995) defined regimes of flow responses to two-dimensional terrain as a function of two non-dimensional parameters describing the upwind flow properties and the geometry of the obstacle: “Lee-side separation”, “Post-wave separation”, and “No separation”. As shown in Figure 3.2, the occurrence of these regimes depends on the obstacle’s aspect ratio $\mathscr{A} = h_0/A_d$ and on the non-dimensional mountain height (inverse Froude number) $\mathscr{N} = Nh_0/U$. Here, h_0 is the obstacle height, A_d the leeside mountain half-width, N the Brunt-Väisälä frequency, and U the wind speed. The same regime classification turns out to be valid for flow past a three-dimensional mountain (Hunt & Snyder, 1980; Baines, 1995; Prestel & Wirth, 2016). Out of the three regimes, banner clouds only occur in the "Lee-side separation" regime, since their formation requires extended leeside uplift all the way to the mountain summit (Voigt & Wirth, 2013).

While theoretical concepts and numerical simulations are consistent with each other, there has been - so far - a lack of detailed observations of the banner cloud phenomenon including the associated flow field. Fortunately, the development of smaller and more mobile Doppler wind lidars in the past decade has facilitated the deployment of such equipment in complex terrain and allowed advances in applications such as wind energy, fire weather, and mountain hydrology (Gerber et al., 2017; Lareau & Clements, 2017; Whiteman et al., 2018; Kristianti et al., 2023, 2024; van Schaik et al., 2025).

Given these more recent developments, we explored the possibility of an observational campaign to study banner clouds. Our focus was on the Matterhorn near Zermatt, Switzerland, one of the most iconic peaks in Europe and worldwide. As is well known, the Matterhorn features frequent occurrence of banner clouds. Despite being one of the highest peaks in the Swiss Alps (4478 m ASL), the Matterhorn is rather well accessible due to the infrastructure catering to skiers, hikers, and mountaineers visiting Zermatt. In 2018 we conducted exploratory measurements proving the fundamental feasibility of direct observation of the flow in the vicinity of a banner cloud at the Matterhorn. Based on these preliminary investigations, we received funding from the German Research Council (Deutsche Forschungsgemeinschaft, DFG) to conduct a low-cost and focused field campaign called the MatterHorn EXperiment (MatterHEX). The key objective of this

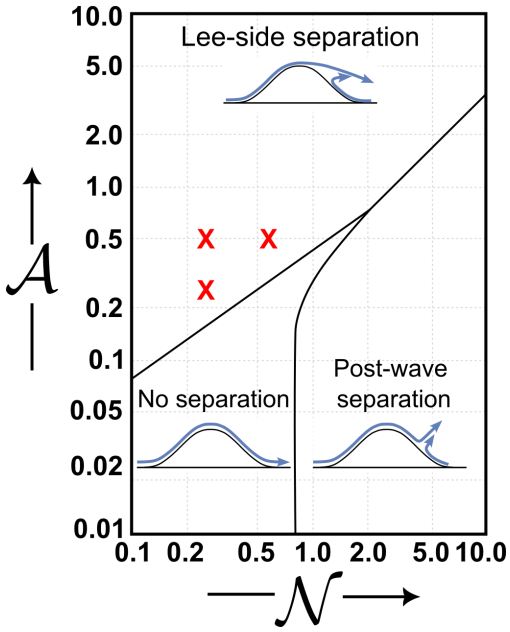

FIGURE 3.2: Diagram of flow separation properties as a function of the inverse Froude number $\mathcal{N}$ and mountain aspect ratio $\mathcal{A}$, adapted from Fig. 5.8 of Baines (1995). The red crosses indicate conditions which are conducive to banner cloud formation in idealized simulations using a three-dimensional obstacle (Prestel & Wirth, 2016).

campaign was to observe the mean leeside flow features resulting from the interaction of a well-characterized background flow with the topography of the Matterhorn. A further motivation was to collect a dataset that would be suited to evaluate Large-Eddy Simulations in extreme complex topography.

The global COVID-19 pandemic delayed our campaign, and we had to wait until fall 2023 to conduct the experiment. We were further constrained by having to avoid the main tourist season while minimizing the risk of being shut down due to an early onset of winter. An additional challenge was the need to coordinate upper-air soundings with the busy helicopter traffic related to tourism, mountain rescues, and infrastructure maintenance.

It is the goal of this paper to provide an overview over the MatterHEX campaign and to present the key findings. A more detailed comparison of the observations with LES model simulations can be found in **Thomas et al. (2025)** [chapter 4]. Of the many banner cloud cases during MatterHEX, we highlight the 3 October 2023 case to describe the observed mean leeside flow structure as well as selected turbulent characteristics of the flow. Finally, we relate our observations to theory.

3.5 Experimental Design and Observations

We received permission for the three-week MatterHEX field campaign between 25 September and 15 October 2023, as well as for one-week setup and take-down phases. Logistical issues delayed the helicopter lifts to the field sites, and routine observations did not start until 29 September

Based on the wind climatology for September and October (Fig. 3.3) and the available infrastructure on the eastern side of the Matterhorn, we designed the experiment for a westerly flow regime. The challenge was to find suitable but accessible locations for the key instrumentation needed to meet our objectives. These were (1) a location for an upwind radiosonde operation, (2) locations for webcams with good view of the east face of the Matterhorn, and (3) accessible

and stable terrain as close as possible to the east face of the mountain to place remote wind sensing equipment with a limited range. The selection of these observation sites is discussed in the following section, and site and instrument details are given in Tables 3.1 and 3.2.

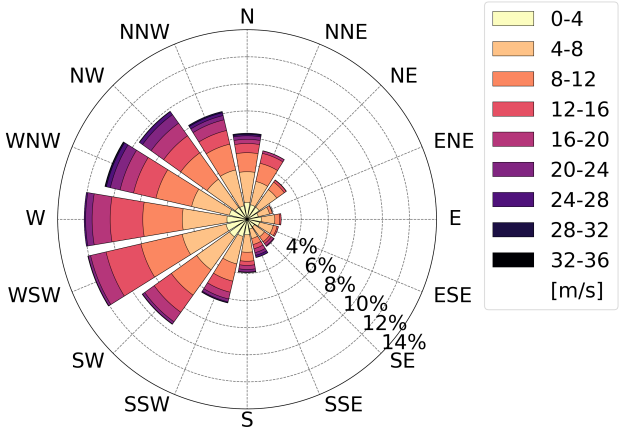

FIGURE 3.3: ERA5 reanalysis 600 hPa wind climatology at lat=45.9° lon=7.55° for 15 September through 15 October covering the period 1993-2023.

TABLE 3.1: MatterHEX sites, site name abbreviations, their coordinates, and elevations.

Observation Site	Latitude	Longitude	Elevation (ASL)
Schönbielhütte (RS)	46.002° N	7.629° E	2694 m
Furggsee (L)	45.974° N	7.695° E	2887 m
Trockener Steg (TS)	45.971° N	7.722° E	2939 m
Hirli (C)	45.989° N	7.699° E	2765 m

TABLE 3.2: Observational components, targeted processes, instrumentation, and measured variables.

Observational component	Targeted Process	Instrument	Location	Variables	Manufacturer	Model
Upwind flow conditions	Wind profile, stratification	Radiosonde	Schönbielhütte (RS)	P, T, RH, u, v	Graw	DFM-09
Leeside flow response	Leeside flow field, wind profile	Doppler wind lidar	Furggsee (L), Trockener Steg (TS, 7-14 Oct)	Radial velocity, aerosol backscatter, VAD wind retrieval	Halo Photonics	Streamline XR
	Leeside wind profile	Doppler wind lidar	Furggsee (L)	VAD wind retrieval	Vaisala	Windcube V2.1
	Banner cloud formation	Webcam	Furggsee (L), Hirli (C)	Pictures	Microseven	M7B5MP-PSAA
	Near surface turbulence	Sonic Anemometer	Furggsee (L)	u, v, w, T	Campbell Scientific	CSAT3

3.6 Upwind Observations

We decided to observe the relevant upwind conditions by launching radiosondes from the Schönbielhütte (RS in Fig. 3.4), a mountain hut of the Swiss Alpine Club, which can be reached in a 4.5-hour hike from Zermatt. The Schönbielhütte is located at 2694 m ASL on the northern slope of the east-west oriented Zmutt valley northwest of the Matterhorn. By the start date of the campaign the hut was already closed for the season, but we were allowed to use its winter room. Provisions as well as cooking fuel were flown in by helicopter, together with the scientific equipment, a small generator, and the helium cylinders needed for the radiosonde operation. Water was

available from a natural well near the hut. Two group members stayed at the hut to perform the upper-air soundings.

Upwind conditions were observed with radiosondes (GRAW DFM-09) that measured air temperature, relative humidity, wind speed and direction as a function of height. The timing of the launches was based on the forecast of westerly flow as well as the occurrence of banner clouds under various flow conditions.

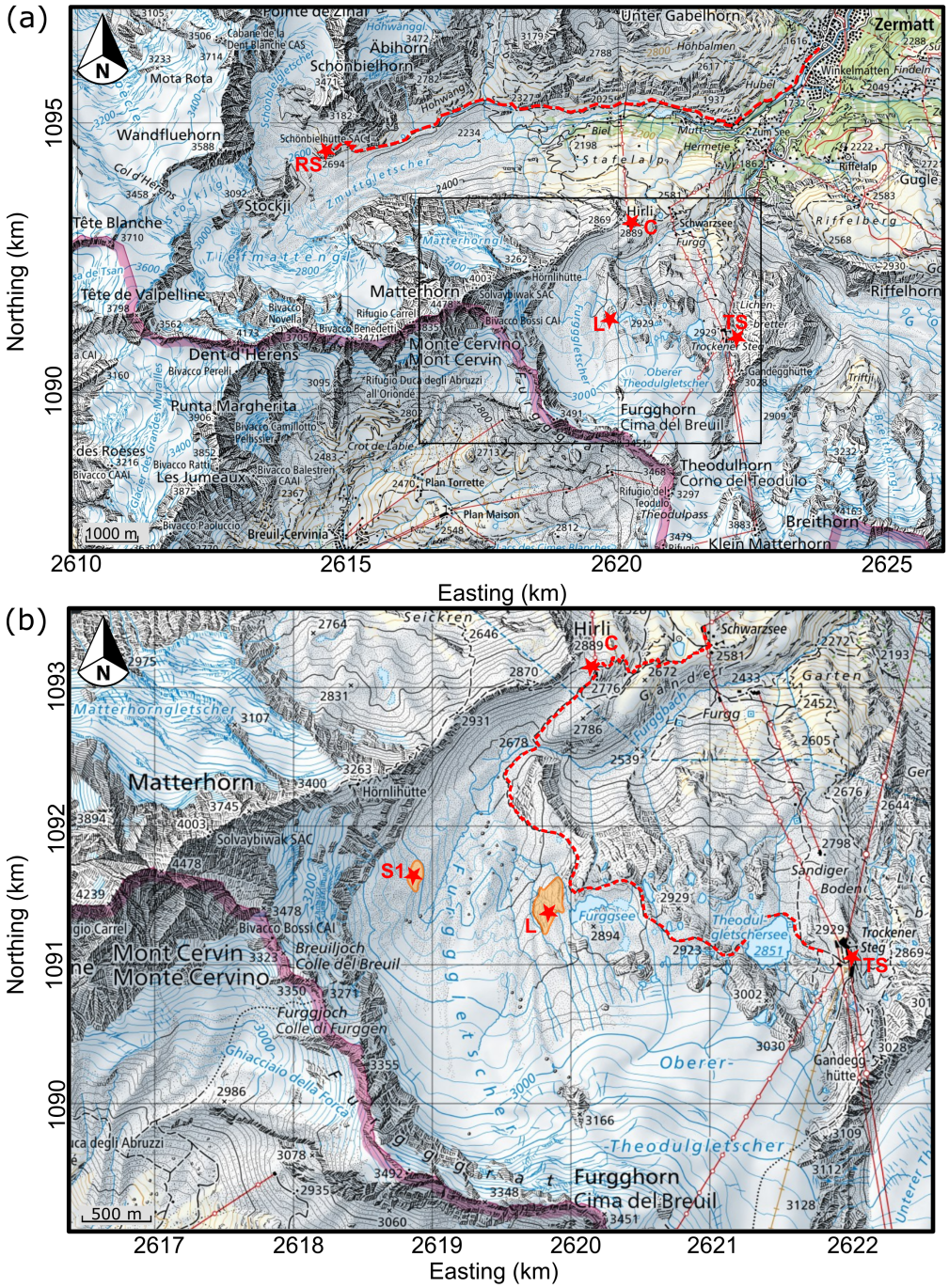

FIGURE 3.4: Maps showing (a) the Matterhorn region with the distribution of both up- and downwind observational sites, and (b) a zoom into the terrain on the lee of the Matterhorn with the location of the instrumentation used to monitor the leeside circulation. Based on CH1903+ / LV95 maps from the Swiss Federal Office of Topography, swisstopo.

3.7 Downwind Observations

The flow response in the lee of the Matterhorn was remotely sensed using Doppler wind lidar techniques. The principal instrument in use was the University of Utah's Halo Photonics Streamline XR scanning Doppler wind lidar. There were several constraints that limited the choice of an observational site. While smaller lidar units such as ours can be powered using portable generators which offers significant flexibility, we were limited to stable terrain safe from rockfall, with easy access, and well-hidden from hikers. During a scouting visit in summer 2023 we noticed that vast areas of the Furgg glacier on the eastern slopes of the Matterhorn had melted, exposing very loose and unstable debris unsuitable for instrument deployment. However, we identified two potential locations on solid bedrock. While the site closest to the summit pyramid (S1 in Fig. 3.4) offered the best vantage point for observing the underside of a banner cloud, access required crossing meltwater streams with large diurnal variations in runoff and travel over debris-covered ice. We therefore opted for the second-best location. This location, on the western side of Lake Furggsee (L in Fig. 3.4), is easily accessible from a popular hiking trail which connects the Trockener Steg (TS in Fig. 3.4) and Schwarzsee cable car stations. This trail offered safe access even under adverse weather conditions, and no major stream crossings were necessary. The local topography, with sharp drop-offs to the west, allowed for a deployment well hidden from the trail despite its proximity. At a highpoint near this site, near-surface wind and turbulence were measured with an 3D ultra-sonic anemometer (Campbell Scientific CSAT3). The near-surface wind profile was monitored using a 5-beam prism-based lidar retrieval with a Vaisala Windcube V2.1. All instruments, hardware, generators, fuel, provisions, and camping gear were flown in by helicopter.

A second scanning Doppler wind lidar (Lumibird Streamline XR) was deployed during part of the experiment at the roof of the Trockener Steg cable car station — the same location where the exploratory measurements were taken in 2018. This site, while at the edge of the lidar range for flow detection around the summit pyramid of the Matterhorn, offered hard power and easy access under almost any weather conditions. Observations from this location were seen as a backup, in case of a failure of the system installed at the Furggsee location.

3.7.1 Lidar Scanning Strategy

The wind lidar at the Furggsee site was programmed with a repeating scan pattern consisting of three range-height indicator (RHI) and four plan-position indicator (PPI) scans, and a short period of vertical stares (see Table 3.3). This scan pattern was repeated approximately every 7 minutes. In addition, a 6-point PPI scan every 15 minutes was used for a velocity azimuth display (VAD) wind retrieval.

The coverage of the RHI and PPI scans is illustrated in Figure 3.5. These scans were designed to capture the key features of the flow field around the Matterhorn's summit pyramid. One RHI scan was centered on the summit, the other two to the north and south of the summit. The PPI scans were positioned to capture potential flow asymmetries at different elevations and to detect the anticipated flow reversal in the lee of the mountain.

The lidar's range gate length was set to 60 m. While the Streamline XR instrument allows range gates as small as 18 m, we chose 60 m to enhance the returns in the ambient high-altitude and low-aerosol environment. Lidar data was collected using the continuous scanning mode, and scan speeds and acquisition time were chosen to resolve the radial wind velocities at the distance of the Matterhorn summit with a spatial resolution of approximately 30 m. Noise was filtered using a threshold filter, but limited by applying the Density-Based Spatial Clustering of Applications

with Noise (DBSCAN) algorithm (Ester et al., 1996; Alcayaga, 2020; Duscha et al., 2023). More details on the data processing can be found in **Thomas et al. (2025)** [chapter 4].

The additional profiling wind lidar (WindCube V2.1) recorded the wind profile above the Furggsee site up to a height of 300 m above ground at 20 levels. The back-up lidar at Trockener Steg scanned a repeating grid pattern across the summit pyramid using a 60 m gate length, as well as a 6-point PPI for a VAD retrieval of the vertical wind profile.

TABLE 3.3: Lidar scans of scan sequence repeated every 7 minutes.

Scan	Azimuthal Range	Elevation Range	Angular Resolution
RHI 1	266.35°	0° – 52.5°	0.55°
RHI 2	276.35°	0° – 52.5°	0.55°
RHI 3	291.35°	0° – 52.5°	0.55°
PPI 1	256.35° – 296.35°	9°	0.55°
PPI 2	256.35° – 296.35°	16.5°	0.55°
PPI 3	256.35° – 296.35°	23°	0.55°
PPI 4	256.35° – 296.35°	27°	0.55°
Vertical Stare	0°	90°	-

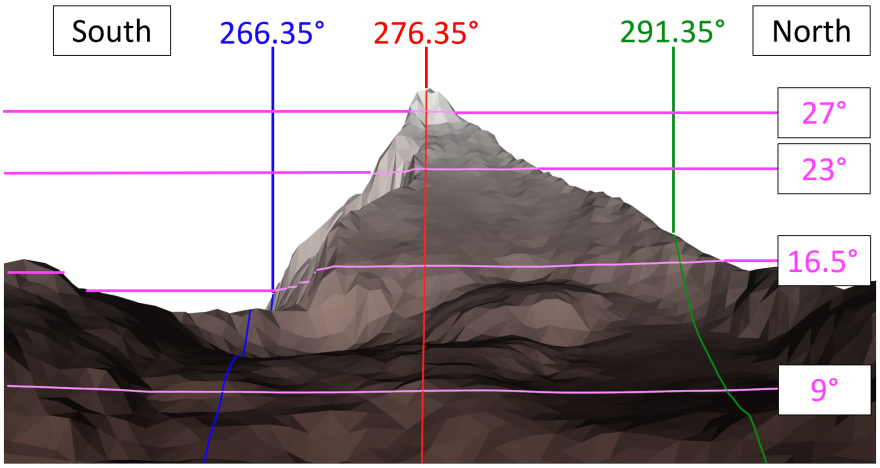

FIGURE 3.5: RHI (blue, red, green) and PPI (pink) scans and their simulated terrain intersections.

3.7.2 Webcams

Time-lapse photography from webcams was used to monitor and document the banner cloud formation and evolution during the field campaign. One camera was co-located with the lidar at the Furggsee site, and a second one was deployed at the upper Hirli cable car station (C in Fig. 3.4), where hard power was available. The combined perspectives from these two vantage points helped to distinguish banner clouds from other low- or mid-level clouds. Both cameras captured time-stamped images every minute, which were transmitted in real time. This allowed us to remotely assess conditions, whether in Zermatt or at Schönbielhütte. The images were later animated into time lapse videos to better visualize the temporal and spatial evolution of the banner clouds. An example video is available as an online supplement.

3.8 Campaign Highlights

In the following we provide highlights from the campaign based on the wind lidar retrievals during the occurrence of banner clouds.

3.8.1 Banner Cloud Occurrence

Banner clouds were observed on eight days of the 17 days of the MatterHEX field campaign, and banner clouds can be identified during 45 hours of webcam imagery. Not all banner clouds were as well defined as the one pictured in Fig. 3.1. There were cases when the banner clouds were very faint, almost sub-visible, and other cases when lower clouds partially concealed a banner-shaped cloud. We even encountered situations reminiscent of a transition from a cap cloud to a banner cloud. Furthermore, banner clouds developed under different prevailing upstream wind directions. Table 3.4 summarizes the banner cloud observations, listing the prevailing wind direction and the launch times of the upwind radiosondes during the event.

TABLE 3.4: Overview of banner cloud episodes observed during MatterHEX.

Date	Banner cloud characteristics	Duration (hours)	Prevailing wind direction	Radiosonde launch time (UTC)
29-Sep	Well defined	3 (1500-1800 UTC)	NNW / NW	1200, 1740, 2000
30-Sep	Faint	4 (1100-1500 UTC)	N / NNW	1200, 1810
3-Oct	Well defined	6 (1200-1800 UTC)	W	1200, 1400
4-Oct	Faint	5 (1200-1700 UTC)	NW / NNW	1815
7-Oct	Cap cloud to banner cloud transition	1 (1130-1230 UTC)	NW / NNW	-
8-Oct	Good	5 (1300-1800 UTC)	NNW / N	-
11-Oct	Very Faint	10 (0500-1500 UTC)	SW	1000, 1320
14-Oct	Good / Obscured	11 (0500-1600 UTC)	W / WSW	0530, 0900, 1210

To give a campaign overview, a time-height cross sections of the vertical profile of wind direction above the Furggsee site is shown in Figure 3.6. Note that the vertical extent of the VAD retrieval was constrained by aerosol availability in this high-altitude environment. However, as cloud droplets greatly enhance lidar reflectivity, the leeside radial flow field within and near a banner cloud edge could frequently be observed, even at times when the lack of aerosols limited the range of the vertical wind profile retrievals further downstream.

In this paper we focus on the 3 October 2023 banner cloud case which was well-suited to describe both the observed mean leeside flow structure and selected turbulent characteristics of the flow.

3.8.2 Leeside Mean Flow Structure

Our lidar scans were successful in resolving the key flow features associated with banner cloud formation as predicted by previous model studies. These are, firstly, the flow reversal in the lee of the mountain, and secondly, the rising motion in the vicinity of the leeside mountain face. Both features are necessary consequences of boundary layer separation at the summit and at the ridgelines as illustrated in the regime diagram (Fig. 3.2).

The mean flow structure is visualized by combining multiple individual lidar retrievals. This has been done for the scans between 1200 and 1800 UTC 3 October 2023, and the composite scans are shown in Figure 3.7. Details on the averaging procedure can be found in **Thomas et al.**

(2025) [chapter 4]. The individual retrievals, and information on the data coverage, are provided in Figures 3.12-3.62 and 3.63 of the supplementary information, respectively.

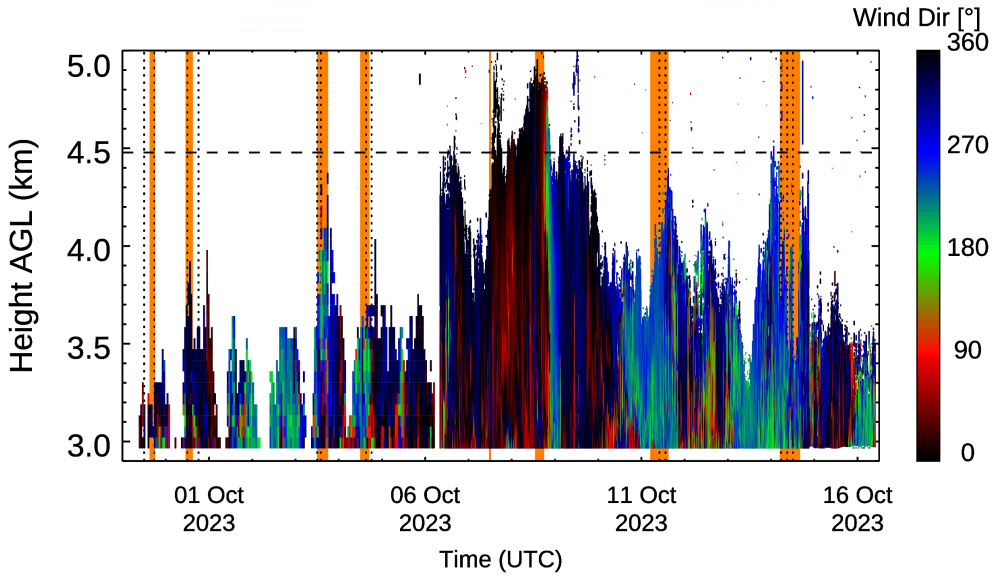

FIGURE 3.6: Time-height cross section of wind direction east of the Matterhorn from Doppler wind lidar at the Furggsee site. Episodes with banner cloud occurrence are highlighted in orange, and radiosonde ascents are indicated as vertical dotted lines. The horizontal dashed line indicates the elevation of the Matterhorn summit.

Since the wind lidar is limited to resolving radial velocities, a unique interpretation may prove difficult. For example, the radial velocities away from the lidar (towards the mountain's lee side) could be explained by either one of the following two extremes: a strong upward motion and no horizontal flow component, or strong horizontal motion towards the mountain and no vertical flow component. However, as the radial velocities remain significant in the direct vicinity of the mountains' east face, and radial velocities in the PPI scans change signs very quickly at the mountain ridgelines, we conclude that these radial retrievals reflect a combination of flow towards the lee slope and upward flow along the lee slope.

The considerable spatial extent of the mean flow towards and upwards along the lee slope apparently allows the air parcels to ascend over a larger vertical distance than at the windward side. This ultimately results in the strongest adiabatic cooling of leeside air parcels, leading to saturation and the formation of the banner cloud. As seen from the underlying individual scans (Fig. 3.12-3.62), the spatial extent as well as the shape of the uplift zone varies greatly with time. Despite the strongly turbulent character of the leeside flow, the time average is consistent with the existence of a banner cloud as observed.

The mean flow patterns shown in Figure 3.7b-d illustrate the flow separation on the ridgelines. This flow separation results in the basic structure of the banner cloud, as the associated shear surfaces in the lee of the mountain separate air masses of different flow history, and hence different moisture content. Entrainment of drier air at the cloud's edges subsequently leads to the evaporation of cloud droplets and the downwind thinning of the cloud banner.

The upwind atmospheric profile from the radiosonde launched during the early part of the episode shows a near neutral boundary layer, capped by a strong increase in potential temperature and wind speed above the Matterhorn summit (Fig. 3.8). As argued in Prestel & Wirth (2016), low atmospheric stability below the mountain summit is conducive to banner cloud formation. Hence, the occurrence of a banner cloud in this specific episode is consistent with these earlier predictions based on theory and numerical simulation.

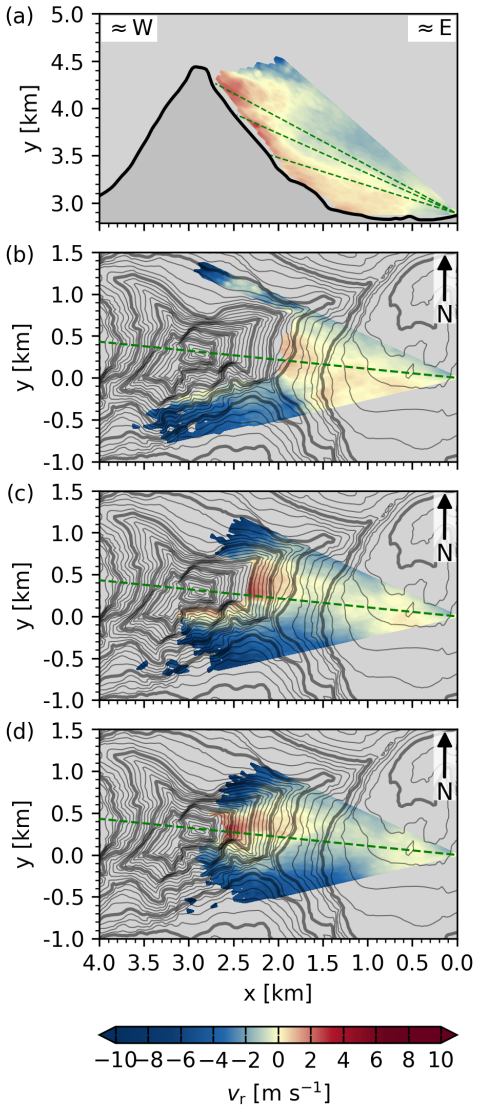

FIGURE 3.7: Mean leeside radial velocities resolved by (a) the range-height indicator scan (RHI) through the summit pyramid, and plan-position indicator scans (PPI) at (b) 16.5°, (c) 23°, and (d) 27° elevation for the period between 1200 and 1800 UTC. Only those grid points are included where data are available for at least 25% of the scans. The x-coordinate in (a) gives the E-W distance, in (b)-(d) the line-of-sight distance from the lidar.

3.8.3 Leeside Turbulent Features

While the primary goal of the observations was to evaluate the mean circulation patterns in the lee of the mountain, we also aimed to capture key turbulent patterns.

On 3 October, we took the photo shown in Figure 3.9 during the hike from Schönbielhütte to Zermatt. It shows how parts of the banner cloud are sheared off, and it suggests that strong overturning leads to a cloud train resembling Kelvin-Helmholtz billows. Indeed, the atmospheric conditions on this day were conducive to Kelvin-Helmholtz Instability (KHI), as indicated by the gradient Richardson number which dropped below the critical threshold of $Ri_c = 0.25$ (Fig. 3.8c). The RHI scan from the time of these observations, shown in Figure 3.9b, reveals a substantial area of upwelling reaching the summit, likely amplifying directional wind shear. This created favorable conditions for this particular banner cloud display, resembling Kelvin-Helmholtz billows. The RHI scan also shows the characteristic ascending and descending portions of the overturning motion at the cloud base.

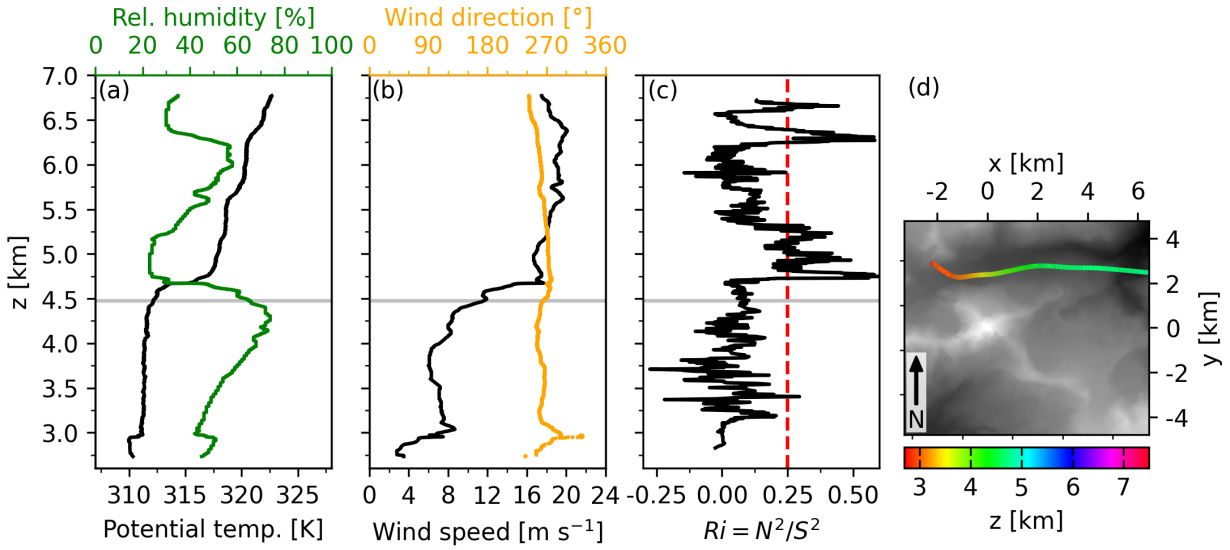

FIGURE 3.8: Upwind vertical profiles at 1358 UTC 3 October 2023 of (a) potential temperature and relative humidity, (b) wind speed and direction, and (c) gradient Richardson number, calculated using a 20-point rolling mean (≈ 100 m). Horizontal gray lines indicate the summit height of the Matterhorn, and the red dashed line in (c) depicts the critical Richardson number Ri_c of 0.25. Panel (d) shows the ascent path of the radiosonde, with coordinates centered at the Matterhorn summit and grey shading indicating topography.

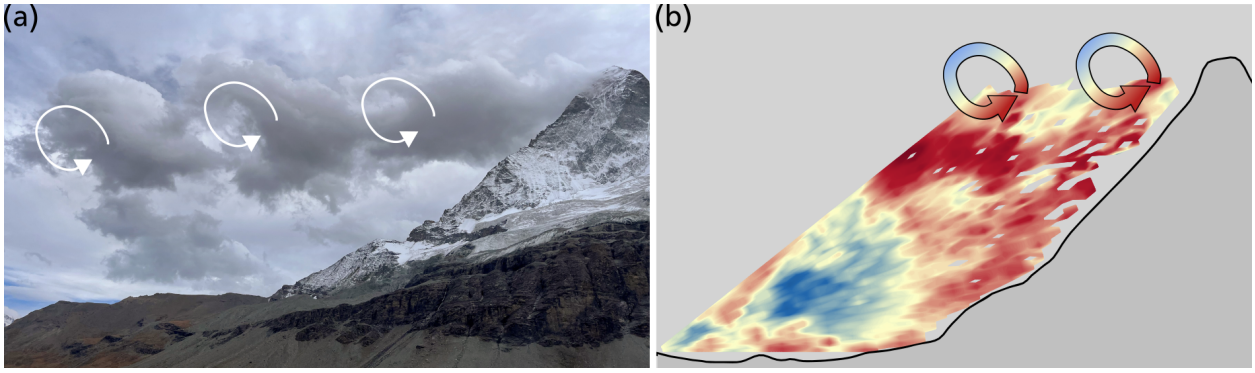

FIGURE 3.9: Analysis of turbulent cloud features at 1506 UTC 3 October 2023: (a) Photograph of a banner cloud pattern resembling Kelvin-Helmholtz billows, and (b) RHI scan through the Matterhorn summit.

Strong overturning motion can also be detected directly above the Furggsee lidar site. Vertical velocities from stare scans, shown in Fig. 3.10, highlight strong vertical speed oscillations consistent with the passing of overturning eddies. Vertical velocities exceed 5 m s^{-1}, indicating vigorous mixing.

As the lidar scans only resolve radial velocities, inferring the full three-dimensional flow pattern can be challenging, especially as turbulent structures evolve within and between individual scans. Additional lidar observations implementing dual-, or triple-Doppler approaches (Hill et al., 2010; Cherukuru et al., 2015; Wang et al., 2016) would be very helpful. Similarly, the combination of lidar observations with numerical Large-Eddy Simulations adds to the understanding of the complex flow patterns (**Thomas et al. (2025)** [chapter 4]).

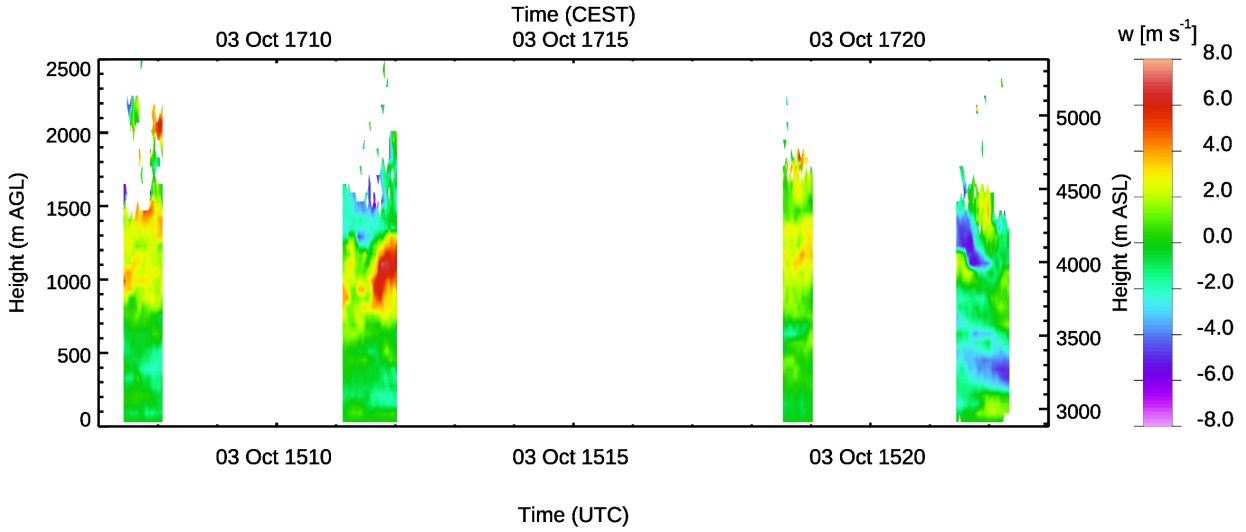

FIGURE 3.10: Vertical velocities from stares above the Furggsee lidar site between 1507 and 1525 UTC 3 October 2023.

3.9 Synthesis

Let us come back to the regime diagram in Fig. 3.2, which illustrates why steep mountains like the Matterhorn (i.e. large $\mathscr{A}$), are more likely to exhibit a banner cloud in their lee than mountains with a lower aspect ratio: Leeside flow separation occurs under a much wider range of stratification for any given wind speed U (i.e. allowing larger $\mathscr{N}$). As Baines (1995) points out, the regime boundaries are approximate and depend on the obstacle's exact shape. In real complex topography, the relevant aspect ratio of a mountain will vary with the direction of the flow. With this in mind, we can now go a step further and explore the dependence of banner cloud formation on wind direction at the Matterhorn. Figure 3.11a illustrates how the specific topography of the Matterhorn controls the height and width scales (h_0 and A_d), and thus $\mathscr{A}$ as a function of wind direction and distance from the summit. Following Baines (1995), leeside separation occurs when $2\pi U/N$ is smaller than the leeside mountain half-width, A_d. This sets the upper threshold value for $\mathscr{N}$, namely $\mathscr{N}_{lim} = \pi\mathscr{A}$, which may not be exceeded for the flow to remain within the "leeside separation" regime and, thus, for banner cloud occurrence. As $\mathscr{N}_{lim}$ is proportional to $\mathscr{A}$, Figure 3.11a also shows the variation of the threshold value $\mathscr{N}_{lim}$ for different flow directions on the Matterhorn. This allows us to calculate a directionally smoothed mean of $\mathscr{N}_{lim}$, $\langle\mathscr{N}_{lim}\rangle$, for a 2-km radius around the Matterhorn summit. Analyzing this $\langle\mathscr{N}_{lim}\rangle$ we conclude that banner clouds can form under a wider range of $\mathscr{N}$ for northerly or southerly flows as $\langle\mathscr{N}_{lim}\rangle$ is larger (Fig. 3.11b); for westerly and easterly flows, $\langle\mathscr{N}_{lim}\rangle$ is smaller by comparison, suggesting that for these wind directions banner cloud formation is less likely, and more sensitive to the balance between the wind speed U and the Brunt-Väisälä frequency N.

We can now use our upwind observations to evaluate whether the flow conditions fall into the leeside separation regime, and thus, if conditions are conducive to banner cloud formation. Figure 3.11b shows that only two of our upwind profiles result in $\mathscr{N}$ values exceeding the threshold level $\langle\mathscr{N}_{lim}\rangle$, and thus preventing banner cloud formation. All the other profiles fall into the banner cloud-permitting leeside separation regime, including four cases during which no banner clouds were visually observed. On these four days, upwind relative humidity levels tended to be lower (not exceeding 40% relative humidity in the 750 m below the summit) than on days when banner clouds were observed (Fig.3.64-3.75). On 11 October, the banner cloud was very faint, and humidity levels peaked at just 45%. These observations indicate that the circulation patterns responsible

for banner cloud formation are likely to occur more frequently than their actual occurrence would suggest.

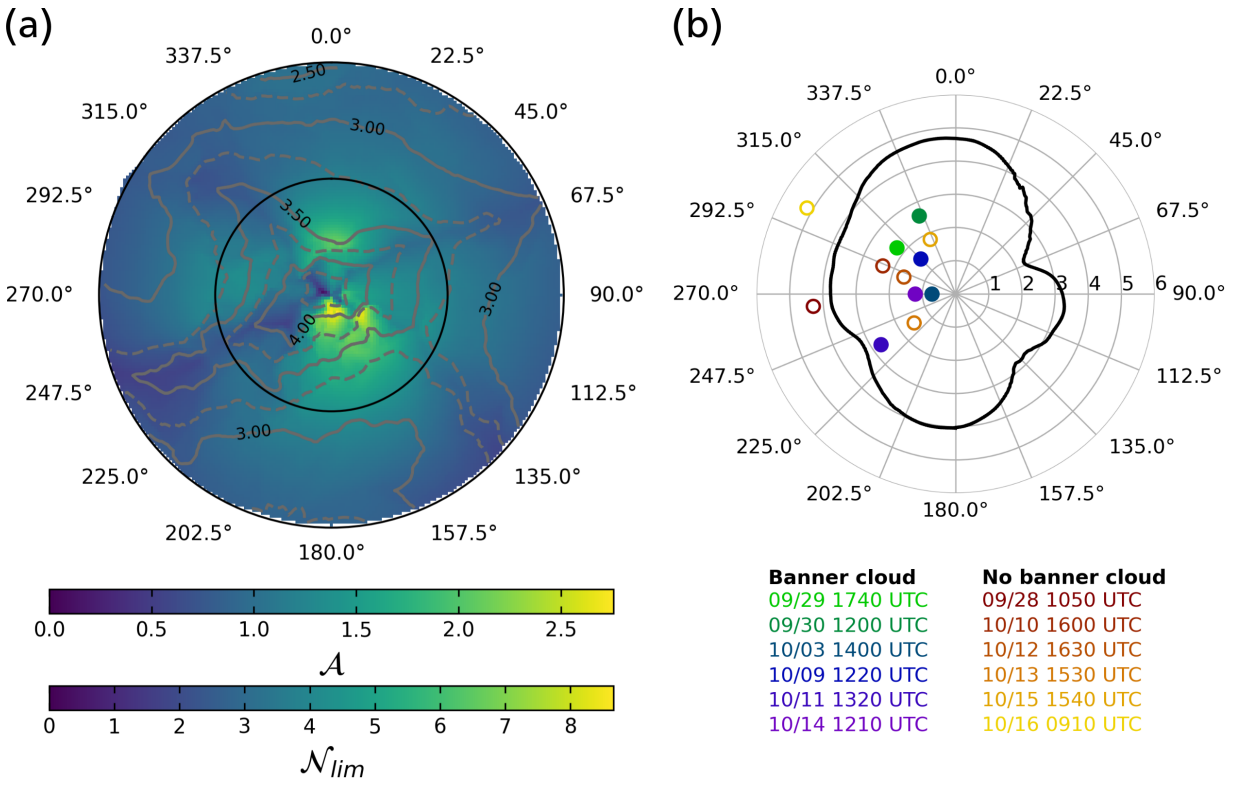

FIGURE 3.11: Analysis of regime conditions and banner cloud occurrence during the MatterHEX campaign. Panel (a) shows the directional dependence of the leeside mountain aspect ratio $\mathcal{A}$ and of the upper threshold value of $\mathcal{N}$, $\mathcal{N}_{lim}$, for leeside flow separation within a 2-km radius around the summit. Panel (b) shows the directional variation of the spatially averaged $\mathcal{N}_{lim}$, $\langle \mathcal{N}_{lim} \rangle$ (2-km distance average with 5° directional smoothing). Circles in (b) indicate $\mathcal{N}$ from upwind observations with (filled) and without (empty) visual banner cloud occurrence. Upstream $\mathcal{N}$ was calculated using the mean U and the mean N between 3000 m ASL and the Matterhorn summit (4478 m ASL). Alternative methods for determining U and N led to very similar results (not shown).

3.10 Summary and Conclusions

This paper summarizes the design and execution of a high-risk, high-reward field experiment addressing the flow-terrain interactions responsible for the frequent formation of banner clouds on steep mountains such as the iconic Matterhorn of the European Alps. A key instrument in this endeavor was a Doppler wind lidar system. Such systems, which have become commercially available in the last decades, allow remote sensing of circulation patterns in highly complex terrain, even at elevations with reduced aerosol loading. Our lidar was used to retrieve radial wind components of the flow around the Matterhorn. Temporal averages of these retrievals were used to resolve the mean flow structures during banner cloud episodes. The observed mean structures suggest strong flow reversal and extensive upward motion in the lee of the Matterhorn, consistent with previous numerical simulations. Individual lidar retrievals resolved the highly turbulent character of the leeside circulation and indicated turbulent structures resembling Kelvin-Helmholtz billows.

We further categorized our observed upwind flow conditions in terms of the regimes of Baines (1995) while taking the effects of the varying obstacle aspect ratio with wind direction into account. As it turns out, all banner cloud cases fit well within the regime of “leeside flow separation” which

is conducive to banner cloud formation. At the same time, our observations suggest that the flow regime promoting the generation of banner clouds is more prevalent than the actual occurrence of banner clouds may indicate. This is because the availability of moisture can be insufficient for condensation to occur despite the large leeside vertical displacement. These findings emphasize the prevalence of extensive leeside rising motion even in the absence of banner clouds. Our observations show that this mean lift in the lee may easily be obscured by strong turbulent eddies and overturning, involving strong changes of vertical velocity over short distances. This emphasizes the danger to leeside air travel, even when clouds may not be visible.

The data collected during MatterHEX resolves the relevant spatiotemporal scales associated with the flow interactions in extremely complex terrain. It is therefore well suited for the evaluation of Large-Eddy Simulations, which in turn may offer a more refined and complete picture of the flow in the complex terrain of the Matterhorn. Such a study is presented in a follow-up paper by **Thomas et al. (2025)** [chapter 4].

We hope to have demonstrated that meaningful observations of flow in highly complex terrain can be made by combining modern equipment with careful campaign design. Given the continuous advances and miniaturization of observational platforms, this bodes well for a bright future in observational mountain meteorology.

3.11 Acknowledgments

MatterHEX was funded by grant 432130757 of the Deutsche Forschungsgemeinschaft (DFG, German Research Foundation). SWH was partially supported by the NSF National Center for Atmospheric Research, which is a major facility sponsored by the U.S. National Science Foundation under Cooperative Agreement No. 1852977. We thank Bernhard Arnold and Romy Biner-Hauser (Gemeinde Zermatt), Air Zermatt, Fredy and Yolanda Biner-Perren (Schönbielhütte SAC), and Reinhard Lauber (Zermatt Bergbahnen AG) for invaluable logistical support. We could not have realized these observations without their support.

3.12 Data Availability Statement

All data is available upon request. [See data availability statement in section 4.9].

3.13 Supplementary Material

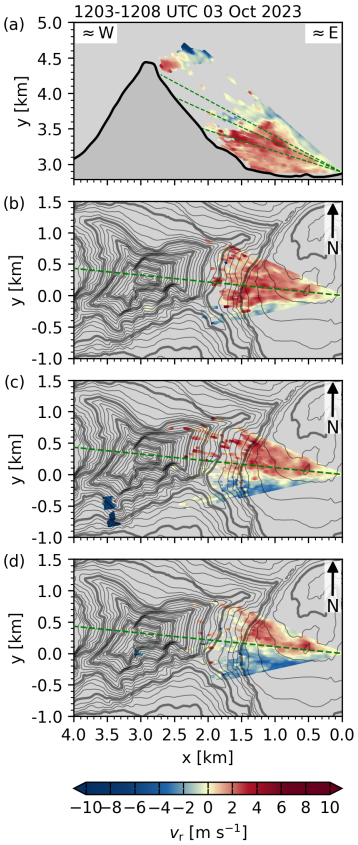

FIGURE 3.12: Lee-side radial velocities resolved by (a) the range-height indicator scan (RHI) through the summit pyramid, and plan-position indicator scans (PPI) at (b) 16.5°, (c) 23°, and (d) 27° elevation for the scan cycle between 1203 and 1207 UTC, 3 October 2023.

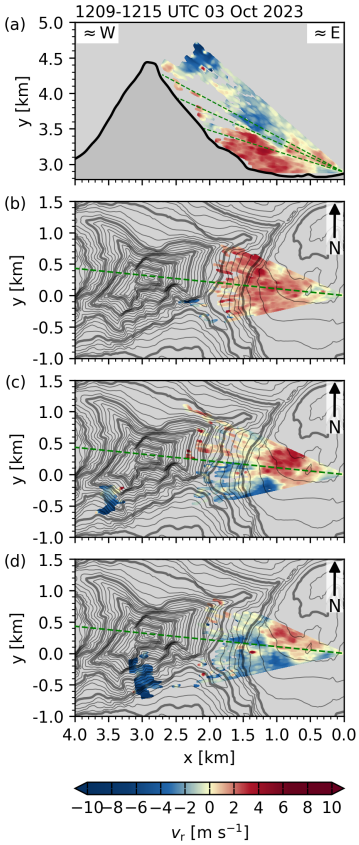

FIGURE 3.13: As Fig. 3.12, but for scan cycle between 1209 and 1215 UTC, 3 October 2023.

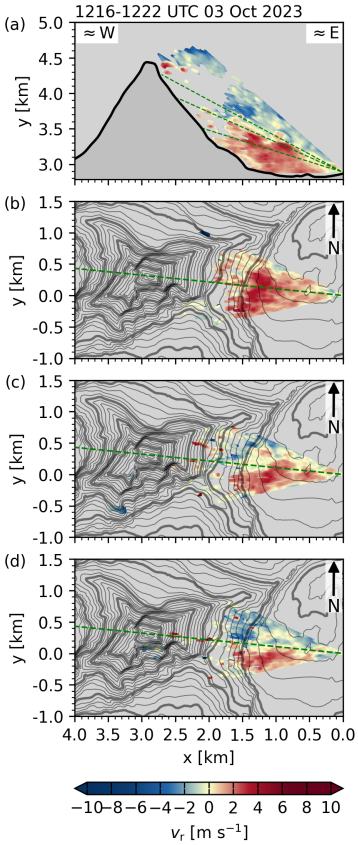

FIGURE 3.14: As Fig. 3.12, but for scan cycle between 1216 and 1222 UTC, 3 October 2023.

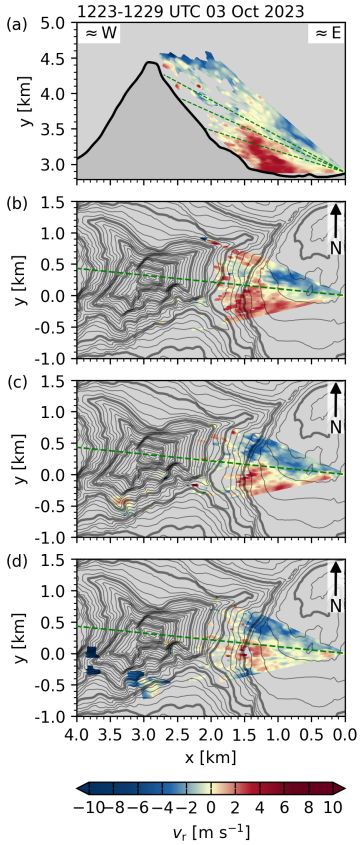

FIGURE 3.15: As Fig. 3.12, but for scan cycle between 1223 and 1229 UTC, 3 October 2023.

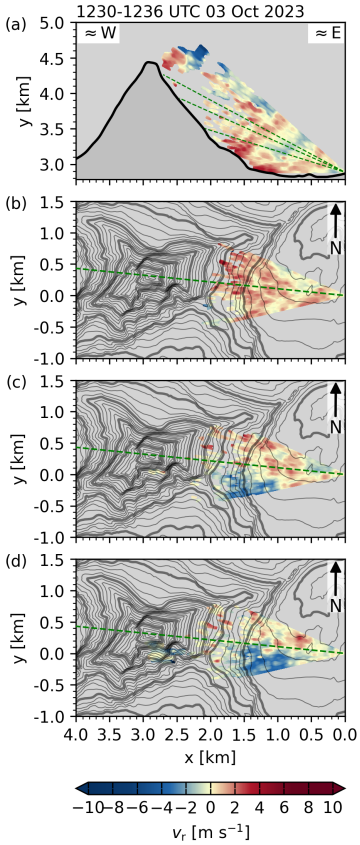

FIGURE 3.16: As Fig. 3.12, but for scan cycle between 1230 and 1236 UTC, 3 October 2023.

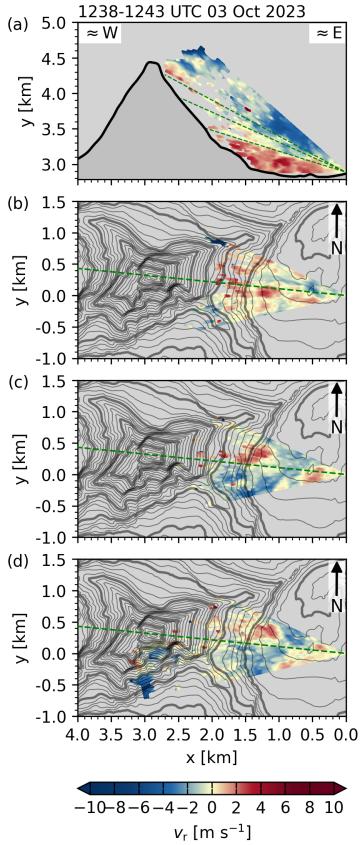

FIGURE 3.17: As Fig. 3.12, but for scan cycle between 1238 and 1243 UTC, 3 October 2023.

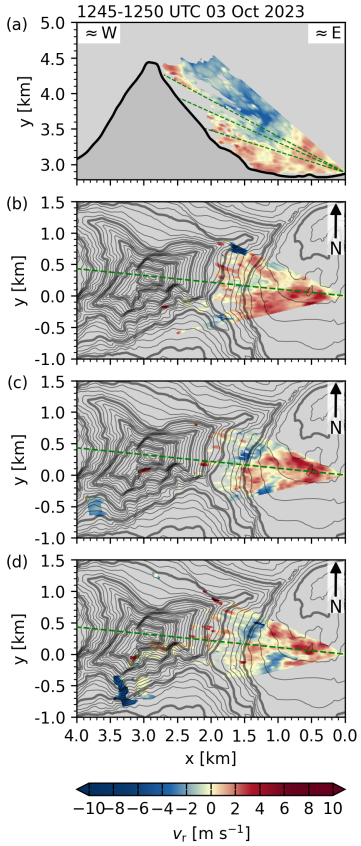

FIGURE 3.18: As Fig. 3.12, but for scan cycle between 1245 and 1250 UTC, 3 October 2023.

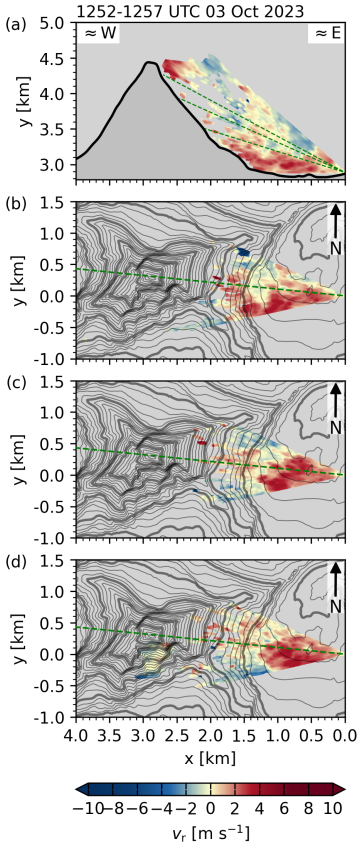

FIGURE 3.19: As Fig. 3.12, but for scan cycle between 1252 and 1257 UTC, 3 October 2023.

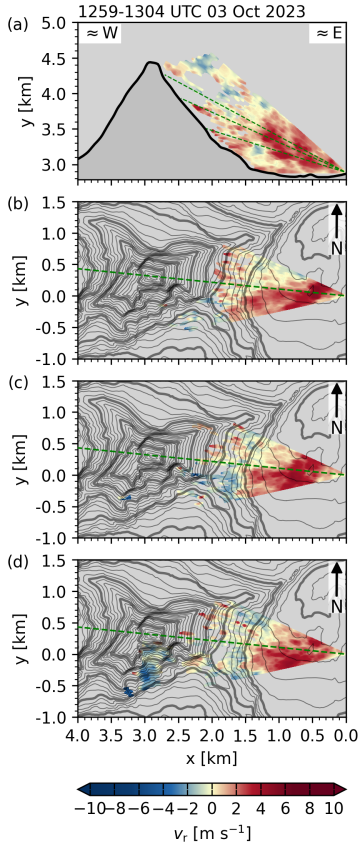

FIGURE 3.20: As Fig. 3.12, but for scan cycle between 1259 and 1304 UTC, 3 October 2023.

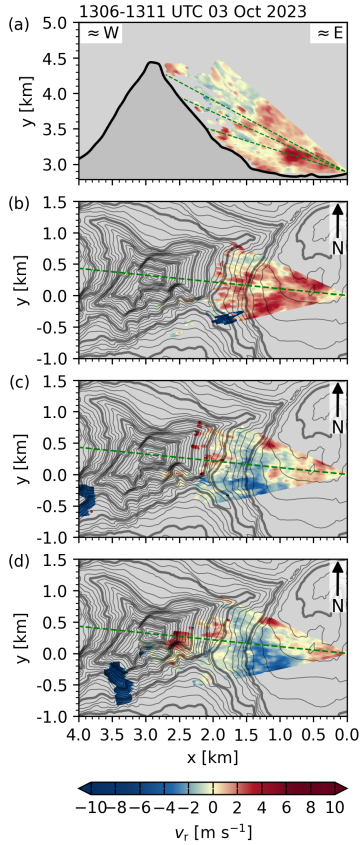

FIGURE 3.21: As Fig. 3.12, but for scan cycle between 1306 and 1311 UTC, 3 October 2023.

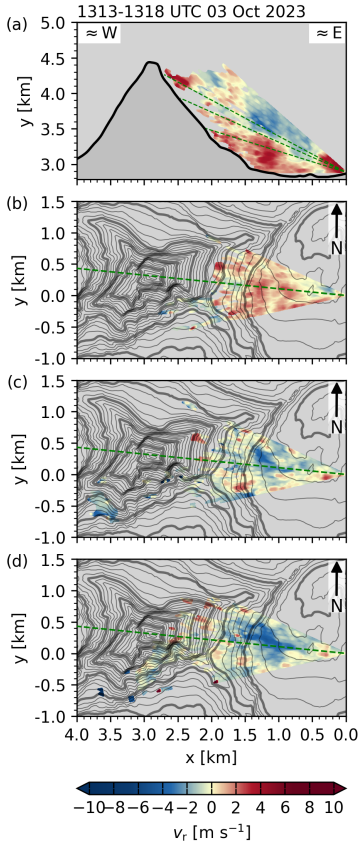

FIGURE 3.22: As Fig. 3.12, but for scan cycle between 1313 and 1318 UTC, 3 October 2023.

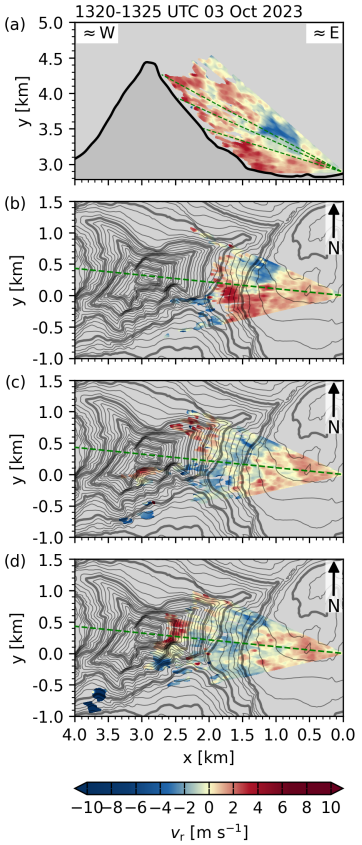

FIGURE 3.23: As Fig. 3.12, but for scan cycle between 1320 and 1325 UTC, 3 October 2023.

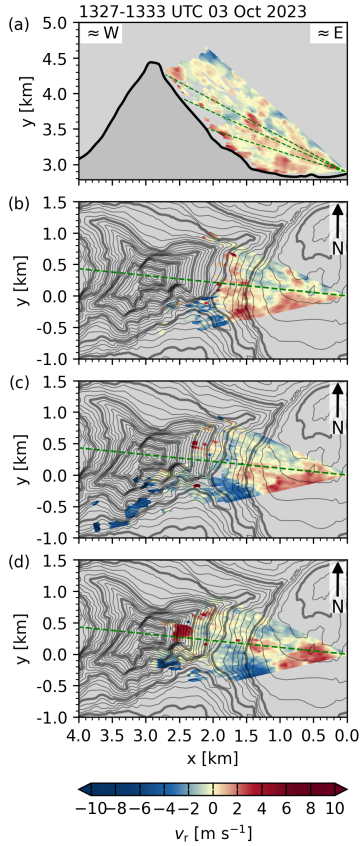

FIGURE 3.24: As Fig. 3.12, but for scan cycle between 1327 and 1333 UTC, 3 October 2023.

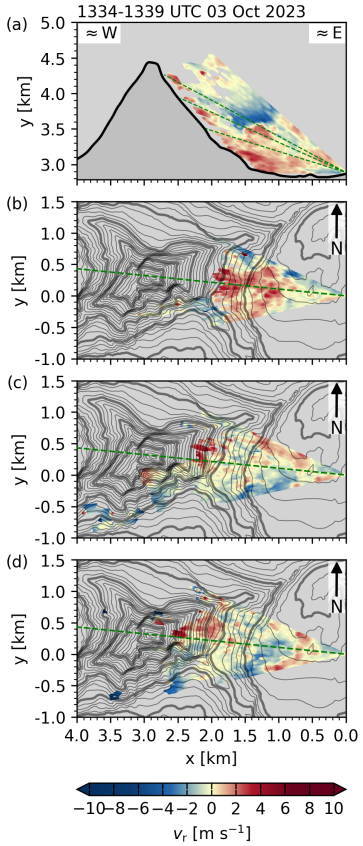

FIGURE 3.25: As Fig. 3.12, but for scan cycle between 1334 and 1339 UTC, 3 October 2023.

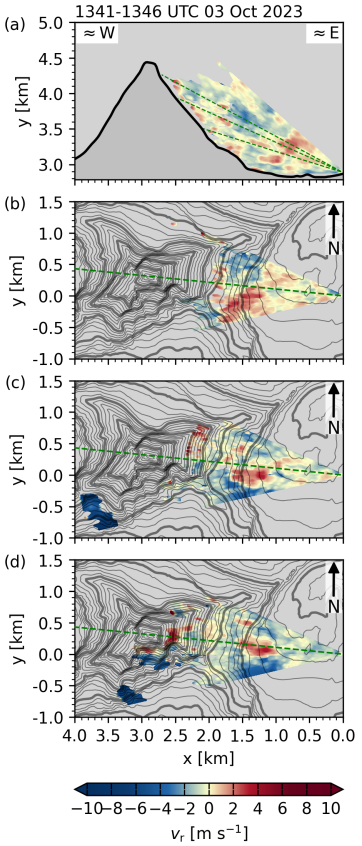

FIGURE 3.26: As Fig. 3.12, but for scan cycle between 1341 and 1346 UTC, 3 October 2023.

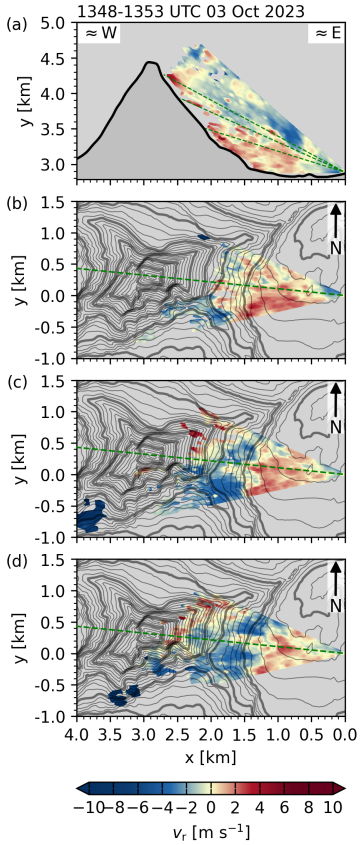

FIGURE 3.27: As Fig. 3.12, but for scan cycle between 1348 and 1353 UTC, 3 October 2023.

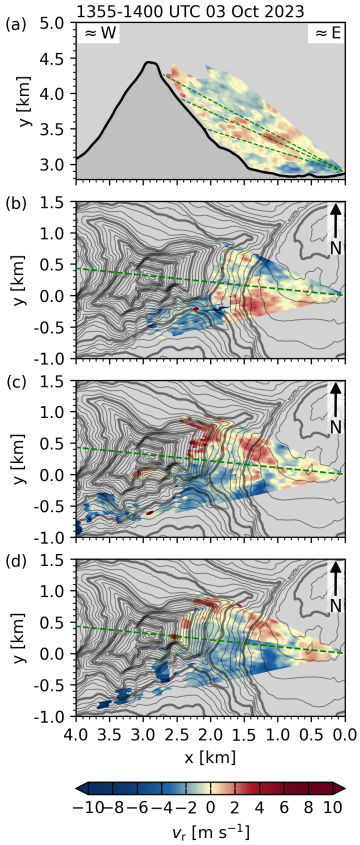

FIGURE 3.28: As Fig. 3.12, but for scan cycle between 1355 and 1400 UTC, 3 October 2023.

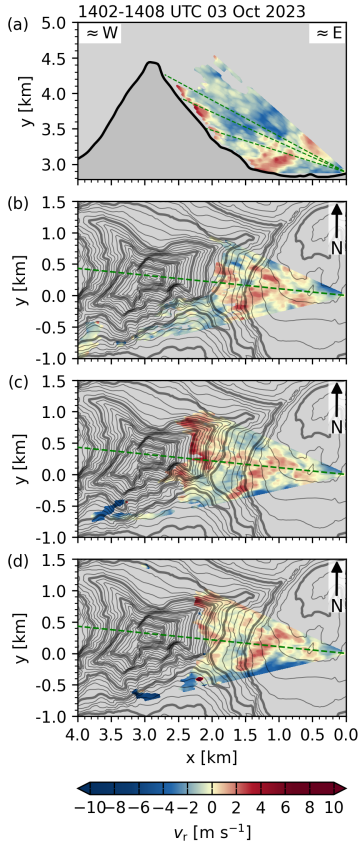

FIGURE 3.29: As Fig. 3.12, but for scan cycle between 1402 and 1408 UTC, 3 October 2023.

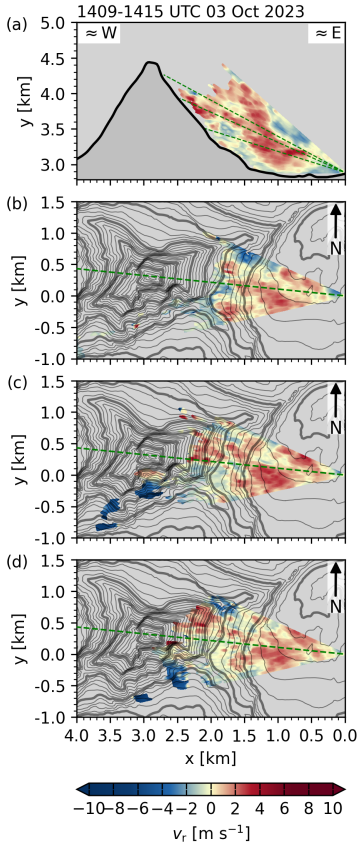

FIGURE 3.30: As Fig. 3.12, but for scan cycle between 1409 and 1415 UTC, 3 October 2023.

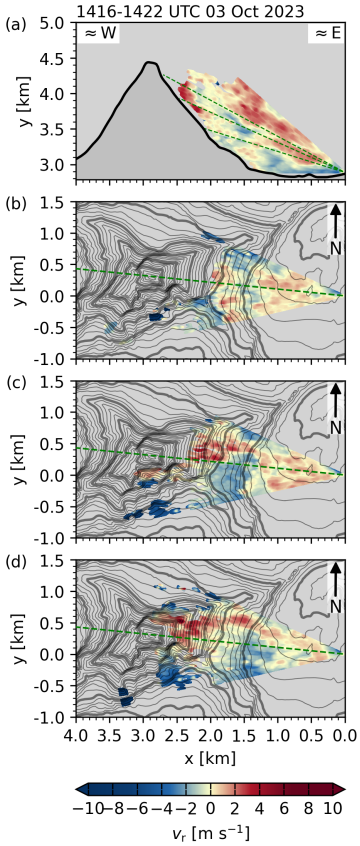

FIGURE 3.31: As Fig. 3.12, but for scan cycle between 1416 and 1422 UTC, 3 October 2023.

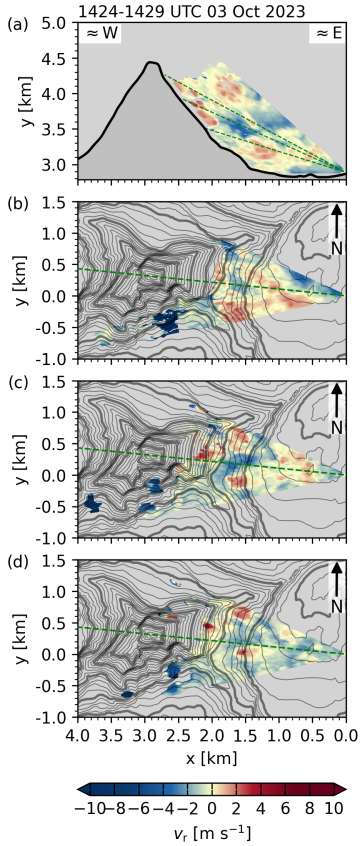

FIGURE 3.32: As Fig. 3.12, but for scan cycle between 1424 and 1429 UTC, 3 October 2023.

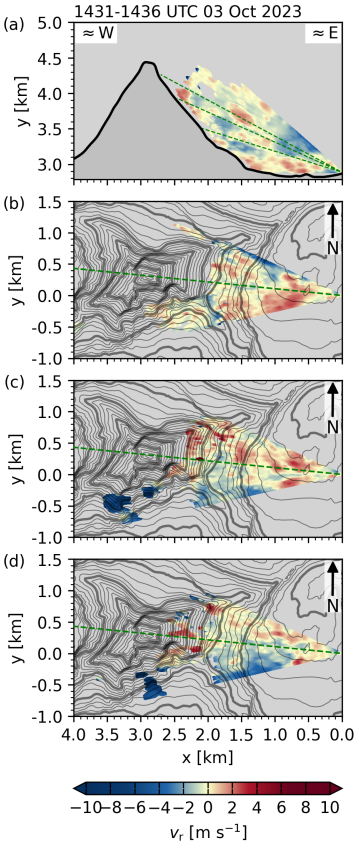

FIGURE 3.33: As Fig. 3.12, but for scan cycle between 1431 and 1436 UTC, 3 October 2023.

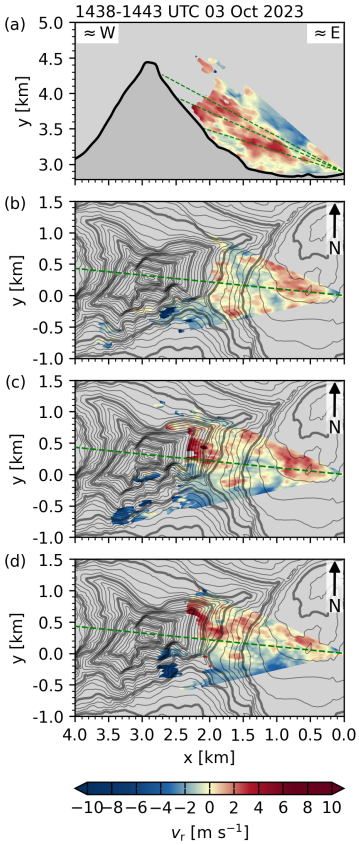

FIGURE 3.34: As Fig. 3.12, but for scan cycle between 1438 and 1443 UTC, 3 October 2023.

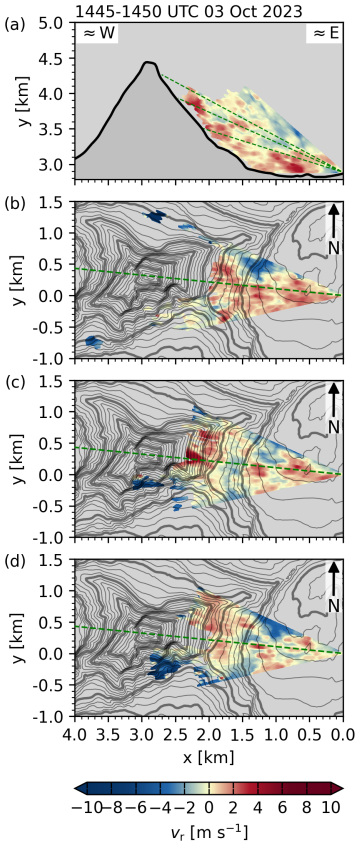

FIGURE 3.35: As Fig. 3.12, but for scan cycle between 1445 and 1450 UTC, 3 October 2023.

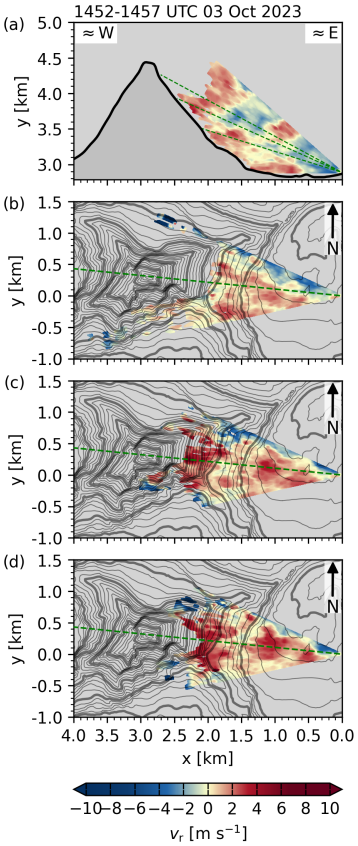

FIGURE 3.36: As Fig. 3.12, but for scan cycle between 1452 and 1457 UTC, 3 October 2023.

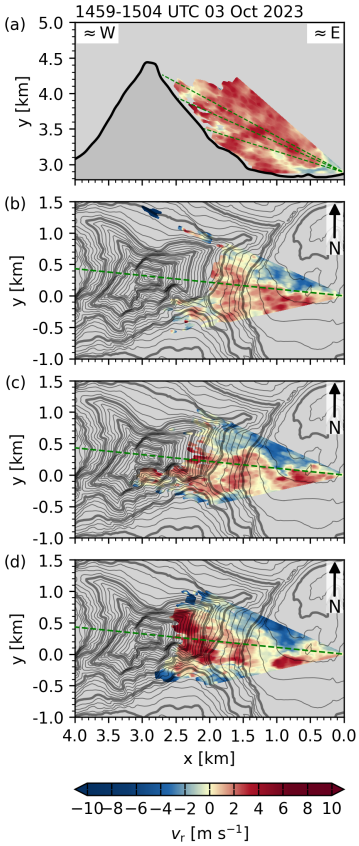

FIGURE 3.37: As Fig. 3.12, but for scan cycle between 1459 and 1504 UTC, 3 October 2023.

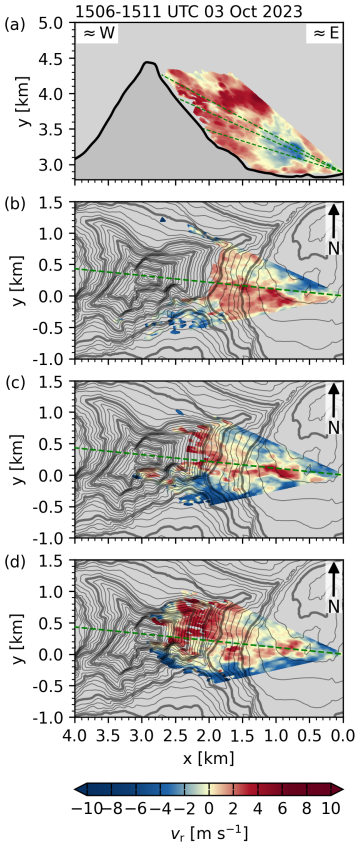

FIGURE 3.38: As Fig. 3.12, but for scan cycle between 1506 and 1511 UTC, 3 October 2023.

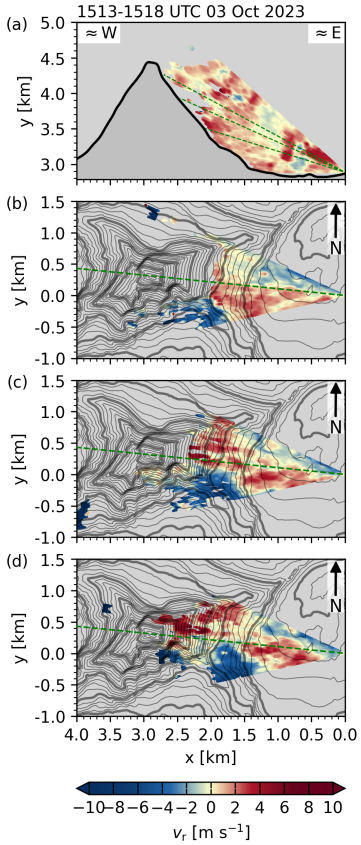

FIGURE 3.39: As Fig. 3.12, but for scan cycle between 1513 and 1518 UTC, 3 October 2023.

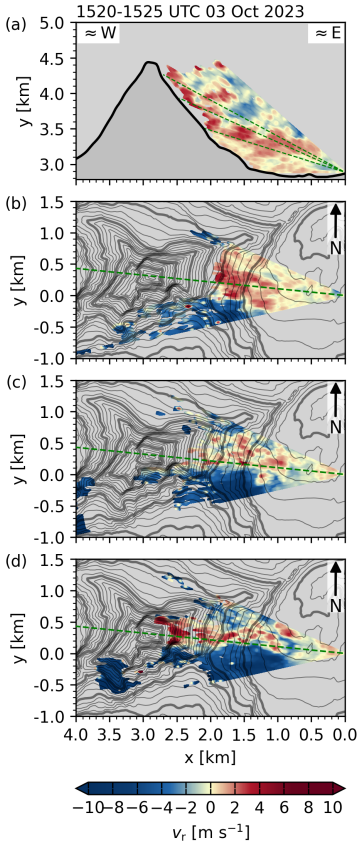

FIGURE 3.40: As Fig. 3.12, but for scan cycle between 1520 and 1525 UTC, 3 October 2023.

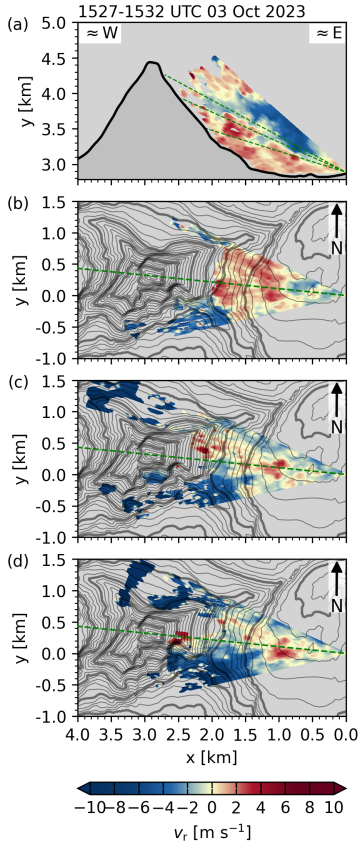

FIGURE 3.41: As Fig. 3.12, but for scan cycle between 1527 and 1532 UTC, 3 October 2023.

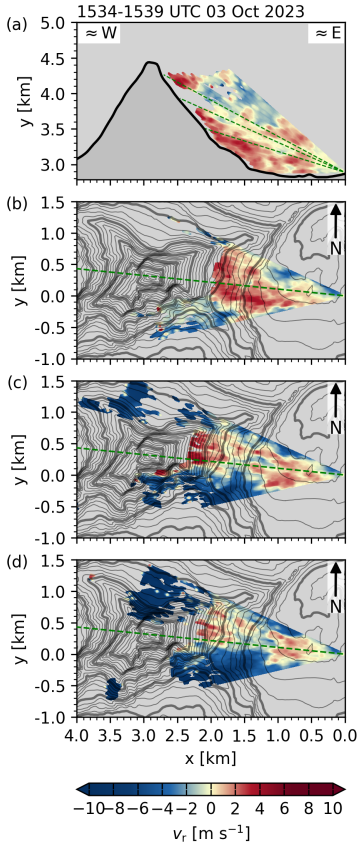

FIGURE 3.42: As Fig. 3.12, but for scan cycle between 1534 and 1539 UTC, 3 October 2023.

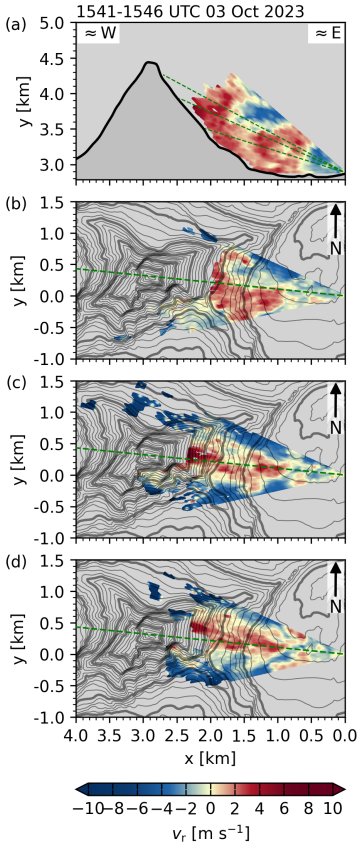

FIGURE 3.43: As Fig. 3.12, but for scan cycle between 1541 and 1546 UTC, 3 October 2023.

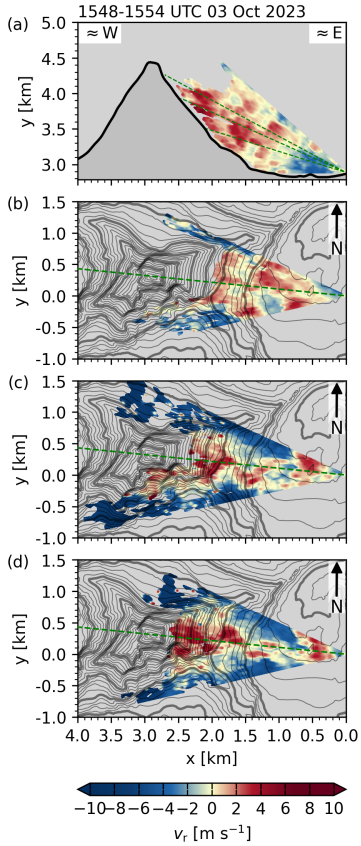

FIGURE 3.44: As Fig. 3.12, but for scan cycle between 1548 and 1554 UTC, 3 October 2023.

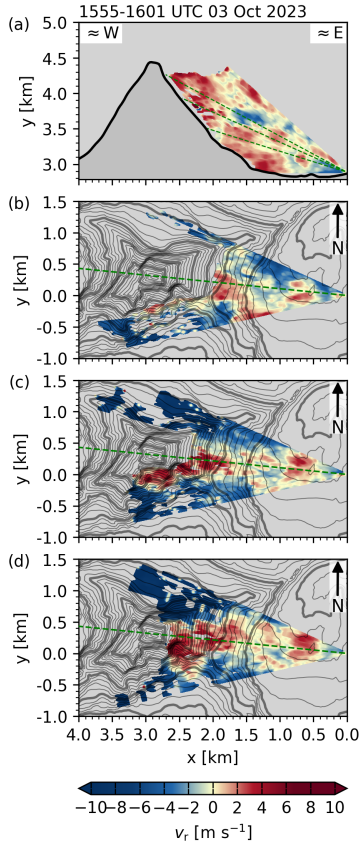

FIGURE 3.45: As Fig. 3.12, but for scan cycle between 1555 and 1601 UTC, 3 October 2023.

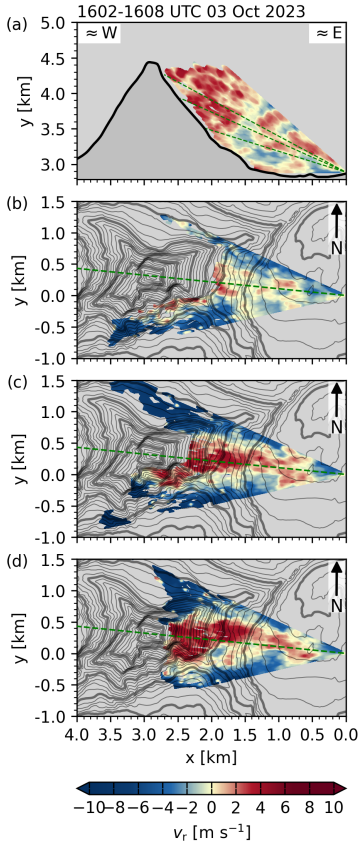

FIGURE 3.46: As Fig. 3.12, but for scan cycle between 1602 and 1608 UTC, 3 October 2023.

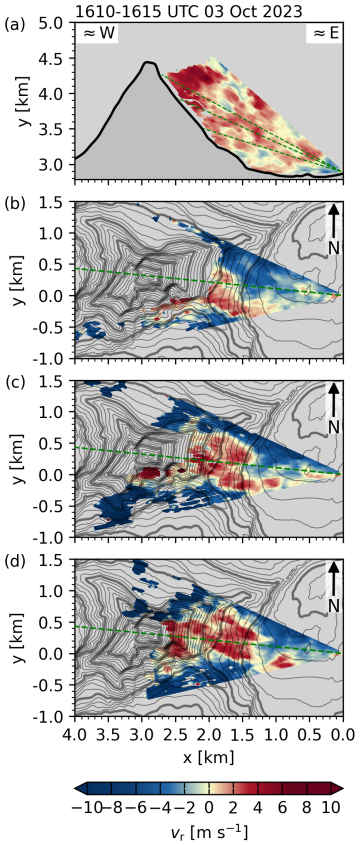

FIGURE 3.47: As Fig. 3.12, but for scan cycle between 1610 and 1615 UTC, 3 October 2023.

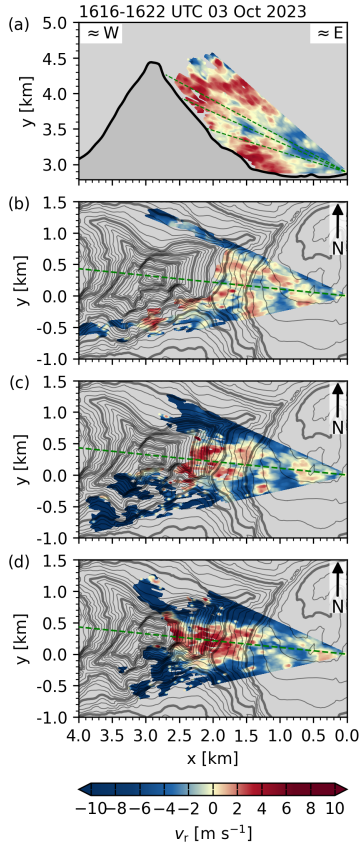

FIGURE 3.48: As Fig. 3.12, but for scan cycle between 1616 and 1622 UTC, 3 October 2023.

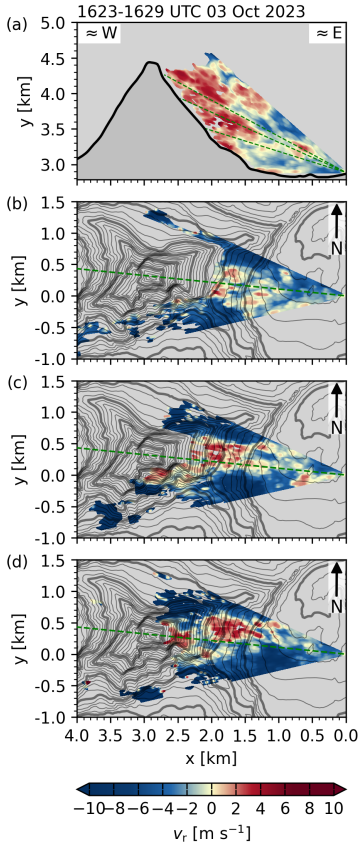

FIGURE 3.49: As Fig. 3.12, but for scan cycle between 1623 and 1629 UTC, 3 October 2023.

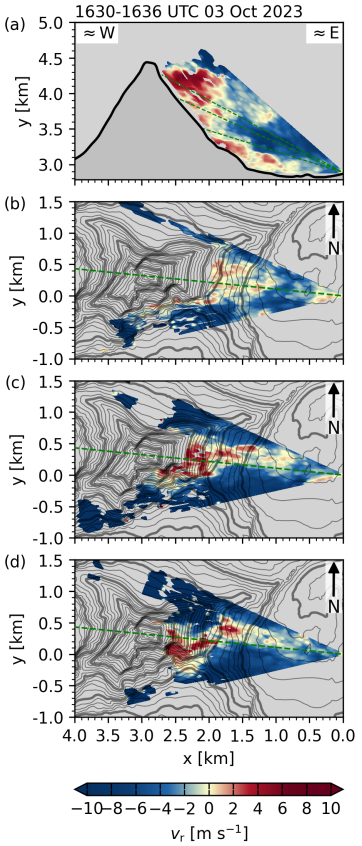

FIGURE 3.50: As Fig. 3.12, but for scan cycle between 1630 and 1636 UTC, 3 October 2023.

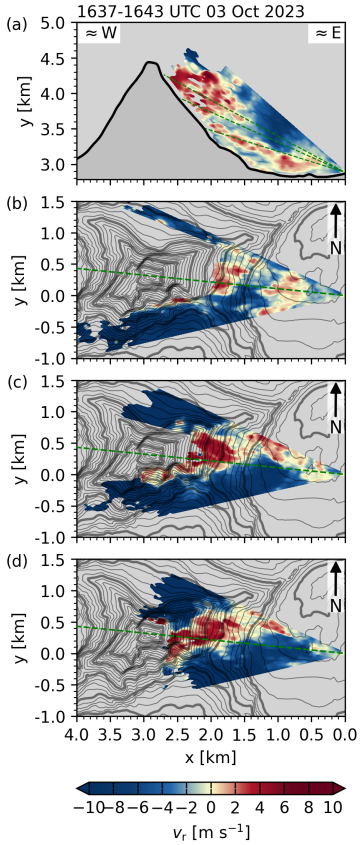

FIGURE 3.51: As Fig. 3.12, but for scan cycle between 1637 and 1643 UTC, 3 October 2023.

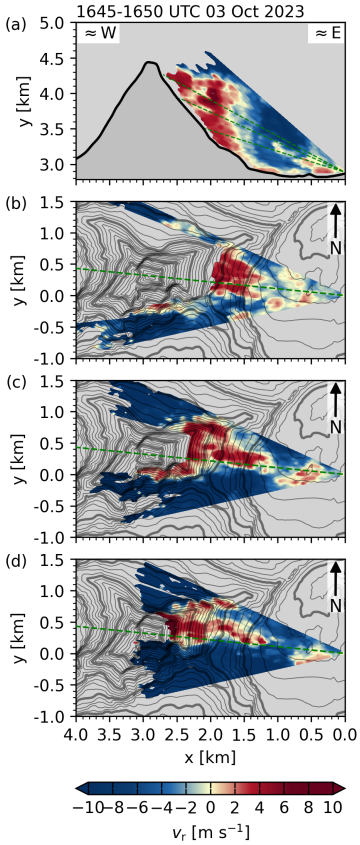

FIGURE 3.52: As Fig. 3.12, but for scan cycle between 1645 and 1650 UTC, 3 October 2023.

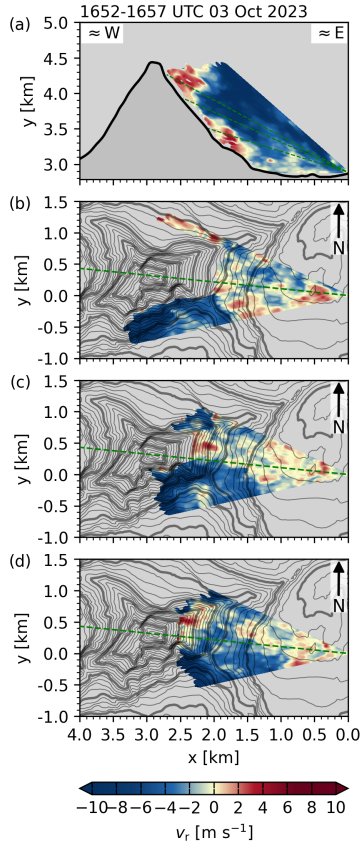

FIGURE 3.53: As Fig. 3.12, but for scan cycle between 1652 and 1657 UTC, 3 October 2023.

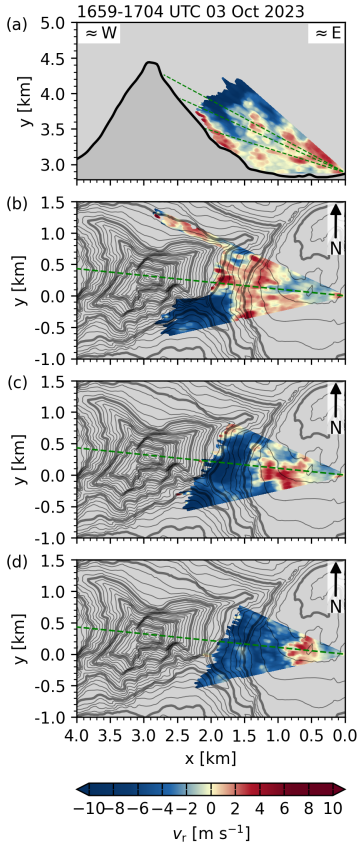

FIGURE 3.54: As Fig. 3.12, but for scan cycle between 1659 and 1704 UTC, 3 October 2023.

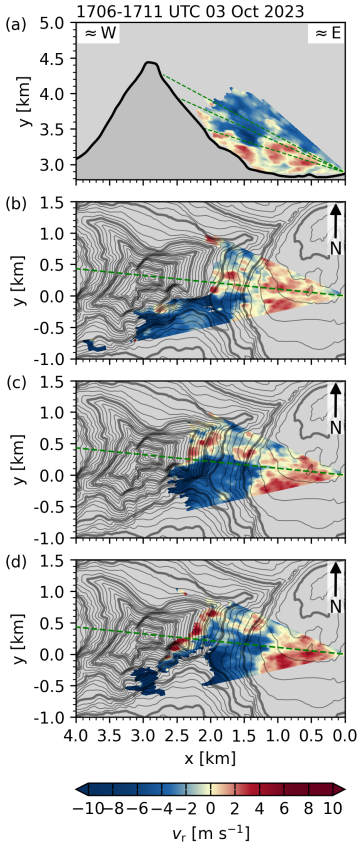

FIGURE 3.55: As Fig. 3.12, but for scan cycle between 1706 and 1711 UTC, 3 October 2023.

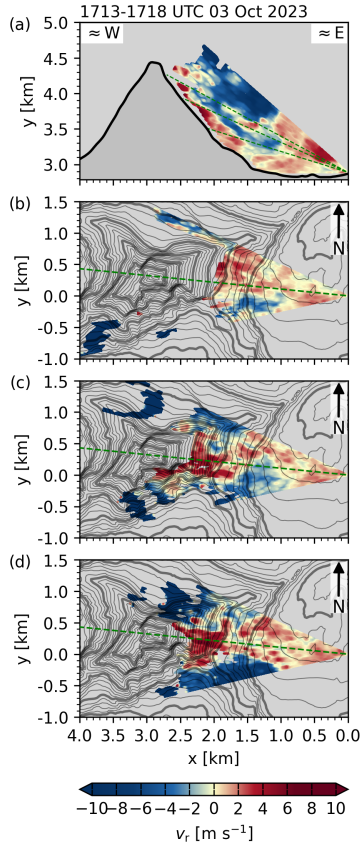

FIGURE 3.56: As Fig. 3.12, but for scan cycle between 1713 and 1718 UTC, 3 October 2023.

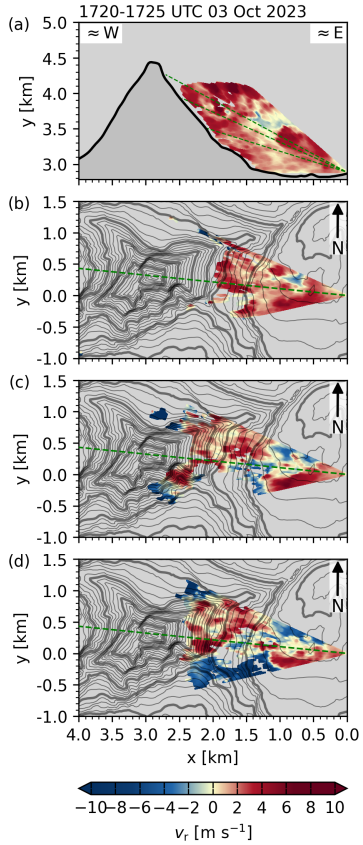

FIGURE 3.57: As Fig. 3.12, but for scan cycle between 1720 and 1725 UTC, 3 October 2023.

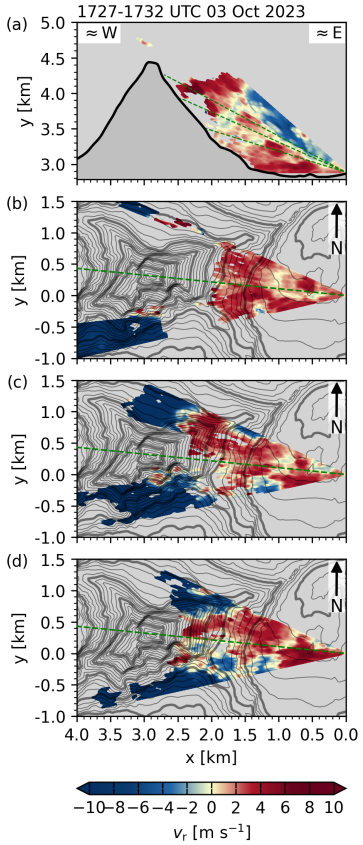

FIGURE 3.58: As Fig. 3.12, but for scan cycle between 1727 and 1732 UTC, 3 October 2023.

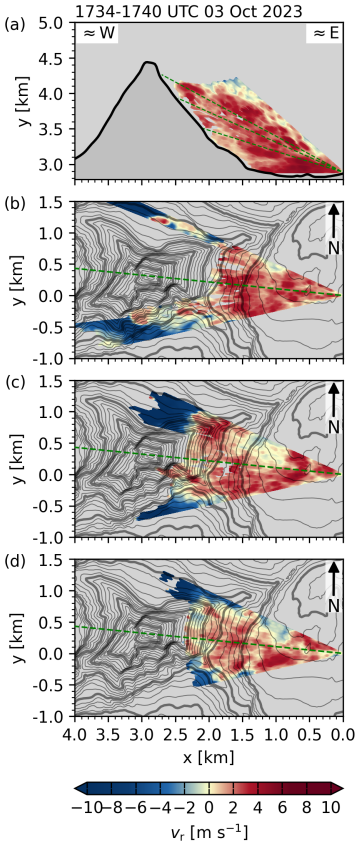

FIGURE 3.59: As Fig. 3.12, but for scan cycle between 1734 and 1740 UTC, 3 October 2023.

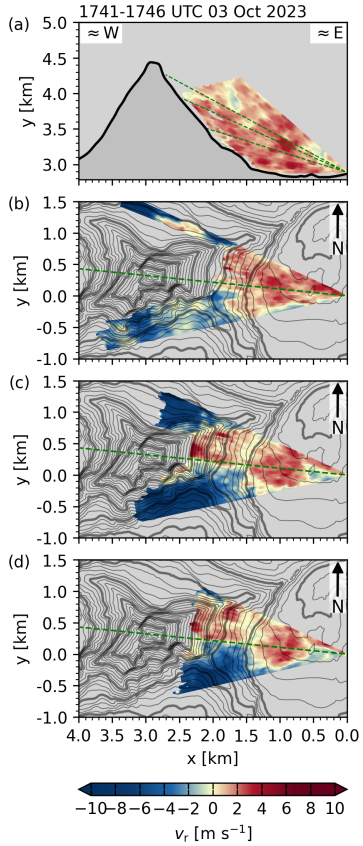

FIGURE 3.60: As Fig. 3.12, but for scan cycle between 1741 and 1746 UTC, 3 October 2023.

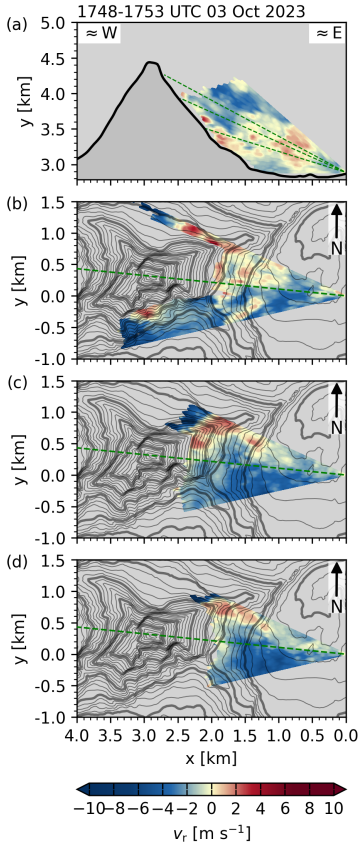

FIGURE 3.61: As Fig. 3.12, but for scan cycle between 1748 and 1753 UTC, 3 October 2023.

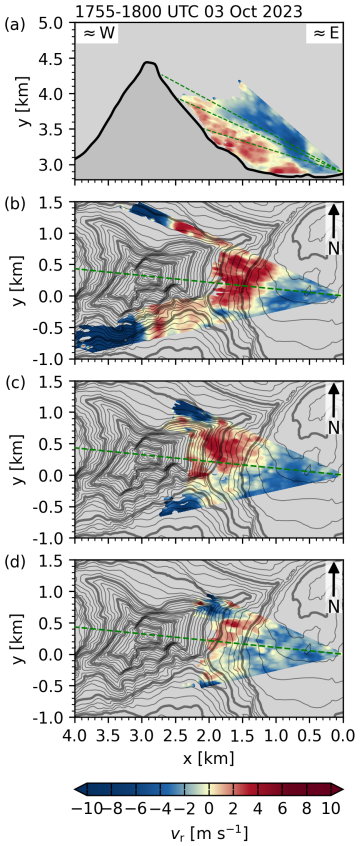

FIGURE 3.62: As Fig. 3.12, but for scan cycle between 1755 and 1800 UTC, 3 October 2023.

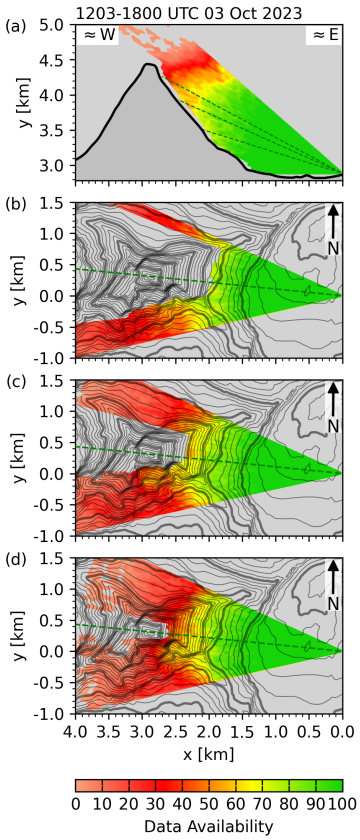

FIGURE 3.63: Percentage in data coverage available for composing the average radial velocities shown in Fig. 3.7, for (a) the range-height indicator scan (RHI) through the summit pyramid, and plan-position indicator scans (PPI) at (b) 16.5°, (c) 23°, and (d) 27° elevation for all cycles between 1200 and 1800 UTC, 3 October 2023.

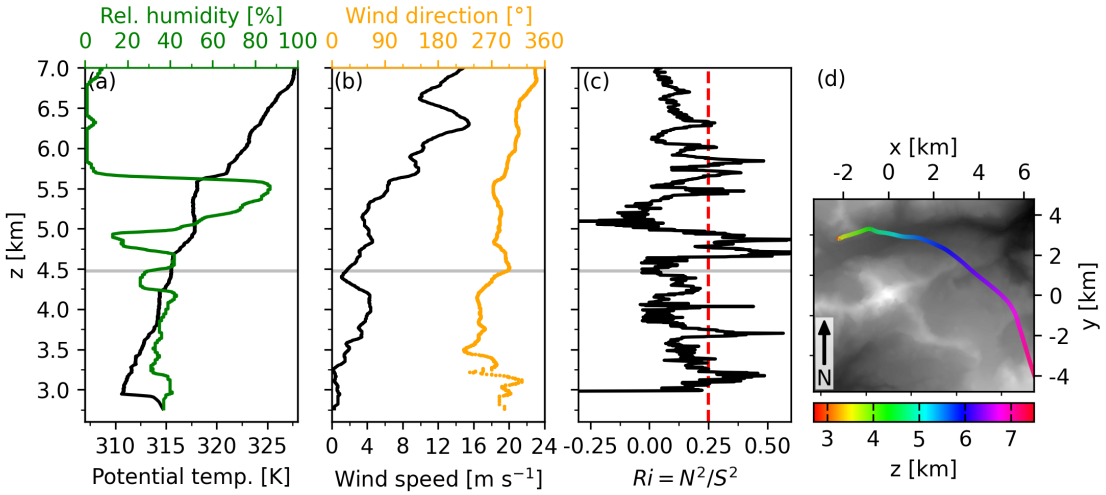

FIGURE 3.64: Upwind vertical profiles at 1050 UTC 28 September 2023 of (a) potential temperature and relative humidity, (b) wind speed and direction, and (c) gradient Richardson number, calculated using a 20-point rolling mean ($\approx$ 100 m). Horizontal gray lines indicate the summit height of the Matterhorn, and the red dashed line in (c) depicts the critical Richardson number Ri_c of 0.25. Panel (d) shows the ascent path of the radiosonde, with coordinates centered at the Matterhorn summit and grey shading indicating topography.

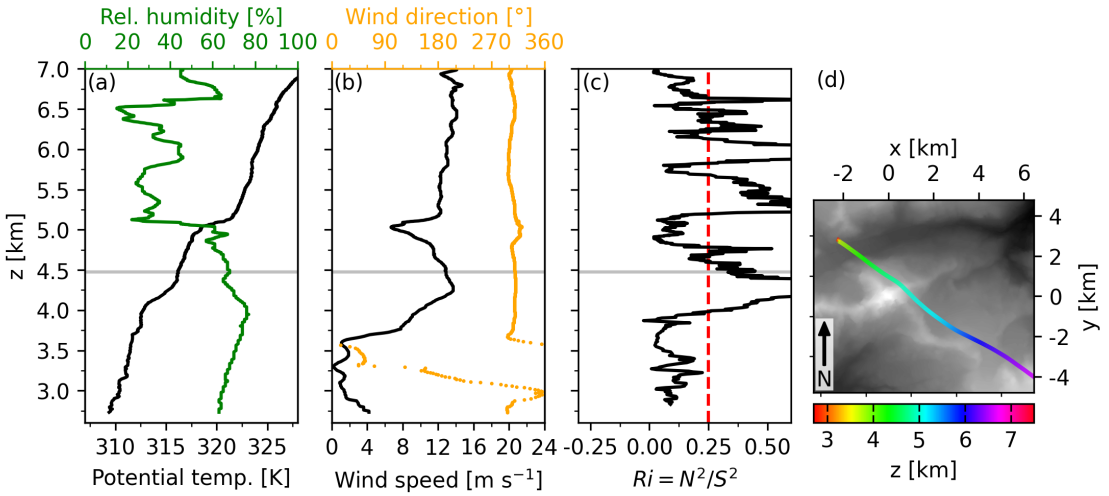

FIGURE 3.65: As Fig. 3.64, but for radiosonde data from 1740 UTC 29 September 2023.

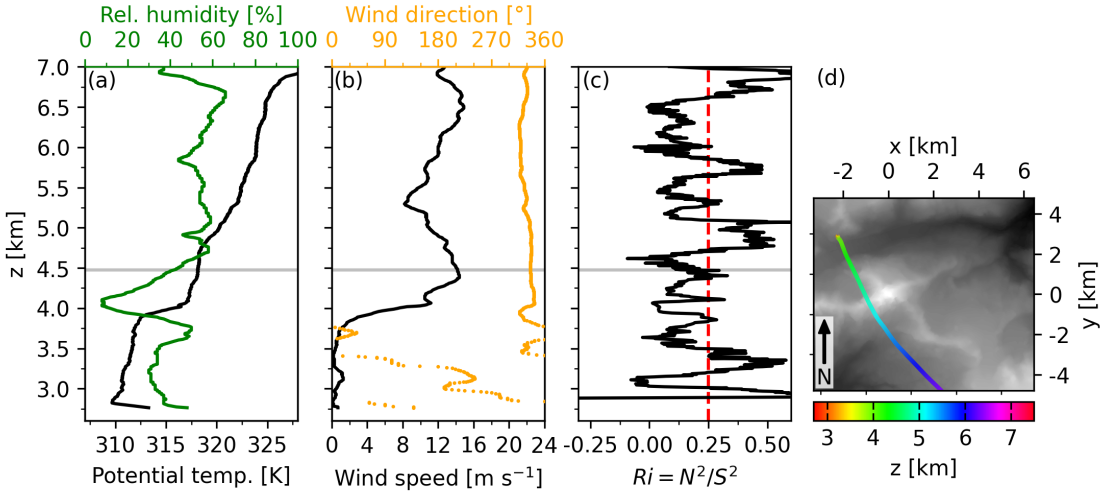

FIGURE 3.66: As Fig. 3.64, but for radiosonde data from 1200 UTC 30 September 2023.

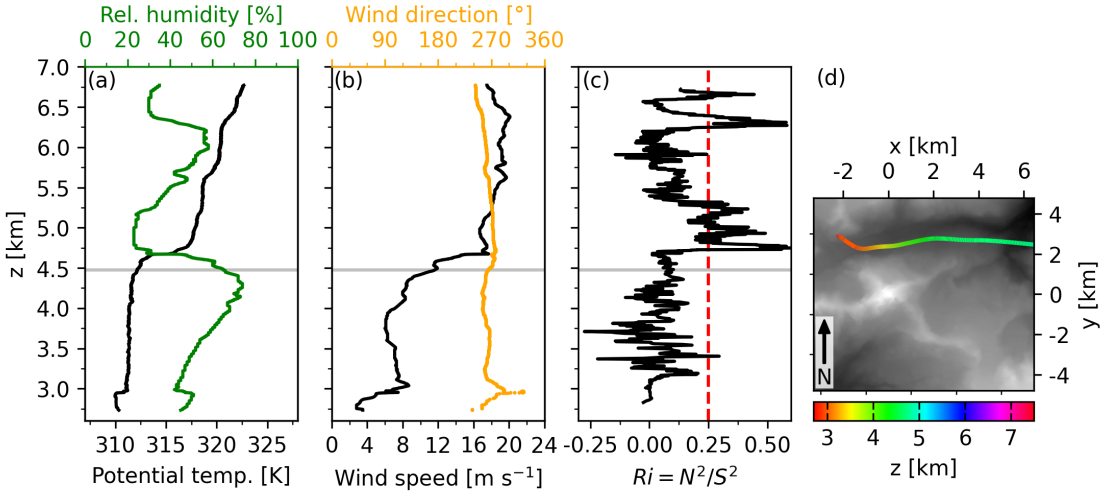

FIGURE 3.67: As Fig. 3.64, but for radiosonde data from 1200 UTC 3 October 2023.

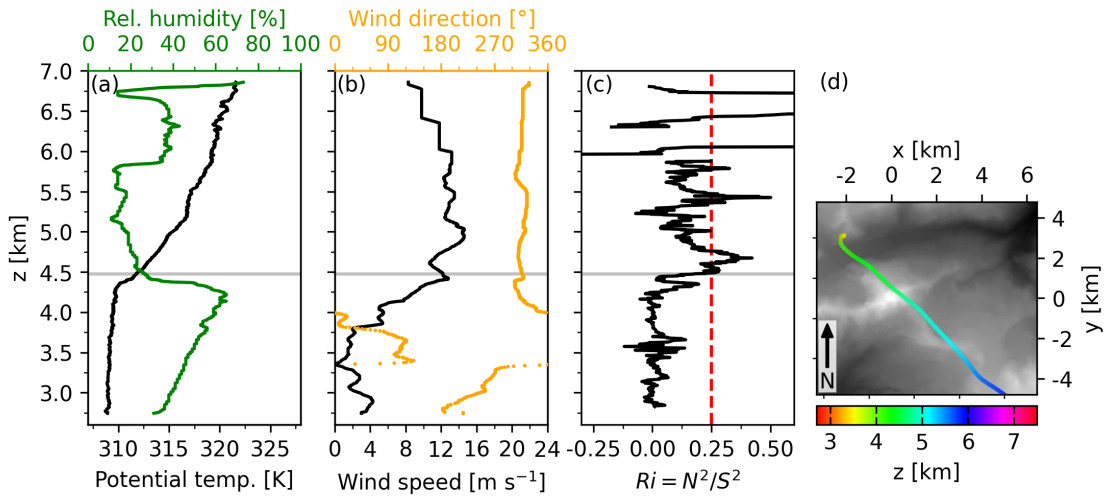

FIGURE 3.68: As Fig. 3.64, but for radiosonde data from 1220 UTC 9 October 2023.

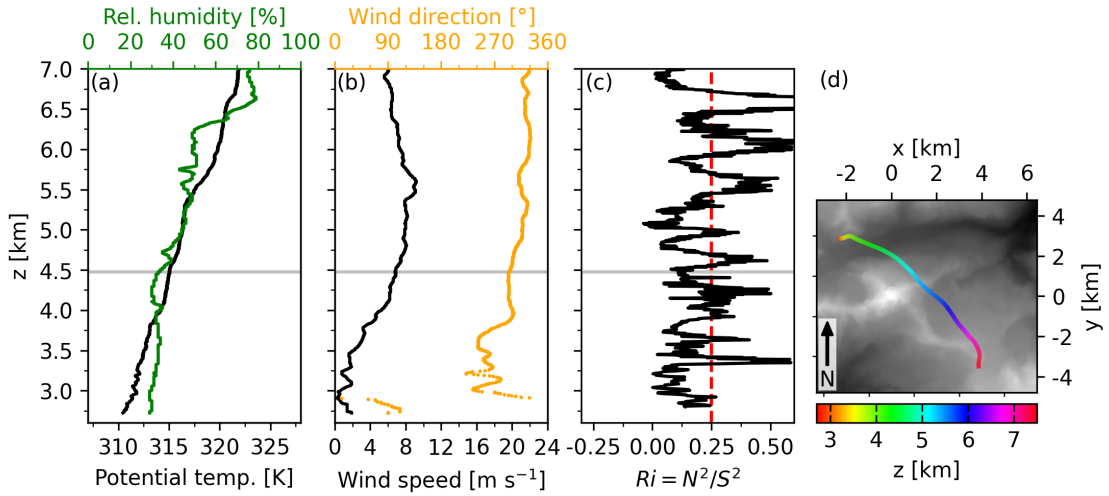

FIGURE 3.69: As Fig. 3.64, but for radiosonde data from 1600 UTC 10 October 2023.

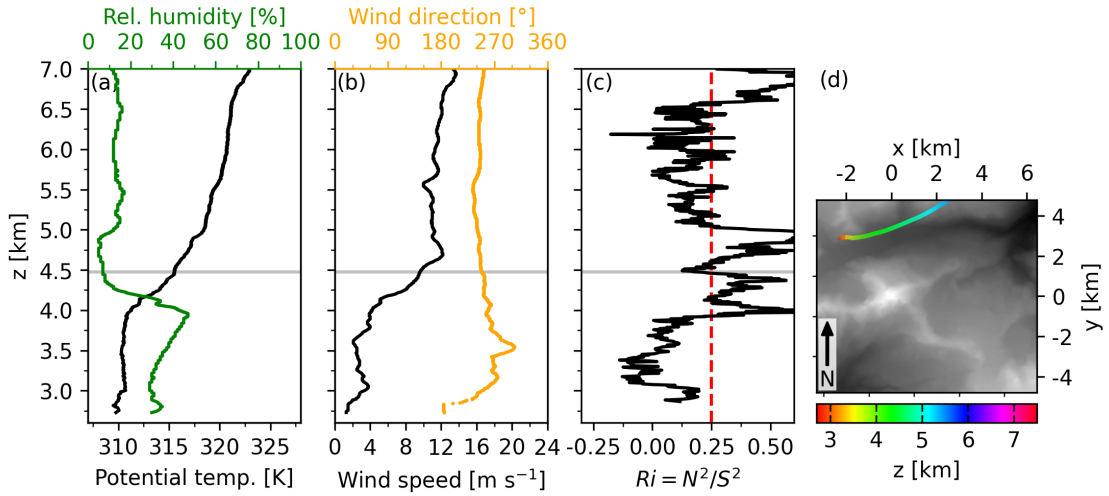

FIGURE 3.70: As Fig. 3.64, but for radiosonde data from 1320 UTC 11 October 2023.

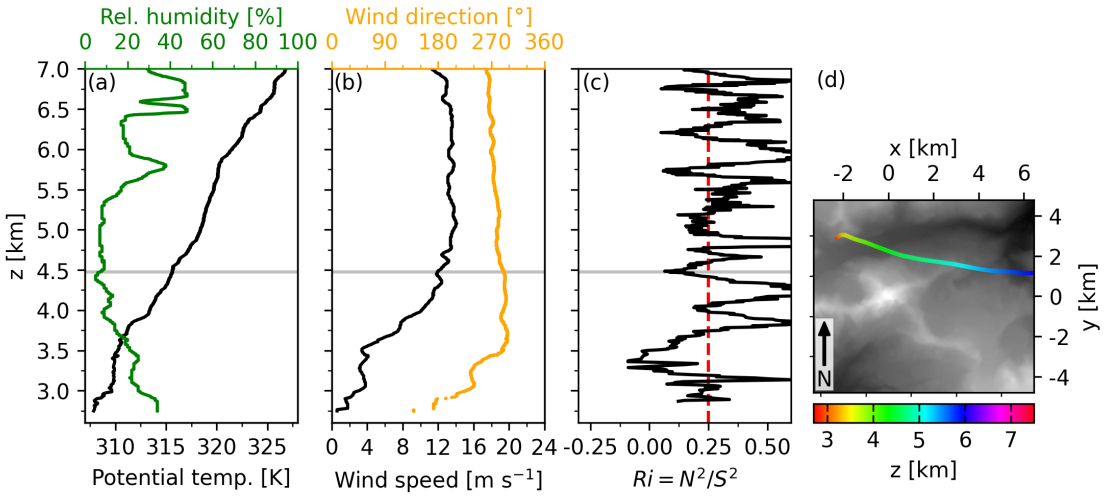

FIGURE 3.71: As Fig. 3.64, but for radiosonde data from 1630 UTC 12 October 2023.

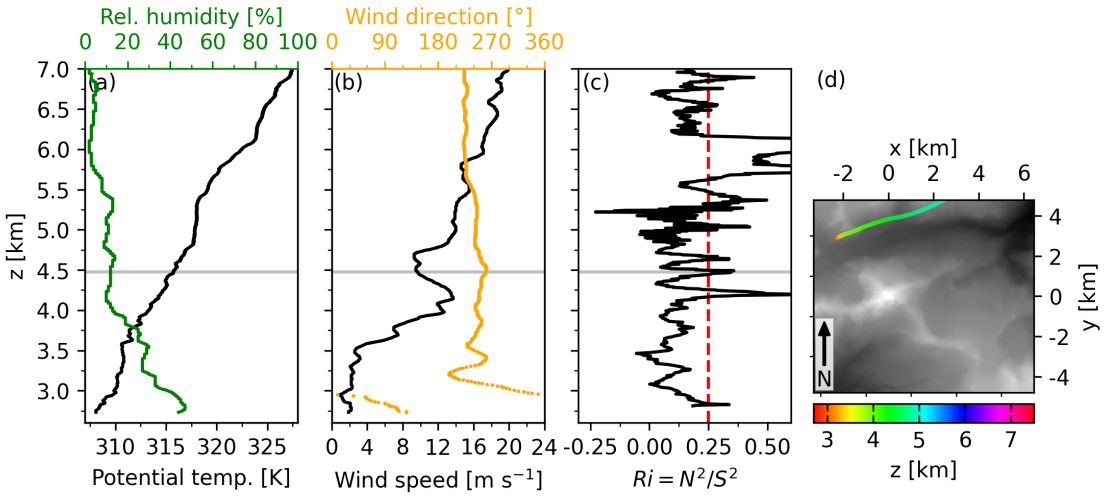

FIGURE 3.72: As Fig. 3.64, but for radiosonde data from 1530 UTC 13 October 2023.

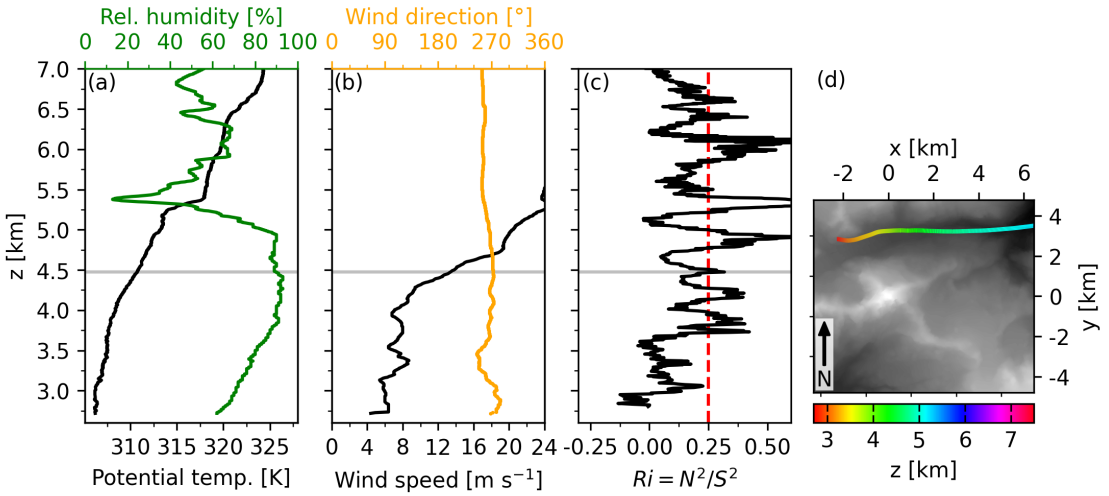

FIGURE 3.73: As Fig. 3.64, but for radiosonde data from 1210 UTC 14 October 2023.

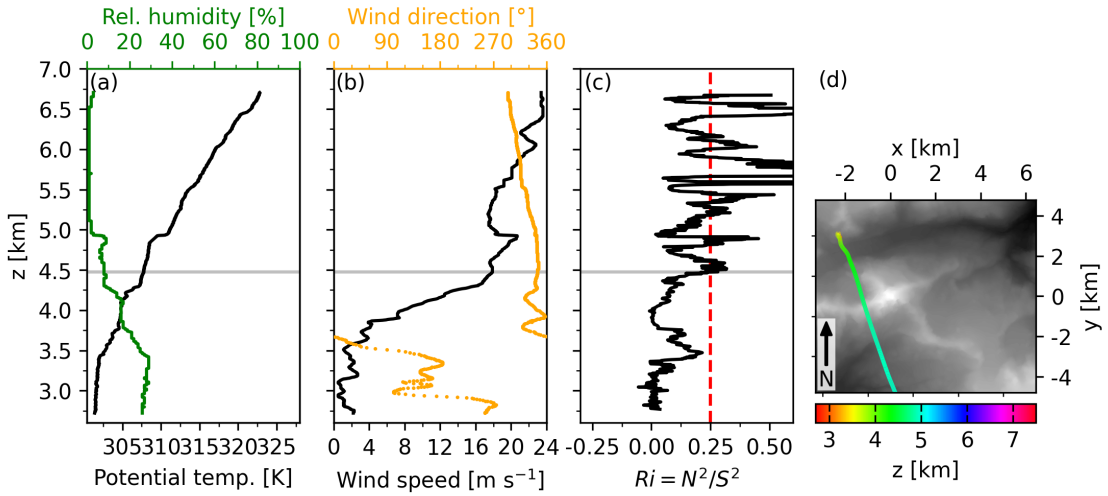

FIGURE 3.74: As Fig. 3.64, but for radiosonde data from 1540 UTC 15 October 2023.

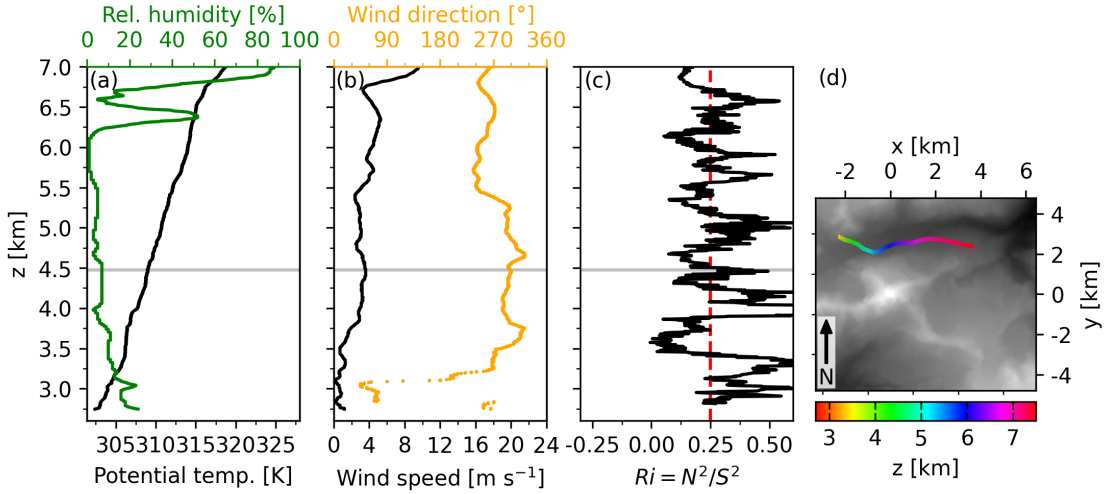

FIGURE 3.75: As Fig. 3.64, but for radiosonde data from 0910 UTC 16 October 2023.

4 Banner Cloud Formation at the Matterhorn: Measurements versus Large-Eddy Simulations

This chapter is taken from a manuscript which is currently under review:

Thomas, M. L., Hoch, S. W., Huwald, H., Lehning, M., van Schaik, B. J. A., Rentel, D. S., Imbert, P., and V. Wirth: Banner Cloud Formation at the Matterhorn: Measurements versus Large-Eddy Simulations. J. Atmos. Sci. [Under Review]

4.1 Abstract

Banner clouds are clouds in the lee of steep mountains or sharp ridges on otherwise cloud-free days. Previous studies identified key mechanisms and preferred flow conditions on the basis of idealized Large-Eddy Simulations, but it remained unclear to what extent these findings apply to real-world conditions. This state of affairs motivated a campaign at the Matterhorn in the Swiss Alps in fall 2023, during which observations were made using a scanning Doppler lidar and radiosondes. This paper analyzes the measurements from two episodes of banner cloud occurrence during the campaign and puts them into context using Large-Eddy Simulations. The observations confirm the previously hypothesized key mechanism of banner cloud formation, namely recirculating flow and strong upwelling on the leeward side of the mountain. The model simulations are configured such as to replicate the ambient flow conditions as observed by the radiosondes, allowing a comparison between the observed lidar scans and synthetic lidar scans produced from the model data. The comparison reveals a considerable level of agreement. Subsequently, the model simulations are used to contextualize the lidar measurements within the complex ambient flow conditions. The analysis confirms that the Lagrangian vertical displacement is a suitable dry diagnostic for banner cloud occurrence, and that distinct lee-side vortex structures are not a necessary prerequisite for banner cloud formation. It is concluded that banner clouds at the Matterhorn are a robust phenomenon occurring under a wide range of ambient flow conditions.

4.2 Introduction

Banner clouds are clouds that appear to be attached to the leeward side of steep mountains or sharp ridges on otherwise cloud-free days (Glickman, 2000). They resemble a banner flying in the wind, hence their name (Schween et al., 2007; Wirth et al., 2012). Banner clouds are noteworthy because flow past orography usually implies uplift and cloud formation on the windward side rather than

the leeward side. They occur only on steep mountains with a weakly stratified ambient atmosphere (Prestel & Wirth, 2016).

In the past, much has been learned about banner cloud formation through Large-Eddy Simulations, although most of these studies used highly idealized model configurations. In particular, orography was represented by a square pyramid (Reinert & Wirth, 2009; Voigt & Wirth, 2013; Schappert & Wirth, 2015; Wirth et al., 2020) or a rotationally symmetric cosine-shaped mountain (Prestel & Wirth, 2016). Similarly, inflow conditions were specified using simple inflow profiles (like a constant wind or constant wind shear) and idealized assumptions regarding the stratification. On the one hand, such idealized setups allowed one to identify key mechanisms and preferred flow conditions of banner cloud occurrence. On the other hand, it remained unclear to what extent the results apply to real-world conditions with complex orography and more realistic ambient atmospheric conditions.

More recently, Thomas & Wirth (2023) [chapter 2] numerically investigated flow past the highly complex orography of the Matterhorn (4478 m a.s.l.) in the Swiss Alps near the town of Zermatt. Their simulations confirmed the main mechanisms and preferred flow conditions that were previously derived in those more idealized model studies: (1) a coherent upwelling region terminates close to the summit on the leeward side of the mountain, (2) air parcels flow around the mountain before they are lifted into the banner cloud, and (3) a weakly stratified ambient atmosphere.

The latter study, too, was restricted to numerical simulations, and the question remains whether and to what extent they are representative for real banner clouds at the real Matterhorn. In an attempt to address this question, we conducted the observational MatterHorn EXperiment (MatterHEX) at the Matterhorn in fall 2023. We aimed to observe the complex flow features associated with banner cloud formation in such a way that they allowed systematic comparison with model simulations. The campaign, which made primarily use of Doppler lidar and radiosonde measurements, is described in detail in **Hoch et al. (2025)** [chapter 3].

The objectives of this paper are threefold: (1) to present the lidar measurements from two episodes with banner cloud occurrence, (2) to present Large-Eddy Simulations which are representative for the conditions during the two episodes, and (3) to compare the lidar observations with synthetic lidar scans retrieved from the model simulations. As it turns out, both demonstrate a considerable level of consistency in capturing the key lee-side flow features. We are, thus, encouraged to use the Large-Eddy Simulations in order to fill observational gaps and contextualize the lidar observations within the broader ambient flow conditions. Finally, this allows us to confirm the utility of the Lagrangian vertical displacement as a diagnostic for banner clouds occurrence.

The paper is organized as follows. First, in section 4.3, we describe our observational strategy including the instrumentation, and the meteorological conditions during the two episodes. In addition, we explain our lidar scanning strategy and the filtering procedure used to process the raw data. In sections 4.4 and 4.5 we present the setup of our numerical model, explain how we configured the model to match the observed conditions, and introduce the diagnostic tools used for model data analysis. The lidar retrievals and their comparison with model-simulated synthetic lidar scans will be shown in section 4.6. We then present the simulated three-dimensional flow patterns in the lee of the mountain and relate them to banner cloud occurrence. Finally, section 4.7 provides a summary and our principal conclusions.

4.3 The MatterHEX Field Campaign

The MatterHEX field campaign took place from 29 September to 16 October 2023, with the objective to collect observational data on key lee-side flow features conducive to banner cloud formation.

This dataset was intended to enable a systematic comparison with model simulations. The following subsections describe the observational strategy and the instrumentation, highlight the distinct characteristics of the specific banner cloud episodes selected for analysis, and explain the lidar scanning strategy and associated post-processing techniques. For a complete overview of the campaign strategy, the deployed instruments, and the observational timeline, we refer to **Hoch et al. (2025)** [chapter 3].

4.3.1 Observation Strategy and Instrumentation

Figure 4.1 provides an overview of the investigation area and the location of the deployed instruments. The observational data used in this study stem from radiosondes, a scanning Doppler lidar, a sonic anemometer, and a webcam (Tab. 4.1). Radiosondes were used to measure ambient flow conditions during banner cloud formation at the Matterhorn. These measurements were crucial for specifying the initial and boundary conditions of the numerical simulations described in section 4.4. The Schönbielhütte SAC (Swiss Alpine Club) at 2694 m a.s.l., approximately 3.7 km northwest of the Matterhorn (Fig. 4.1a), was selected as the best launch site given the anticipated westerly to north-westerly flow during the fall season in this region. In the following all heights are given as height above mean sea level.

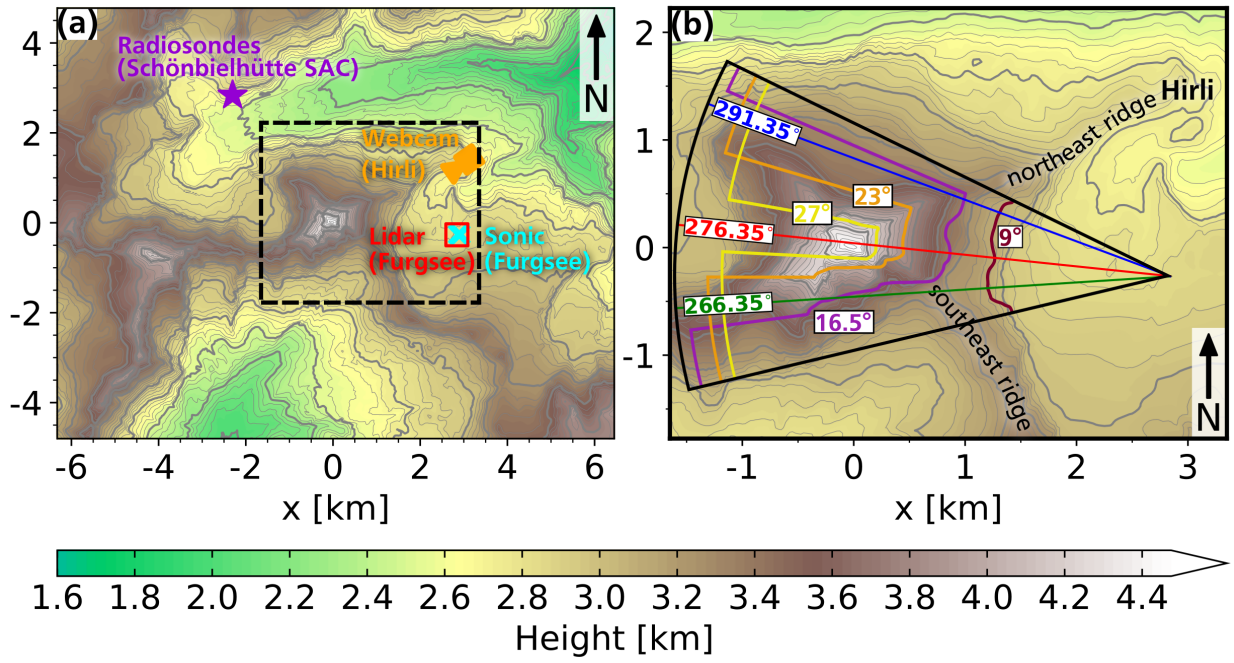

FIGURE 4.1: Topography of (a) the target region and its surroundings with the distribution of instruments. The dashed black rectangle indicates (b) the detailed zoomed-in view of the terrain on the leeward side of the Matterhorn including the RHI ($\alpha = 266.35, 276.35$, and $291.35°$) and PPI ($\theta = 9.0, 16.5, 23.0$, and $27.0°$) lidar scan paths and their intersections with the terrain. The coordinates are centered at the Matterhorn summit.

A Halo Photonics Streamline XR Doppler lidar, positioned approximately 2.9 km east of the Matterhorn near Furggsee at 2877 m (Fig. 4.1a), measured radial wind velocities v_r along the line of sight (LOS) of the lidar beam. The lidar scans were defined by varying the azimuthal angle α and the elevation angle θ of the laser beam. We combined range height indicator (RHI) scans and plan position indicator (PPI) scans to investigate the flow field around the summit pyramid of the Matterhorn (Fig. 4.1b). Radial wind speeds were retrieved for distance segments (range gates) with a length of 60 m (range gate length) along the LOS path of the laser beam based on the Doppler

shift of the laser beam scattered back to the lidar by aerosols. Generally, the range gate length can be adjusted based on the required spatial resolution and based on the aerosol loading. As aerosols are typically scarce in high-altitude regions, we chose a combination of a 60 m range gate length and corresponding scan speeds to resolve flow variations on a spatial scale of approximately 50 m.

The formation of banner clouds and their temporal and spatial evolution were documented using webcams. This study focuses on webcam images and time-lapse sequences obtained from the webcam deployed at the upper Hirli cable car station (see supplementary material), approximately 3.4 km northeast of the Matterhorn (Fig. 4.1a).

TABLE 4.1: Instrumentation used for analysis.

Instruments	Sites	Latitude	Longitude	Height
Doppler lidar	Furggsee	45.97395°	7.69527°	2877.0 m
Sonic Anemometer	Furggsee	45.97422°	7.69568°	2884.0 m
Webcam	Hirli	45.989°	7.699°	2774.0 m
Radiosonde	Schönbielhütte SAC	46.002°	7.629°	2694.0 m

4.3.2 Weather Conditions During the Two Episodes

During the 17-day observation period, banner clouds were observed on eight days with different levels of visibility. For this study, we focus on data collected during two specific banner cloud episodes, 29 September and 3 October 2023. These days were chosen because well-defined banner clouds occurred under distinctly different stratification and ambient wind conditions.

During the first episode on 29 September, the prevailing ambient flow was from the northwest. Aerosols were scarce, leading to weak clear-air lidar returns. The cloud geometry regularly alternated between two phases: one resembling a banner cloud, clearly limited to the southeast side of the Matterhorn, and another one where clouds covered the northwestern side of the mountain, too. By late afternoon, the banner cloud had developed a compact shape. The webcam image on the left of Fig. 4.2, captured at 1657 UTC (1857 CEST), clearly shows the banner cloud, demarcated from the nearly cloud-free windward side. The radiosonde observation at 1736 UTC (1936 CEST) (shown later in Fig. 4.6a-c) indicates a northwesterly ambient flow with changes in wind shear, particularly between 4 and 5.5 km. The wind speed increased up to approximately 4.2 km. The potential temperature profile indicates weak stratification, interrupted by two layers of enhanced stability below and above the Matterhorn summit. A decrease of wind speed was observed between the layers of increased stability.

On 3 October, available aerosols allowed for enhanced clear-air lidar returns. The ambient wind was predominantly blowing from the west, and banner clouds of varying shapes could be observed. The webcam image on the right of Fig. 4.2, captured at 1409 UTC (1609 CEST), shows a banner cloud extending far downstream to the east. The radiosonde ascent from 1358 UTC (1558 CEST) (shown later in Fig. 4.6e-g) indicates a near-neutral stratification extending just above the summit of the mountain, capped by a strong 5 K temperature inversion. A strong increase in wind speed from 8 to 17 m s^{-1} was observed at the altitude of the Matterhorn summit. The passage of a cold front around 1700 UTC (1900 CEST) interrupted the banner cloud occurrence temporarily.

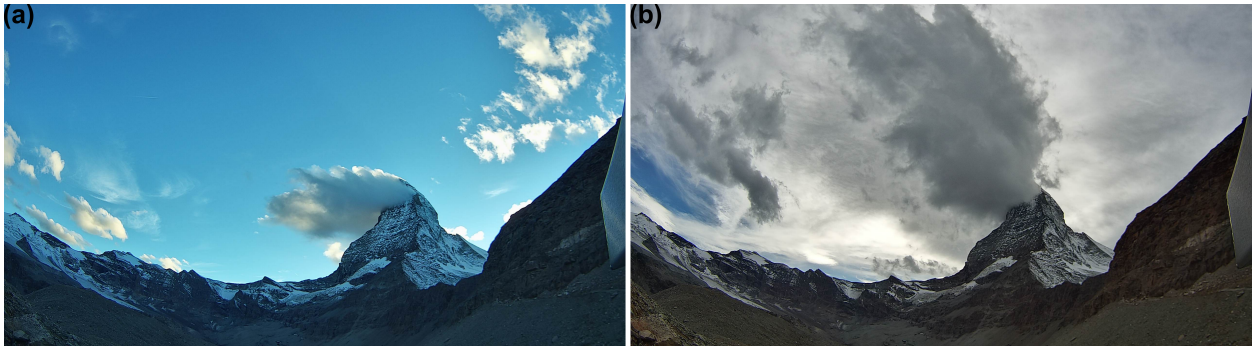

FIGURE 4.2: Banner clouds observed at the Matterhorn (a) at 1657 UTC (1857 CEST) 29 September and (b) at 1409 UTC (1609 CEST) 3 October. Both photo images are taken from the webcam installed near Hirli northeast of the Matterhorn (Fig. 4.1). Time-lapse sequences are available in the supplementary material.

4.3.3 The Lidar Scanning Strategy

Our scanning strategy was designed to observe leeward recirculation patterns and upwelling close to the mountain slopes; it involved a series of three RHI and four PPI scans that was repeated approximately every seven minutes. The lidar was operated in the continuous scanning mode, meaning that LOS data is accumulated over the angular range covered in the beam's acquisition interval. The three RHI scans were aligned either centered with the mountain summit ($\alpha = 276.35°$), to its south ($\alpha = 266.35°$), or north ($\alpha = 291.35°$), covering a range of elevation angles θ between 0 and 40° (Fig. 4.1b). The RHI scans north and south of the Matterhorn were selected in order to observe the North-South asymmetry of the flow around the summit. The angular resolution of the scans was $\Delta\theta \approx 0.55°$, resulting from the selected scanning speed and acquisition time. This amounts to a vertical resolution of approximately 35 m at the distance of the summit pyramid. The four PPI scans covered an azimuthal range between $\alpha = 256.6$ and 297.1° at fixed elevation angles $\theta = 9.0, 16.5, 23.0$, and 27.0° (Fig. 4.1b). For reference, the summit of the Matterhorn appears at an elevation angle of $\theta \approx 30°$ and an azimuthal angle of $\alpha \approx 276.4$ when seen from the lidar location. The azimuthal resolution of the PPI scans was $\Delta\alpha \approx 0.56°$, which corresponds to approximately 35 m at the distance of the summit pyramid.

4.3.4 Filtering of the Lidar Data

The quality of retrieved v_r values from the lidar strongly depends on the atmospheric conditions (aerosol availability) and the experimental setup. Retrievals with a low signal-to-noise ratio, SNR [dB], given by the base 10 logarithm of the signal power to noise power ratio, are commonly removed using a threshold filter (Hill et al., 2010; Krishnamurthy et al., 2013; Newsom et al., 2015; Gryning et al., 2016). However, choosing an appropriate SNR threshold is case-specific and might reject good data from regions far away from the lidar position, since SNR values decrease rapidly with distance (Alcayaga, 2020). To address this issue, excessive data filtering using conventional SNR thresholds was compensated by combining it with the Density-Based Spatial Clustering of Applications with Noise (DBSCAN) algorithm (Ester et al., 1996). DBSCAN detects high density clusters in (v_r,SNR)-space, enabling it to distinguish reliable v_r values from noise within the same SNR range. This method recovers reliable v_r values otherwise removed by the fixed SNR-threshold filter. The effectiveness of DBSCAN for v_r filtering lidar scanning patterns has previously been shown by Alcayaga (2020) and Duscha et al. (2023).

More specifically, the DBSCAN algorithm identifies clusters of measurement points whose neighborhood in (v_r,SNR)-space of size ε contains a minimum number of points, N_{min} (Ester et al.,

1996). These clusters grow until all reachable points have been added and all clusters are separated as individual groups. The choice of both input parameters has a strong impact on the resulting clusters. On the one hand, large ε in combination with small N_{min} would result in sparse clusters, which are likely to contain noise. On the other hand, small ε in combination with large N_{min} would lead to incompletely delimited clusters, because not all nearby points would be reached.

Before applying the DBSCAN algorithm, we removed all $|v_{\text{r}}| > 20\,\text{m s}^{-1}$ because these are considered to be unrealistic for both episodes. Moreover, we determined the DBSCAN parameters ε and N_{min} through visual inspections of the (v_{r},SNR) scatter diagrams for both the RHI and the PPI scan configurations individually. In the end we decided to use $\varepsilon = 0.9$ and $N_{\text{min}} = 150$ for RHI, and $\varepsilon = 0.9$ and $N_{\text{min}} = 100$ for PPI scans. The left panel of Fig. 4.3 exemplifies the application of the DBSCAN algorithm at 1507 UTC (1707 CEST) on 3 October 2023. Apparently, the algorithm identifies a cluster of points, with only a small fraction of points located outside of the densest region (red). By definition, all points lying outside the cluster (gray) are considered noise. However, the DBSCAN algorithm might exclude other reliable points that cannot be assigned to the cluster. For instance, the points outlined in green are assigned to measured values within a cloud (not shown). To retain these points, we decided to combine the DBSCAN and SNR-threshold filters using a logical OR for each time step (step 1 in Fig. 4.3). Through visual inspection, we found that some erroneous features were retained. To address this issue, we furthermore discarded points along each LOS that are surrounded by two invalid points (i.e., points already filtered out) in each direction, i.e., at two previous, two following, and two neighboring range gates.

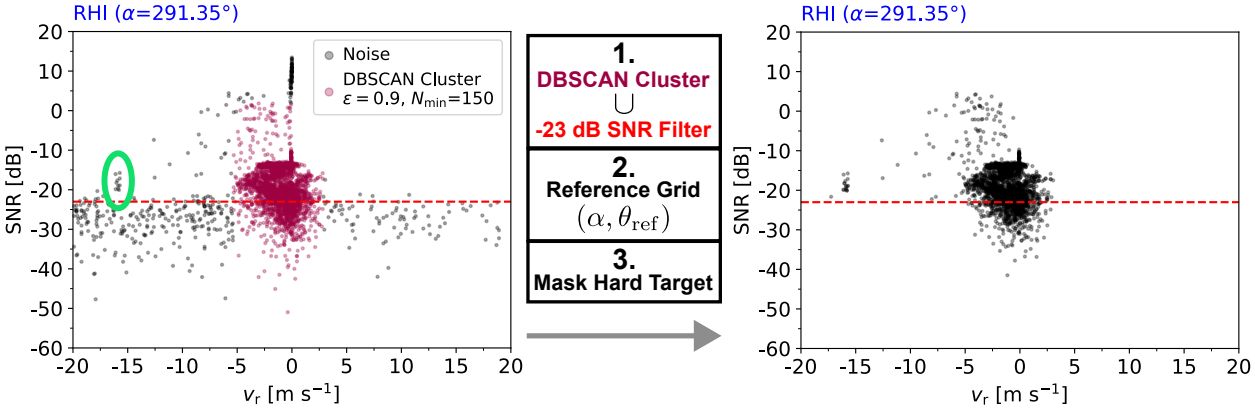

FIGURE 4.3: Example of the filtering procedure along the RHI lidar scan with $\alpha = 291.35°$ at 1507 UTC (1707 CEST) 3 October 2023. The left panel shows the result of the DBSCAN algorithm with the parameters $\varepsilon = 0.9$ and $N_{\text{min}} = 150$ applied to all raw (v_{r},SNR) values with $|v_{\text{r}}| \leq 20\,\text{m s}^{-1}$. Values assigned to the DBSCAN cluster are colored in red. By definition, all other values are classified to be noise (gray). Values attributed to a cloud are circled in green. The red dashed line marks the fixed SNR-threshold of $-23\,\text{dB}$, below which all values are filtered out. The right panel shows the final set of (v_{r},SNR) values after the following three steps: 1. The union of values of the DBSCAN cluster and SNR $\geq -23\,\text{dB}$, 2. Interpolation on reference lidar grid, and 3. Additionally discarding all hard target returns.

Since small angle variations occur in the repeated scans we interpolated the values to a reference lidar grid. For this purpose, we defined a reference elevation and azimuthal angle range, $\theta_{\text{ref}} := [\theta_1, \theta_2, \ldots, \theta_n]$ and $\alpha_{\text{ref}} := [\alpha_1, \alpha_2, \ldots, \alpha_n]$. They are based on the mean angular resolution, $\overline{\Delta\theta} \approx 0.55°$ and $\overline{\Delta\alpha} \approx 0.56°$, as well as the minimum and maximum of θ and α from our reference date, 2 October. The v_{r} values were then interpolated to the new $(\alpha, \theta_{\text{ref}})$ and $(\alpha_{\text{ref}}, \theta)$ positions (step 2 in Fig. 4.3).

Lidar returns from the mountain slopes are called hard target returns. They can easily be identified as having high backscatter concomitant with zero v_{r}. We removed the hard target returns as a third step in the filtering process (step 3 in Fig. 4.3). For this purpose, we used the hard-target

returns from 2 October, when weather conditions were very dry and aerosols were scarce, allowing us to develop our "hard-target filter". The final result of our combination of filtering procedures on 3 October is shown in the right column of Fig. 4.3.

The aerosol loading varied between the two episodes. On 29 September, low aerosol content reduced the SNR obtained by the lidar, and the v_r filtering procedure primarily retained v_r values close to the lidar and in clouds at greater distances. In contrast, on 3 October, sufficient aerosols ensured a high density of reliable lidar returns even at larger distances. A detailed comparison of data availability for the RHI and PPI scans on 29 September and 3 October is provided in Fig. 4.15 and Fig. 4.16 of the supplementary material.

4.3.5 Time Averaging

After applying the data quality control filters, the lidar scans are available for analysis approximately every seven minutes. As an example, Figs. 4.4a-f shows every second RHI scan between 1355 UTC (1555 CEST) and 1512 UTC (1712 CEST) on 3 October 2023. In each RHI scan, we can clearly distinguish regions with motion away from the lidar (red) from regions with motion towards the lidar (blue). Comparing these scans with the time-wise closest webcam images in Figs. 4.4h-m reveals that the lidar return signals are not limited by aerosol availability, but only by the attenuation occurring within the banner cloud.

The spatial variations within the individual RHI scans, along with the temporal variations in the series of RHI scans and the webcam images, highlight the turbulent nature of the flow around the steep and complex terrain of the Matterhorn. Consequently, comparing individual lidar scans with synthetic lidar scans from our simulations would be inappropriate, because each of these describe a different realization of the turbulence. Therefore, we only consider time-averaged lidar retrievals for further analysis. As consecutive scans are only available every seven minutes, we have to assume statistical stationarity of the flow during the defined averaging period. Similarly, we assume stationarity of the upstream conditions. The time averages of v_r were calculated at each point on the lidar reference grid. Data availability varies across the grid points. To ensure the reliability of our final time-composite lidar retrievals, we set a minimum data availability threshold of 25 % for each grid point. For an averaging period of one hour, this corresponds to data availability in at least three out of twelve scans. Figure 4.4g illustrates an example from the time period between 1355 UTC (1555 CEST) to 1512 UTC (1712 CEST) on 3 October.

4.4 Numerical Model and Model Configuration

For our simulations, we consider three-dimensional turbulent flow of dry air in a non-rotating atmosphere using the compressible version of the EULAG model in LES mode (Prusa et al., 2008; Smolarkiewicz et al., 2014; Kurowski et al., 2014; Smolarkiewicz et al., 2016). Our general model configuration closely follows that of Thomas & Wirth (2023) [chapter 2], who demonstrated that this model is able to deal with the steep and complex orography of the Matterhorn region. We use a Cartesian grid and represent the orography through an immersed boundary method (Mittal & Iaccarino, 2005; Smolarkiewicz et al., 2007). This approach effectively represents a no-slip boundary condition (Goldstein et al., 1993; Smolarkiewicz et al., 2007), but lacks explicit control over surface friction. However, this limitation is no disadvantage for the investigation of banner clouds, as strong surface friction is required for their formation (Prestel & Wirth, 2016). Subgrid-scale turbulent transport is implemented by a TKE prognostic equation closure based on Schumann's parameterization (Schumann, 1991). Radiation effects and surface heat fluxes are assumed to be zero. Furthermore, we do not incorporate cloud microphysics in this study, as our primary focus is

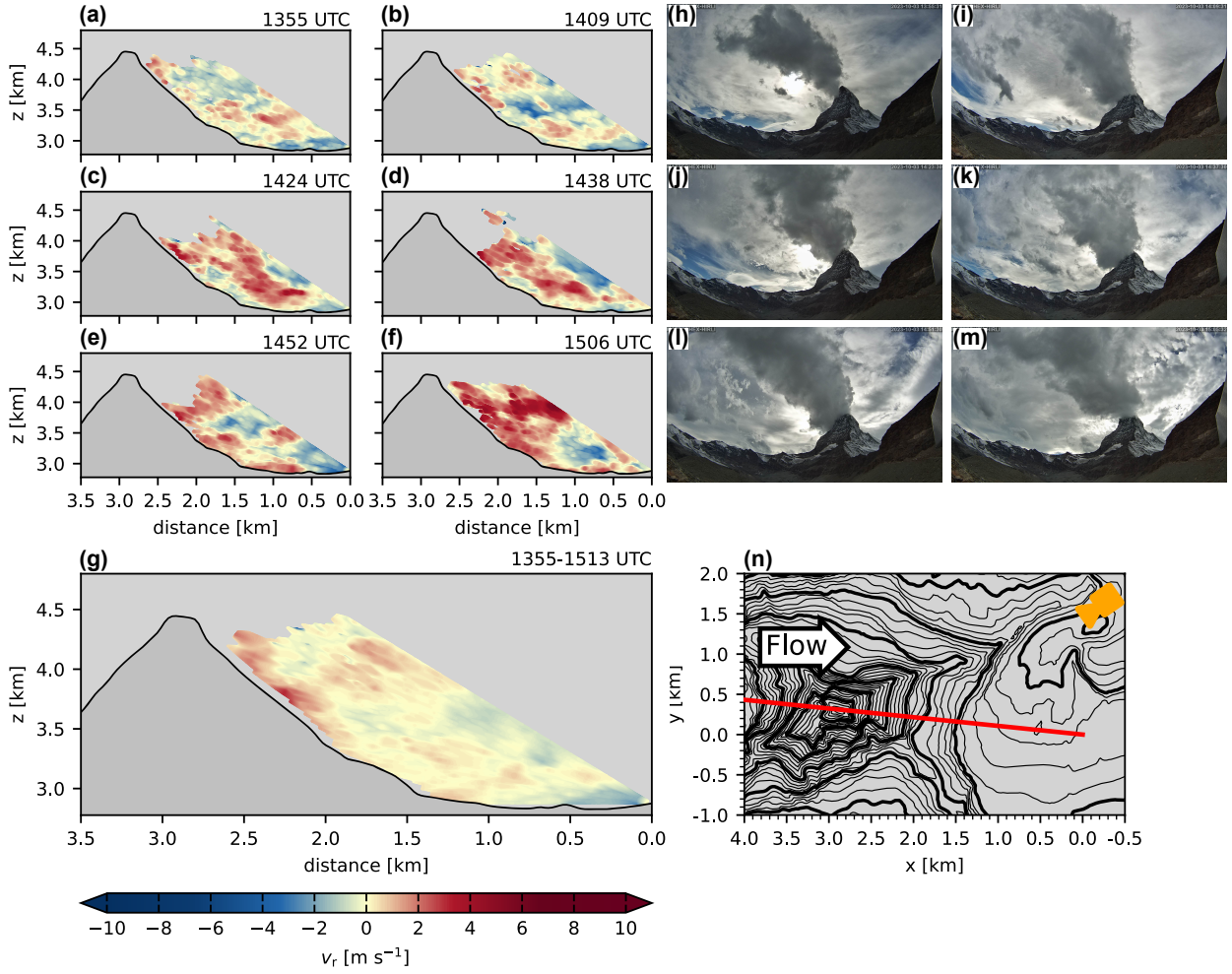

FIGURE 4.4: RHI lidar scan with $\alpha = 276.35°$ between 1355 UTC (1555 CEST) and 1512 UTC (1712 CEST) 3 October 2023 and comparison with webcam images. Panels (a)-(f) show six (out of twelve) RHI scan retrievals; the latter were used to compute a time-averaged composite (panel g) by accounting for all grid points, for which data were available during at least three out of twelve scans (25 %). Red colors indicate motion away from the lidar and blue colors motion towards the lidar. Black lines in the RHI panels represent terrain height. Panels (h) to (m) show the time-wise closest webcam images from the Hirli site on the northeast ridge of the Matterhorn. Panel (n) shows the orientation of the RHI scan, the position of the webcam, and the ambient flow direction indicated by the large arrow.

on the underlying mechanisms required for banner cloud formation, assuming sufficient moisture availability. The approach used to estimate the occurrence of clouds in the absence of moisture and explicit cloud modeling is detailed in section 4.5.2.

We consider real orography based on two datasets: the Cartesian topographic dataset DHM25 from the Swiss Federal Office of Topography (swisstopo) at a resolution of 25 m in the LV03 projection (swisstopo, 2017), and the topographic dataset TINITALY version 1.1 at a resolution of 10 m in the UTM WGS 84 Zone 32 projection system (Tarquini et al., 2023). We converted the TINITALY data to the LV03 projection and interpolated them to a grid with a resolution of 25 m. In regions where both datasets overlap, a distance-weighted composite is created using both datasets. Note that the Furgg Glacier has retreated since the DHM25 data set has been generated. As a consequence, some of our plots show observed data slightly below the model orography.

Our model configuration implies that only one of the four domain boundaries can serve as an inflow boundary. It follows that the simulation of strictly westerly flow on 3 October is straightforward, using the left boundary as inflow boundary (Fig. 4.5b). For other, more general ambient

flow directions, we rotated the topography within the model domain such that we could always use the left boundary as inflow boundary (Fig. 4.5a). In addition, for the purely westerly ambient flow on 3 October, we slightly smoothed the orography at the northern boundary to avoid numerical instabilities. For both setups, the model domain extends 12.8 km $\times$ 9.6 km $\times$ 7 km in the x-, y-, and z-direction, respectively, where the x-coordinate corresponds to the streamwise direction. The grid spacing is equidistant with $\delta x = \delta y = \delta z = 25$ meters.

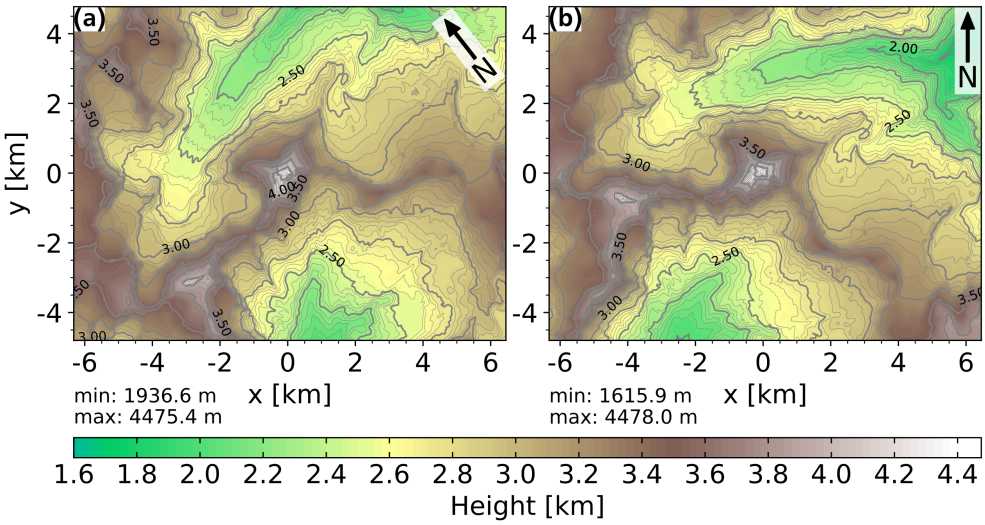

FIGURE 4.5: Model orography for (a) the September Case with inflow wind direction of 308° and (b) the October Case with inflow wind direction of 270°.

We apply a rigid-lid condition at the upper domain boundary and open conditions at the streamwise and lateral boundaries. Absorbers are used at all model domain boundaries to relax flow velocity and potential temperature toward the ambient state, and minimizing wave reflections. Over the uppermost 2 km of the model domain, relaxation is applied with a time scale of $\tau = 250$ s. At the streamwise and lateral boundaries, relaxation is applied over the outer 1000 m and 1500 m of the domain with a time scale of $\tau = 1000$ s.

The simulations use a dynamic integration time-step Δt constrained by the CFL stability criterion. The model runs are split into two parts: a spin-up period of duration t_{su}, and an analysis period of duration t_{an}. The spin-up period was made just long enough to achieve a statistically stationary state. For our analysis, we consider the time-averaged fields during t_{an}. The duration of the spin-up period and the total simulation time $t_{\mathrm{sim}} = t_{\mathrm{su}} + t_{\mathrm{an}}$ are given in Tab. 4.2.

The initial and boundary conditions are based on our radiosonde observations, which provide vertical profiles of wind speed, wind direction, and potential temperature. We assume that these measurements are representative for the ambient flow conditions. They are depicted with blue color in Fig. 4.6a-c and Fig. 4.6e-g. In addition, the radiosonde profiles are used to compute a hydrostatically balanced ambient state that is required by EULAG.

The challenge was to design the initial and boundary conditions such that the resulting model state can be taken as representative for the conditions during either of the two observation episodes. To achieve this goal, we iteratively adjusted the model initial state as well as the inflow profile until the time-averaged profiles of wind speed, wind direction, and potential temperature showed reasonable agreement with the radiosonde observations during the corresponding observation episode. Figure 4.6 shows the different profiles involved in this procedure: radiosonde profiles (solid blue line), the profiles of the initial conditions ultimately used to achieve the desired model state (dashed brown line), the 1-hr averaged model profiles along the actual radiosonde path (dotted green line),

and the 1-hr averaged model profiles directly above a point near Schönbielhütte SAC (red solid line; surface point marked as red cross in Fig. 4.6d and h). The comparison of these profiles indicates that the model profiles capture the major features of the atmospheric state in both episodes. Since the radiosonde path exits the model domain somewhere in the middle troposphere, we used the vertical profiles near the Schönbielhütte SAC as representative for further analysis.

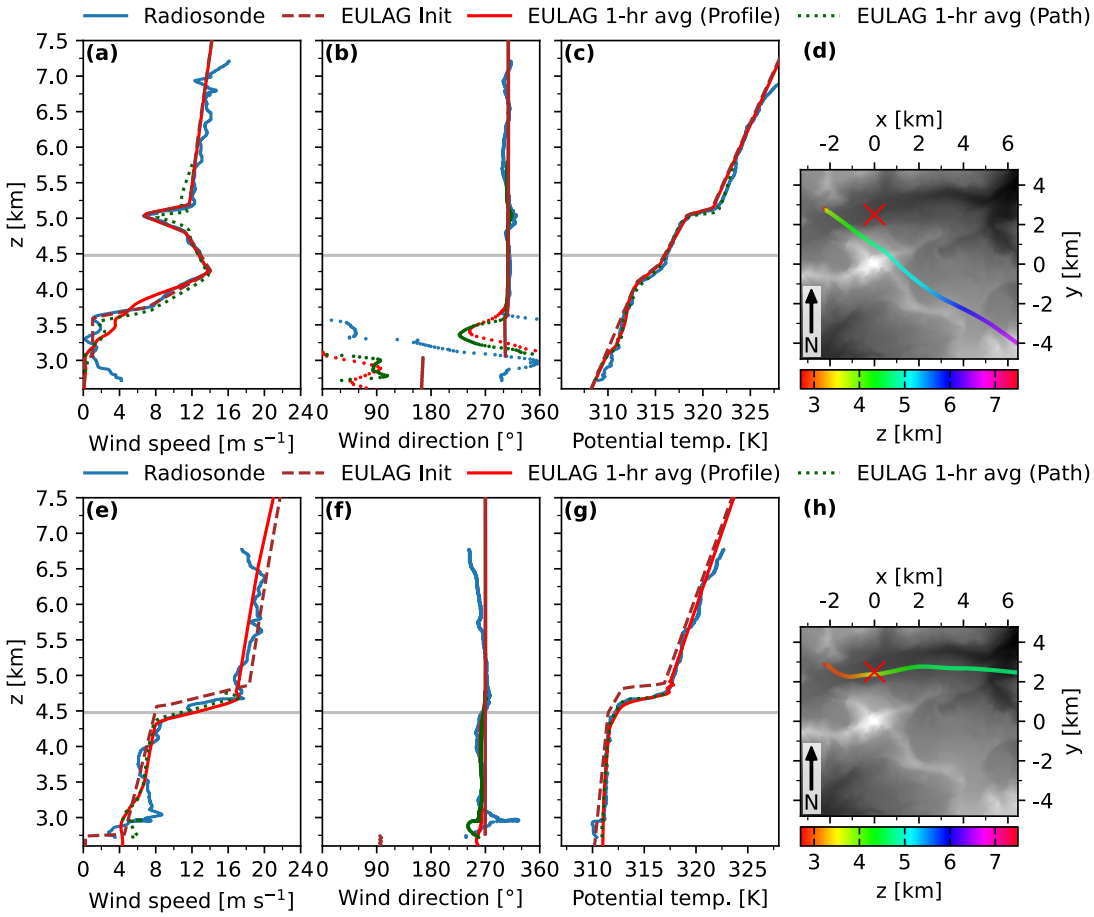

FIGURE 4.6: Profiles from the radiosonde launched at 1736 UTC (1936 CEST) 29 September (solid blue line, top row) and from the radiosonde launched at 1358 UTC (1558 CEST) 3 October (solid blue line, bottom row). The dashed brown lines depict the EULAG initial vertical profiles, the solid red lines depict the 1-hr averaged vertical profiles located at the red cross in the orography maps (panels (d) and (h)), and the dotted green lines depict the 1-hr averaged vertical profiles along the radiosonde path. Panel (d) and (h) show the radiosonde ascent path, including its altitude as multicolored line, and the terrain height increasing from black to white with coordinates centered at the Matterhorn summit. The flight time of the radiosonde along the displayed path are ≈ 24 minutes on 29 September and ≈ 16 minutes on 3 October.

At the inflow boundary, we prescribe the same wind speed and potential temperature profiles as for the initial conditions, with a zero wind extension below the altitude of the lowest point of the inflow boundary (dashed brown lines in Fig. 4.6). In both episodes, the observed wind direction is nearly independent for altitudes above 3.5 km. Correspondingly, we use one fixed value for the ambient wind direction for each episode: 308° for 29 September, and 270° for 3 October.

TABLE 4.2: EULAG model details of the two considered cases. The lowest and highest model orography heights are given by $z_{\min}$ and $z_{\max}$. The model spin-up and total simulation time are given by t_{su} and t_{sim}. The simulations use a dynamic integration time step Δt based on the CFL criterion.

	September Case	**October Case**
Observation date	29 Sep. 2023	3 Oct. 2023
Wind direction	308°	270°
Domain	$12.8 \times 9.6 \times 7.0$ km^3	$12.8 \times 9.6 \times 7.0$ km^3
δx, δy, δz	25 m	25 m
$z_{\min}$, $z_{\max}$	1936.6 m, 4475.4 m	1615.9 m, 4478.0 m
t_{su}	60 min	60 min
t_{sim}*	120 min	120 min
Δt	CFL criterion	CFL criterion

* The exact simulation time can deviate by less than 2 s due to the dynamic integration time step Δt.

4.5 Diagnostic Tools

4.5.1 Model Radial Velocity

We used our simulated wind fields to compute synthetic lidar scans, thus allowing a comparison with the observed lidar scans. For this purpose, we first interpolated the simulated wind fields onto the reference lidar grid for both the RHI and the PPI scans (see section 4.3.4). We then computed the radial velocity component through

$$v_{\text{r}} = u \sin\alpha \cos\theta + v \cos\alpha \cos\theta + w \sin\theta, \tag{4.1}$$

where u, v, and w are the simulated wind components in the x, y and z-direction.

4.5.2 Cloud Occurrence

A key aspect of this study is the diagnosis of banner clouds at the Matterhorn. Therefore, it appears odd at first sight that we restrict ourselves to the simulation of the flow of dry air. However, earlier studies indicated that moist micro-physics is of minor importance for banner cloud formation (Reinert & Wirth, 2009). The key mechanism is vertical uplift in the immediate lee of the mountain (Voigt & Wirth, 2013). As it turns out, the Lagrangian vertical displacement Δz serves as an appropriate proxy for banner cloud occurrence (Reinert & Wirth, 2009; Voigt & Wirth, 2013; Schappert & Wirth, 2015; Prestel & Wirth, 2016; Wirth et al., 2020; Thomas & Wirth, 2023). Following these earlier studies, we introduce a material tracer $\chi(\mathbf{x},t)$, for which the initial and boundary conditions are specified as $\chi = z$. The vertical displacement Δz is subsequently computed as

$$\Delta z = z - \chi \tag{4.2}$$

throughout the model domain. The sign of Δz indicates whether air parcels passing through a region originate from lower or higher altitudes. Large positive Δz are associated with an increased likelihood of cloud formation due to strong uplift and associated adiabatic cooling.

A banner cloud event is characterized by the presence of a cloud in the lee of the mountain and the absence of cloudiness on its windward side (as defined by Schween et al. (2007)). Therefore, the probability of banner cloud formation is increased when the flow field exhibits a windward-leeward asymmetry in Δz, with a plume of large positive Δz values on the leeward side. Given suitable moisture conditions, one may expect a cloud to occur on the leeward side only. In our

analysis, we estimate the spatial extent of the banner cloud using a specific positive threshold value of Δz.

4.6 Results

In this section, we present the lidar measurements for both episodes and compare them to synthetic lidar scans based on the results of our model simulations (see section 4.5.1). Moreover, we use the simulations to contextualize the lidar observations within the complex ambient flow conditions and relate them to banner cloud occurrence.

4.6.1 The September Case

We start our discussion with the first episode on 29 September. As described in section 4.3.2, there was a northwesterly ambient flow such that the leeward side was located southeast of the Matterhorn. During the chosen time interval the webcams captured a compact banner cloud (Fig. 4.2a). Figure 4.7 shows the time average composite of v_r for the observed scans.

First, we have a look at the PPI scan with $\theta = 9^\circ$ (Fig. 4.7e). This scan angle provides information about air motion at the base of the Matterhorn. The v_r field shows a north-south gradient up to a distance of 1 km from the lidar site. At larger distances, positive v_r extend over the entire azimuthal scanning range, indicating flow towards the Matterhorn. At the same time, all RHI scans in Fig. 4.7a-c show that the vertical depth of this near-surface flow is confined to the lowest 200 meters. The observed flow pattern is in some conflict with the corresponding synthetic lidar scans, which show only negligible motion at the base of the Matterhorn (Fig. 4.8e).

These small discrepancies (less than $2\,\mathrm{m\,s^{-1}}$) may be attributed to remnants of upvalley circulations that developed during the day under strong thermal forcing prior to the local sunset at 1714 UTC (1914 CEST) (Fig. 4.11). Such thermally driven circulations are not resolved in our simulation, as radiation and associated surface heat fluxes are not accounted for. Another possible explanation may be that local flow features in the radiosonde profiles below 3.5 km, which are incorporated into the initial and inflow conditions, could lead to these small discrepancies.

In contrast, the agreement between the lidar observations and the simulations improves noticeably for PPI scans with steeper elevation angles (Fig. 4.7f-h and Fig. 4.8f-h). First, there is a north-south gradient of v_r close to the lidar along $y = 0$ in both the observed and the synthetic lidar scans (compare Fig. 4.7f-h with Fig. 4.8f-h). Second, the synthetic PPI scan for $\theta = 23^\circ$ (Fig. 4.8g) shows a region of positive v_r at the southern slope, which is also observed with the lidar (Fig. 4.7g). The corresponding observed RHI scan intersecting this region (Fig. 4.7a) reveals that — discounting the data gap — positive values extend upslope and occur over a large area south of the Matterhorn summit. In this case, the synthetic scans (Fig. 4.8a and g) allow one to better estimate the spatial extent of the feature, which would remain uncertain from the observed lidar scan alone due to limitations in the data coverage. Similarly, the synthetic scans fill data gaps regarding other features, like for instance the conspicuous line separating positive and negative values of v_r south of the Matterhorn for the scans with $\theta = 16.5, 23.0$ and 27.0°. We hypothesize that this line represents flow separation along the southwestern ridge of the Matterhorn, which leads to recirculating flow south of the Matterhorn and, thereby, creates a sharp flow boundary. Moreover, the two separate patches of positive v_r visible in the observed RHI scan (Fig. 4.7a) turn out to represent one contiguous region of flow away from the lidar when referring to the corresponding synthetic scan (Fig. 4.8a).

Combining the features described above indicates recirculating flow starting near surface on the leeward side of the Matterhorn, extending through a fairly deep layer on the southern slope,

and transitioning into upslope flow. Presumably, this upslope flow leads into the banner cloud, which at this time was observed on the southeast face close to the Matterhorn summit (Fig. 4.2a).

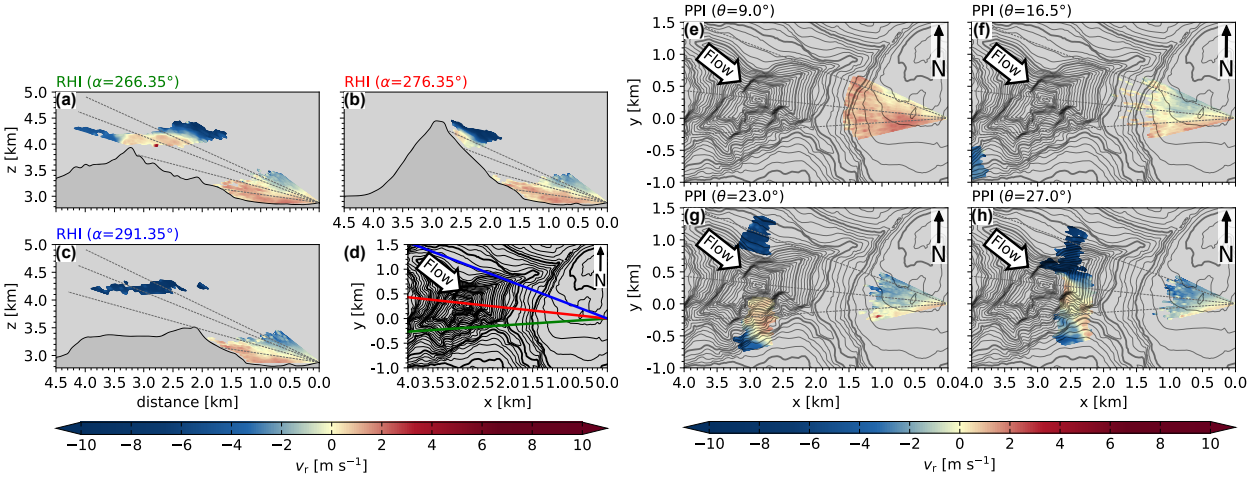

FIGURE 4.7: Time average composite of v_r (color; m s^{-1}) for RHI (left) and PPI (right) lidar scans on 29 September 2023. The time average is calculated for all grid points, for which data were available during at least three out of twelve scans (25 %) from 1648 UTC (1848 CEST) to 1808 UTC (2008 CEST) for the RHI scans (left) and from 1650 UTC (1850 CEST) to 1811 UTC (2011 CEST) for the PPI scans (right). Panel (d) shows the orientation of the three RHI scans. Black lines in the RHI panels represent terrain height. Large arrows indicate the ambient flow direction.

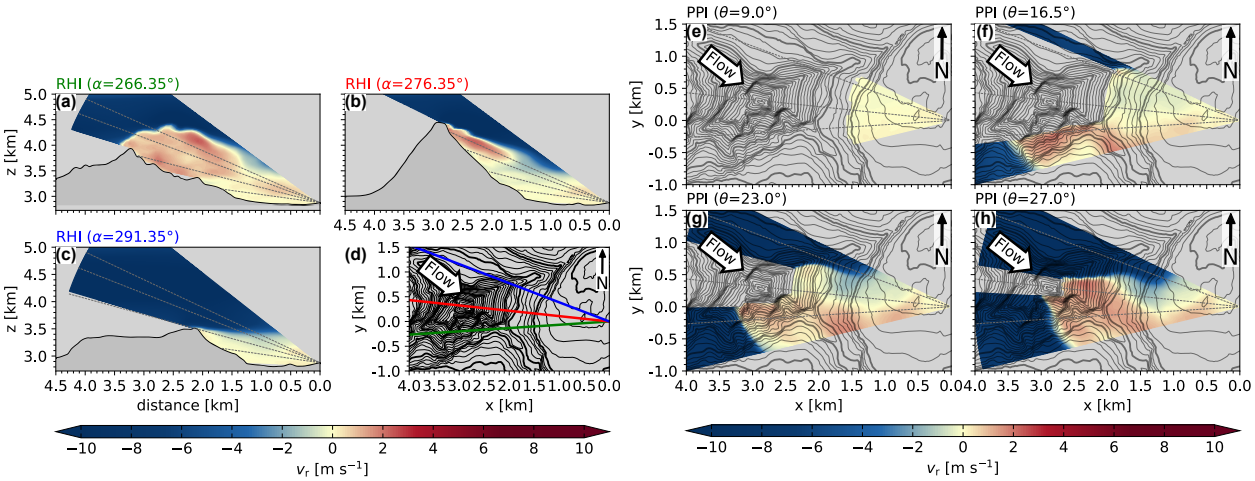

FIGURE 4.8: Synthetic RHI (left) and PPI (right) scans of v_r (color; m s^{-1}) from the 1-hr averaged simulated wind fields for the September Case after averaging over one hour. Black lines in the RHI panels represent terrain height. Large arrows indicate the ambient flow direction.

4.6.2 The October Case

We now turn to the second episode on 3 October with purely westerly flow. Figure 4.9 shows the time average composite of v_r for the observed scans, while the corresponding synthetic scans are shown in Fig. 4.10. This episode begins with the launch of the radiosonde, and includes the timing of the photograph shown in Fig. 4.2b.

As before, we begin with the shallow PPI scans with $\theta = 9.0°$ (Fig. 4.9e and Fig. 4.10e). Similar to the episode on 29 September, small discrepancies exist at lower altitudes. Comparing the

observed and the synthetic lidar PPI scan (Fig. 4.10e and Fig. 4.9e), both show a more pronounced north-south gradient of v_r compared to the episode on 29 September (Fig. 4.8e and Fig. 4.7e). Additionally, positive values of v_r (indicating leeward recirculation) are mainly limited to the southern half. However, the synthetic PPI scan also exhibits positive v_r in the northwest sector of the scan, in contrast to the observed lidar scan. This deviation extends to higher altitudes, as can be seen in the PPI scan with $\theta = 16.5°$ (Fig. 4.10f). Furthermore, the RHI scan with $\alpha = 291.35°$ (Fig. 4.10c) indicates that this motion away from the lidar must be associated with upslope flow. By contrast, the observed lidar scan (Fig. 4.9c) does not show positive v_r in this region. As with the analysis of the first episode on 29 September, we hypothesize that local flow features below 3.5 km at the radiosonde launch site, which are incorporated in the initial and inflow conditions, may contribute to the described discrepancies.

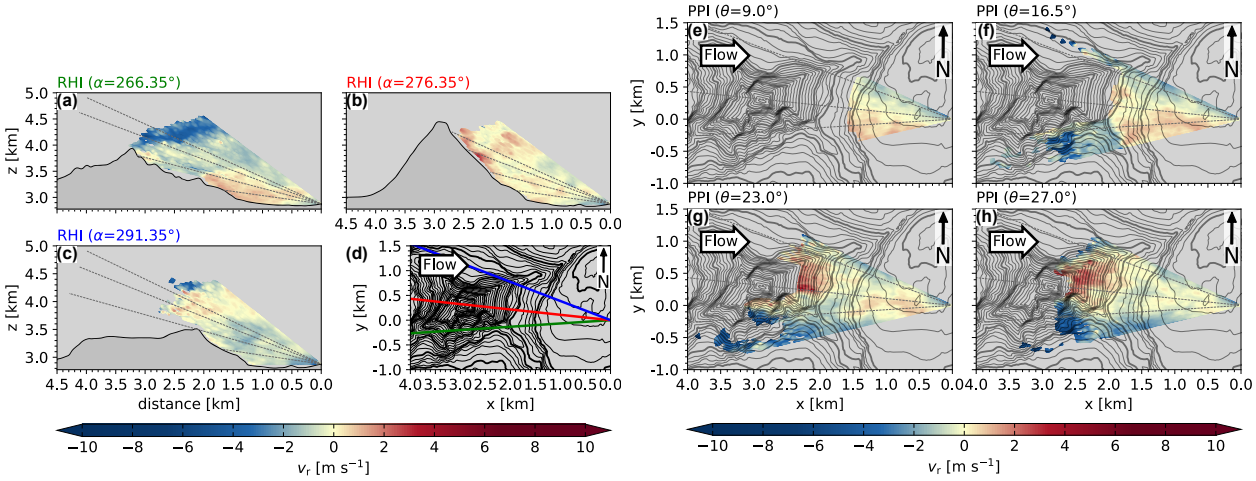

FIGURE 4.9: Time average composite of v_r (color; m s^{-1}) for RHI (left) and PPI (right) lidar scans 3 October 2023. The time average is calculated for all grid points, for which data were available during at least three out of twelve scans (25 %) from 1354 UTC (1554 CEST) to 1514 UTC (1714 CEST) for the RHI scans (left) and from 1358 UTC (1558 CEST) to 1518 UTC (1718 CEST) for the PPI scans (right). Black lines in the RHI panels represent terrain height. Large arrows indicate the ambient flow direction.

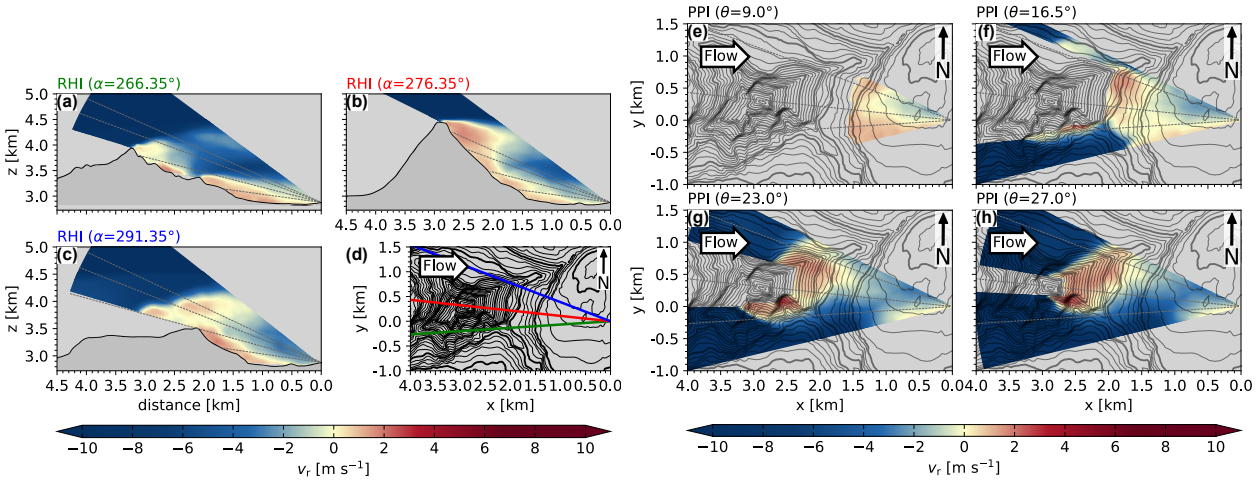

FIGURE 4.10: Synthetic RHI (left) and PPI (right) scans of v_r (color; m s^{-1}) from the 1-hr averaged simulated wind fields for the October Case after averaging over one hour. Black lines in the RHI panels represent terrain height. Large arrows indicate the ambient flow direction.

Next, we consider the steeper PPI scans (Fig. 4.9g,h and Fig. 4.10g,h), for which there is a high level of consistency between the observed and synthetic scans. For instance, both reveal a region of positive v_r located on the east face and the northeastern ridge, in contrast to the first episode on 29 September (Fig. 4.7g,h and Fig. 4.8g,h). In the RHI scans with $\alpha = 276.35°$ (Fig. 4.9b and Fig. 4.10b), these positive values are linked to upslope motion toward the Matterhorn summit, and qualitatively similar features are observed; both scans depict recirculating flow extending from the foot of the Matterhorn all the way up to its summit. It is remarkable that the observed positive values are very high, locally exceeding $2\,\mathrm{m\,s^{-1}}$, despite the fact that the composites imply time averages of a highly turbulent flow (see Fig. 4.4). Additionally, both scans indicate that the warm-colored region on the leeward side close to the summit extends by almost 1 km in the streamwise direction. Given the large elevation angle of nearly 40 degrees, this feature suggests a broad region of upwelling below a potential banner cloud. This interpretation is supported by the corresponding PPI scans with $\theta = 23.0$ and $27.0°$ (Fig. 4.9g,h and Fig. 4.10g,h), which show a region of positive v_r on the eastern side of the Matterhorn extending towards (and slightly beyond) the northeastern ridge.

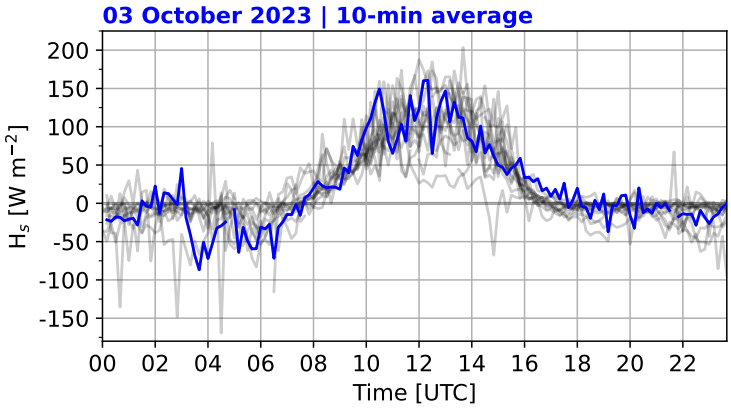

FIGURE 4.11: Time series (2 October to 16 October 2023) of observed 10-minute-averaged turbulent sensible heat fluxes near the surface at the lidar site. The data from 3 October 2023 are highlighted in blue.

4.6.3 Flow Patterns and Banner Cloud Occurrence

In the preceding subsections we demonstrated that the synthetic lidar scans from our simulations show strong consistency with the observed lidar scans in capturing key lee-side flow patterns. For both episodes we identified case-specific features in the respective scanning patterns, but these were obviously limited to the wind component v_r parallel to the lidar beam. In the next step, we take advantage of the simulations to investigate the fully three-dimensional flow fields and associate these to banner cloud occurrence.

Figure 4.12 shows one-hour time-averaged vertical displacement Δz and streamlines in horizontal cross sections for both episodes. The comparison between the two episodes reveals that the September Case (Fig. 4.12a-d) exhibits a considerably larger recirculation area, which extends far downstream in the southeastern direction. More specifically, we see two counterrotating vortices on the southern and eastern side at $z = 3500$ m (Fig. 4.12a), between which a recirculating flow transports air parcels towards the Matterhorn. The southern vortex can be seen up to a height of 4 km (Fig. 4.12b,c).

The cross sections at $z = 3750$ m and 4000 m (Fig. 4.12b,c) confirm our hypothesis in section 4.6.1: namely, that the strong gradient south of the Matterhorn in the PPI scan with $\theta = 23.0$

and 27.0° (Fig. 4.7g,h and Fig. 4.8g,h) is due to flow separation at the southwestern ridge of the Matterhorn. At this ridge, the northwesterly ambient flow encounters an easterly flow associated with the southern vortex. The other vortex on the east side of the mountain becomes distorted with increasing altitude and transforms into a directional shear line (Fig. 4.12c). This explains the sharp gradient at the same location in the synthetic PPI scan with $\theta = 27.0°$ (Fig. 4.8h).

In contrast, the October Case shows a less pronounced recirculation area, which is confined to the immediate vicinity of the mountain slope and lacks distinct vortex structures (Fig. 4.12e-h). This supports the findings of Thomas & Wirth (2023) [chapter 2], who showed that distinct vortex structures in the horizontal plane are not a necessary prerequisite of banner cloud occurrence.

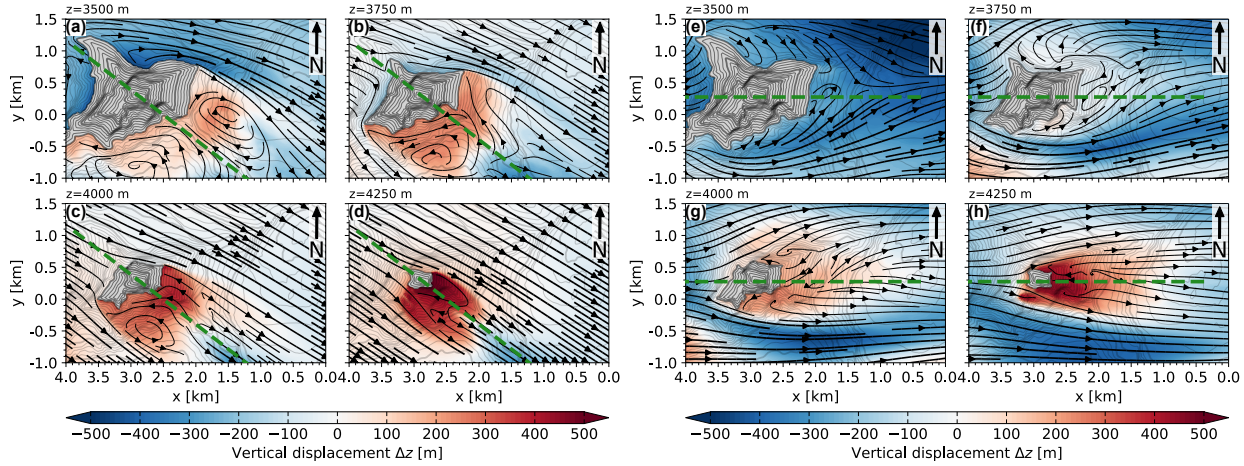

FIGURE 4.12: One-hour time-averaged vertical displacement Δz (color; m) and streamlines (black) in horizontal cross sections at $z = 3500$ m, 3750 m, 4000 m, and 4250 m for the September Case (panels (a)-(d)) and the October Case (panels (e)-(h)). The green dashed line in each panel depicts the streamwise axis through the Matterhorn summit, which will be used in the subsequent Fig. 4.13 for vertical cross sections.

For a more comprehensive description of the lee-side flow, we now examine vertical cross sections intersecting the Matterhorn summit (Fig. 4.13). In addition to the one-hour time-averaged flow state (Fig. 4.13a,c), we also consider snapshots of the simulated flow (Fig. 4.13b,d) to gain insight into the lee-side turbulent structures. In the September Case (Fig. 4.13a,b) the cross section happens to be oriented along the southeast ridge of the Matterhorn, which locally has a very steep slope. The streamlines of the time-averaged flow (Fig. 4.13a) indicate that the recirculating flow starts far downstream. At the same time not all of the corresponding streamlines reach the Matterhorn summit; on their way towards the mountain, the recirculating air parcels either gain a downward component or acquire a component perpendicular to the section associated with the southern vortex visible in Fig. 4.12b.

In the October Case (Fig. 4.13c,d), the vertical cross section is oriented west to east. The lee-side slope is more uniform, and the geometry of the recirculating flow differs quite strongly in comparison with the September Case (Fig. 4.13a,b). The streamlines of the time-averaged flow (Fig. 4.13c) indicate a strong diffluence at $(x,z) = (1.1, 3.5)$ km, which is co-located with strong confluence in the corresponding horizontal section (Fig. 4.12e). Below this altitude, downward motion dominates, combined with a wind component away from the Matterhorn. In other words, the horizontal recirculating flow is less discernible compared to the September Case. Rather, the recirculating flow is confined to a very shallow layer close to the surface and parallels the mountain slope at altitudes near the summit. This is consistent with our observed lidar scan slicing through the Matterhorn summit (Fig. 4.9b).

Finally, we turn our attention to the key diagnostic for banner cloud occurrence, namely the vertical parcel displacement Δz. Beginning with the September Case (Fig. 4.12a-d and Fig. 4.13a,b), both the horizontal and the vertical distribution of positive values indicate widespread upward displacement from lower altitudes. In contrast, the October Case (Fig. 4.12e-h and Fig. 4.13c,d) exhibits a different pattern, with positive values confined to altitudes above 3.8 km. Comparing the vertical displacement snapshots of both cases (Fig. 4.13b,d), the October Case reveals distinct vortex patterns. These differences are further accentuated by the animation of the vertical displacement available in the supplementary material. This contrasts with the previous comparison of the time-averaged flow in the horizontal plane, where no clear vortex structures were observed in the October Case. However, this does not preclude the presence of transient vortex structures in the vertical plane.

In both, the September and October Case, the largest vertical displacement is consistently found on the leeward side in the immediate vicinity of the Matterhorn summit. Moreover, the leeward-windward asymmetry of Δz is very strong, indicating a high potential for banner cloud occurrence (Prestel & Wirth, 2016; Thomas & Wirth, 2023). A fully three-dimensional rendition of the diagnosed banner cloud for both cases is shown in the small panels in Fig. 4.14. The comparison with the snapshots from the webcam reveals a strong structural similarity. This underlines that Δz is a valuable diagnostic for banner cloud occurrence in different flow conditions, enhancing confidence in our simulations. The utility of Δz for banner cloud occurrence is further supported by Fig. 4.17 in the supplementary material, which shows the one-hour time-averaged vertical displacement for two additional episodes of the campaign when no banner cloud was observed. The characteristic leeward-windward asymmetry of Δz is evident only for the first out of the two episodes (Fig. 4.17a). The scale analysis of **Hoch et al. (2025)** [chapter 3] suggests that only this episode exhibits conditions that are conducive to banner cloud formation.

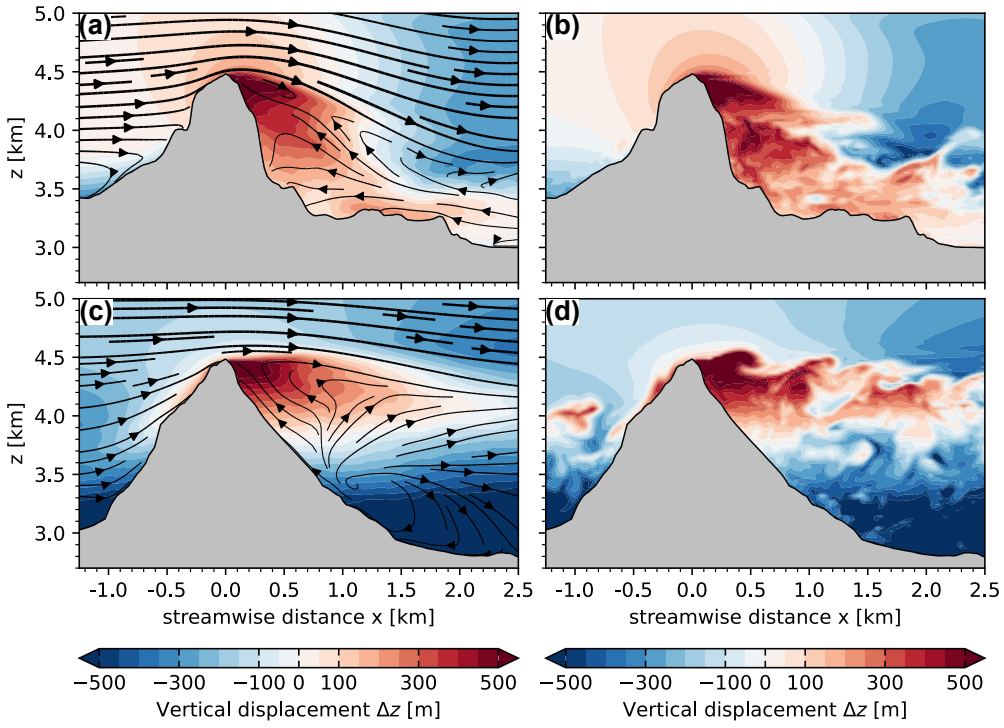

FIGURE 4.13: Banner cloud proxy obtained from the LES model in a vertical cross section in streamwise direction. The left panels show the one-hour time-averaged vertical displacement Δz (color; m) and streamlines (black lines) for (a) the September Case and (c) the October Case. The right panels show a snapshot of vertical displacement Δz (color; m) for (b) the September Case and (d) the October Case. The respective section is depicted in Fig. 4.12 by the green dashed lines. Black lines represent terrain height. The x-axis is centered at the Matterhorn summit.

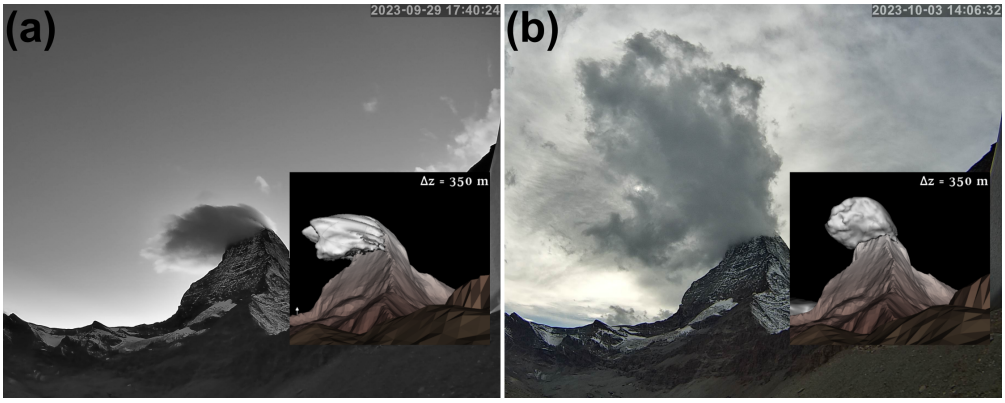

FIGURE 4.14: Comparison between observed and simulated banner cloud occurrence: (a) at 1740 UTC (1940 CEST) 29 September 2023 and (b) at 1407 UTC (1607 CEST), 3 October. In both panels, the photo images are taken from the webcam installed near Hirli northeast of the Matterhorn, and the small insets depict the simulated banner cloud volume as diagnosed through the one-hour time-averaged isosurface $\Delta z = 350$ m.

4.7 Summary and Conclusions

This paper analyzed data from a campaign named MatterHEX. In this campaign, a scanning Doppler lidar was used for the first time in lee of the Matterhorn to determine the flow field associated with banner cloud occurrence. Focusing on two episodes of banner cloud occurrence, we compared the observational data with Large-Eddy Simulations conducted using the EULAG model (Prusa et al., 2008). The simulations were initialized using radiosonde profiles from the campaign to ensure proper representation of ambient atmospheric conditions. Model-based radial velocities were compared to the observed lidar retrievals with the aim to lend confidence into the model's ability to resolve the relevant lee-side flow structures.

For the analysis of the lidar data, we used a combination of conventional threshold filtering and the DBSCAN algorithm (Ester et al., 1996) to optimize lidar retrievals in the aerosol-scarce high-altitude atmosphere. Our simulations used inflow profiles that were tuned to match the simulated ambient flow to our radiosonde observations. Moreover, a rotation of the orography within the model domain allowed us to simulate the two different ambient wind directions.

Naturally, our lidar observations are limited to the wind component along the line-of-sight. However, combining this information with the knowledge of the orography allowed us to estimate motion along the mountain slopes. This way we confirmed the hypothesized key mechanism for banner cloud formation that had emerged from previous model studies: namely the lee-side re-circulating flow which, in combination with the steep mountain slope, results in strong lee-side upwelling.

We carried through a systematic comparison between the lidar and the model data based on time averages of about one hour. Overall, we found a reasonable level of agreement. Only small discrepancies arise close to the surface in the basin between the Matterhorn and the lidar site. Additional radiosonde measurements in this area would be required to provide a more comprehensive characterization of the lower atmospheric flow in the model. In our case this was not feasible due to terrain-specific constraints and logistical limitations.

Our analysis is limited to two cases from a short experimental campaign, and some question on banner clouds remain that can not be answered here. For instance, we do not have enough data to evaluate diurnal or seasonal trends in banner cloud occurrence at the Matterhorn (cf. Wirth et al. (2012)). Other questions that are not addressed in our analysis of time averaged flows relate to the details of the turbulent flow features. For example, we could not address features such

as temporal variability from vortex shedding. **Hoch et al. (2025)** [chapter 3] took an important first step by showing that individual lidar retrievals from our measurement campaign resolved parts of the lee-side turbulent structures. However, fully capturing the dynamics of these flows requires measurements capable of resolving both their complete spatial structure and high temporal variability.

Despite these limitations, the general agreement between observations and simulations gave us confidence that the model resolves the dynamic processes at the relevant spatial and temporal scales to successfully simulate the flow features responsible for banner cloud formation. In summary our results provide circumstantial evidence that banner cloud formation at the Matterhorn is a robust phenomenon that may occur under a wide range of ambient flow conditions. In particular, distinct vortex structures in the horizontal plane on the leeward side of the mountain are not a necessary prerequisite, consistent with the results of Thomas & Wirth (2023) [chapter 2]. We demonstrated through direct comparison with webcam images that the vertical displacement is a useful model diagnostic for banner cloud occurrence. It follows that moist cloud physics is unlikely to play a dominant role, consistent with the findings of Reinert & Wirth (2009). This transpires that previous results from model-based investigations are, indeed, relevant in the real world — at least at a steep mountain like the Matterhorn. Finally, this study highlights the value of a synergetic use of observations and simulations to gain insight into the three-dimensional nature of flow patterns in steep and complex terrain.

4.8 Acknowledgments

The corresponding author is grateful to the entire MatterHEX team for successfully carrying out the measurement campaign in the complex terrain. All figures were generated with the Python matplotlib package (Hunter, 2007) and vedo package (Musy et al., 2020). Parts of this research were conducted using the supercomputer MOGON 2 and/or advisory services offered by Johannes Gutenberg University Mainz (hpc.uni-mainz.de), which is a member of the AHRP (Alliance for High Performance Computing in Rhineland Palatinate, www.ahrp.info) and the Gauss Alliance e.V.. This research was funded by the Deutsche Forschungsgemeinschaft (DFG, German Research Foundation)–432130757, including funding for Sebastian W. Hoch as Mercator Fellow. Sebastian W. Hoch was partially supported by the NSF National Center for Atmospheric Research, which is a major facility sponsored by the U.S. National Science Foundation under Cooperative Agreement No. 1852977. Hendrik Huwald is a member of the UrbanTwin and SPEED2ZERO Joint Initiatives, which received financial support from the ETH Board under the Joint Initiatives scheme. Brandon J. A. van Schaik is a participant in the EPFLGlobal Leader program, which is funded by the European Union's Horizon 2020 research and innovation program under the Marie Skłodowska-Curie grant agreement No 945363.

4.9 Data Availability Statement

The field campaign and simulation data necessary for re-producing figures in this study are available at https://doi.org/10.5281/zenodo.14644747

4.10 Supplementary material

4.10.1 Lidar Data Coverage

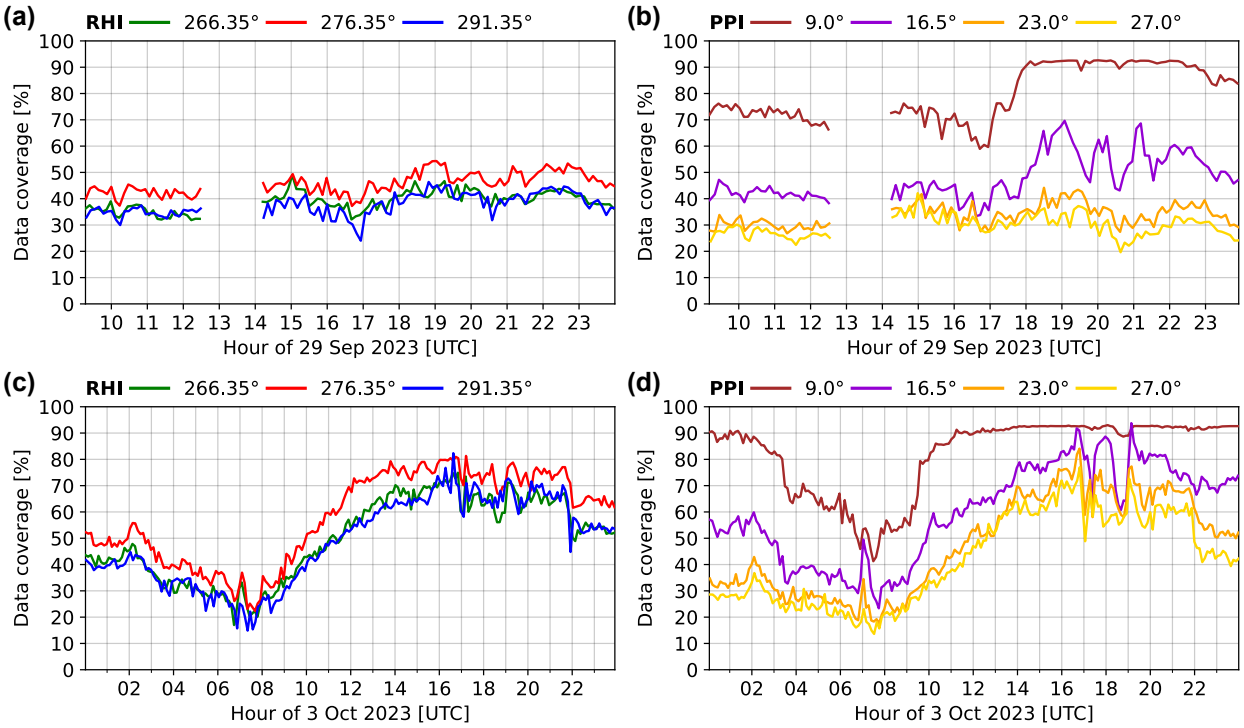

FIGURE 4.15: Time series of the data coverage (%) integrated along each RHI and PPI scanning range (a,b) on 29 September 2023 and (c,d) on 3 October 2023. On 29 September lidar data was only available from 0930 UTC (1130 CEST), with a brief interruption between 1230 UTC (1430 CEST) and 1400 UTC (1600 CEST) due to maintenance work.

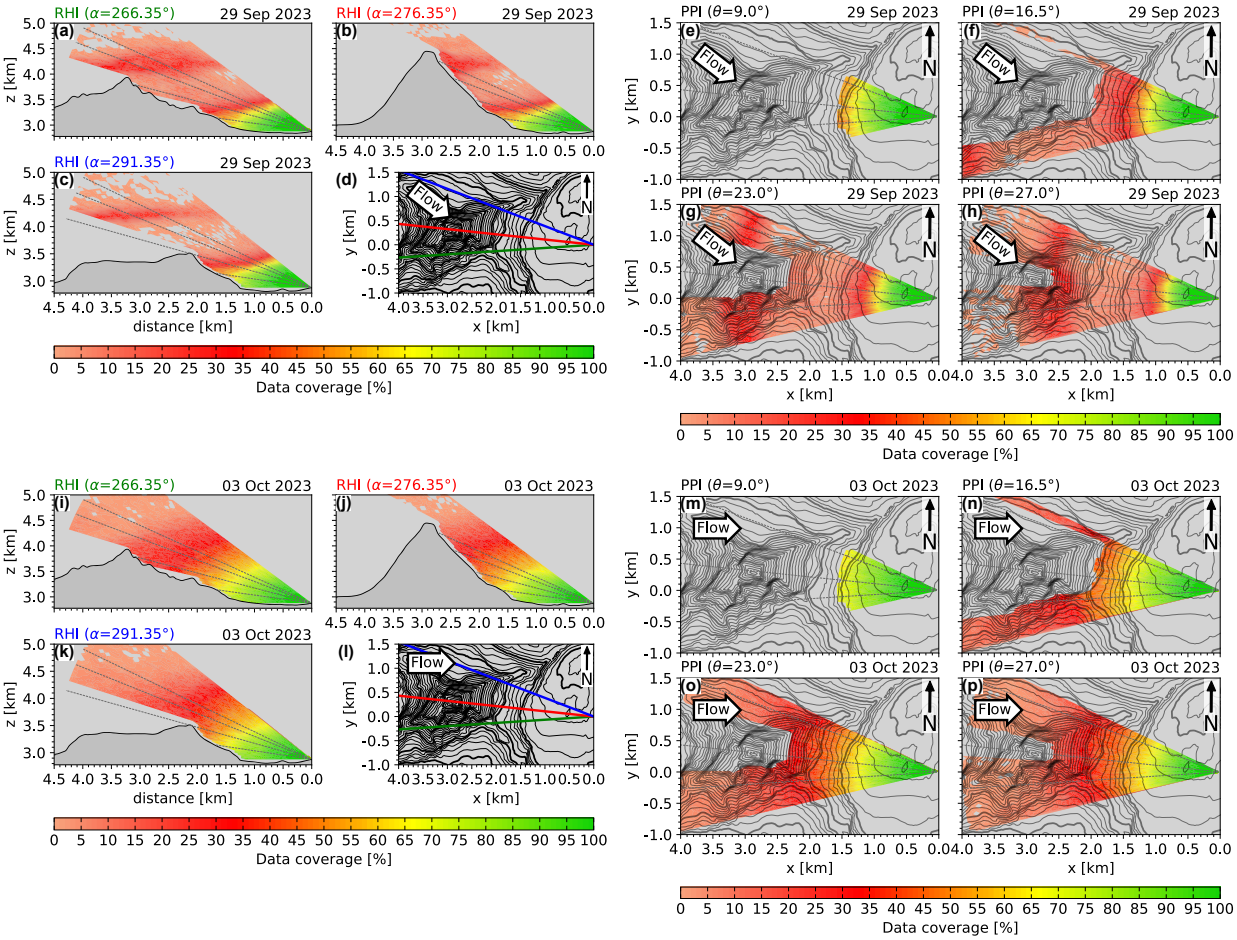

FIGURE 4.16: Data coverage (color; %) for RHI and PPI scans integrated on (a-h) 29 September 2023 and (i-p) 3 October 2023. Gray dashed lines in the RHI and PPI scans represent the PPI and RHI scan lines, respectively. Black lines in the RHI scans indicate the terrain height. Ambient flow direction is indicated by the large arrows.

4.10.2 Lagrangian Vertical Displacement: Two Episodes without Banner Cloud Observation

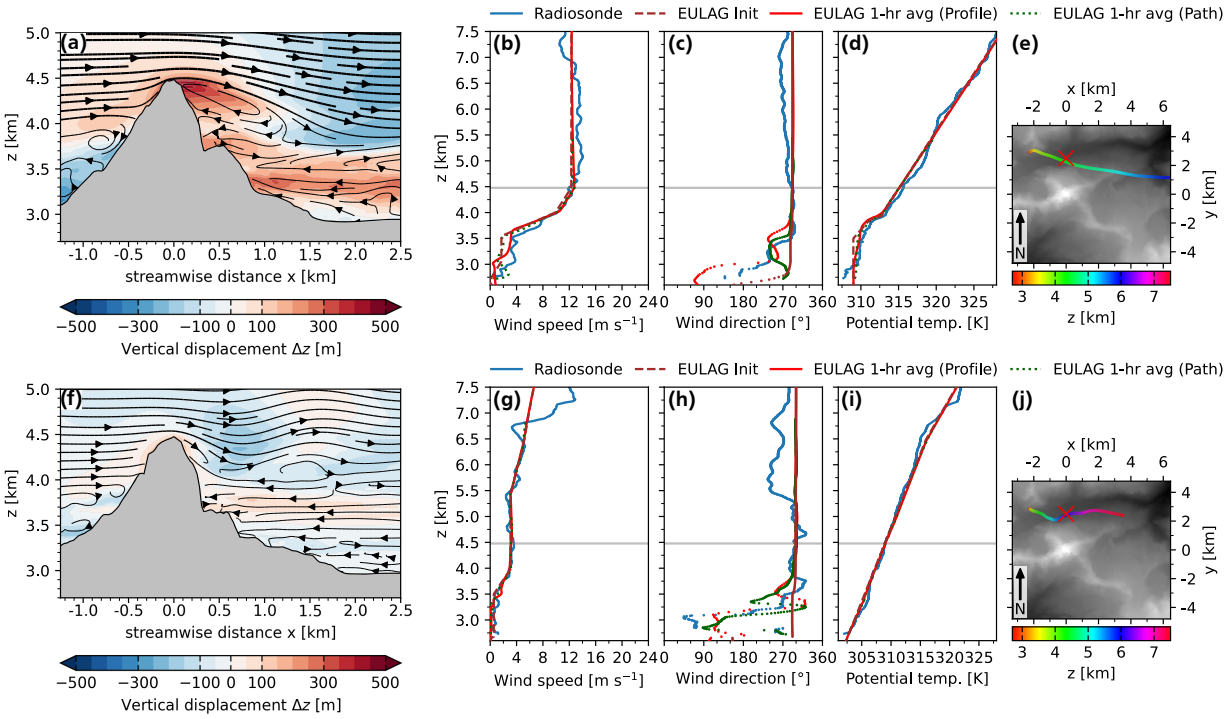

FIGURE 4.17: One-hour time-averaged banner cloud proxy Δz (color; m) and streamlines (black) for (a) 12 October and (f) 16 October along the streamwise axis through the Matterhorn summit. The black lines in both panels indicate the terrain height. Panels (b)-(d) and panels (g)-(i) show profiles from the radiosonde launched at 1632 UTC (1832 CEST) 12 October and at 0906 UTC (1106 CEST) 16 October as solid blue line, respectively. The dashed brown lines depict the EULAG initial vertical profiles, the solid red lines depict the 1-hr averaged vertical profiles located at the red cross in the orography map (panels (e) and (j)), and the dotted green lines depict the 1-hr averaged vertical profiles along the radiosonde path. Panels (f) and (j) show the radiosonde ascent path, including its altitude as multicolored line, and the terrain height increasing from black to white with coordinates centered at the Matterhorn summit. The flight time of the radiosondes along the displayed path are $\approx$ 15 minutes on 12 October and $\approx$ 26 minutes on 16 October.

5 Summary and Conclusions

This thesis investigated the key mechanisms of banner cloud formation over complex terrain under realistic conditions, using the Matterhorn in the Swiss Alps as a natural laboratory. Therefor, dry Large-Eddy Simulations (LES) using the EULAG model with the highly complex orography of the Matterhorn were conducted and evaluated using observational data from the dedicated MatterHEX field campaign. The campaign provided the first systematic observation of leeside flow features and atmospheric conditions relevant to banner clouds. The dataset involved upwind flow conditions from radiosondes, leeside flow patterns captured by a Doppler lidar, and banner cloud development monitored via webcams. The main objective was to evaluate to what extent the key mechanisms identified in previous idealized studies, namely flow separation associated with a recirculating flow and strong upwelling on the leeward side, persist under realistic orographic and atmospheric conditions.

The initial part of the thesis used LES to examine how increasing orographic complexity, ranging from an idealized pyramid to the fully realistic orography of the Matterhorn, affect the flow structures governing banner cloud formation. The results confirm that banner cloud formation remains primarily driven by dynamically induced upwelling in the leeside recirculation region, though the detailed flow structure is strongly shaped by terrain complexity. Realistic orography was shown to reduce flow symmetry and coherence of vortices seen for the idealized pyramid case. In addition, the region of strong upwelling was no longer necessarily confined to the leeward side but extended toward the spanwise mountain slopes. This was reflected in backward trajectory analysis which showed that most parcels ascended along the southern face before finally being lifted into the banner cloud on the leeward side. Further sensitivity experiments revealed that weak stratification in the lee of the Matterhorn is essential for banner cloud formation, but is subject to a clear dependence on wind speed, especially under conditions without wind shear. It must be either a property of the ambient flow or generated through turbulence arising from the interaction with the terrain in case of high wind speeds.

To evaluate these simulation-based findings against real-world data, the MatterHEX field campaign was conducted to observe banner cloud formation under natural conditions. Despite challenges posed by the high-altitude, aerosol scarce environment, a combination of conventional SNR-threshold filtering with the DBSCAN clustering algorithm recovered meaningful lidar retrievals. As a complementary approach to lidar analysis, the ambient flow conditions observed by radiosondes were also categorized using the theoretical flow regime framework developed by Baines (1995). All banner cloud episodes corresponded to the flow regime associated with leeside flow separation. Moreover, this regime occurred more frequently than actual banner cloud observations would suggest, likely due to insufficient moisture for cloud formation despite strong uplift. During one banner cloud episode, time-averaged radial velocity retrievals indicated flow separation associated with strong flow reversal and upwelling. Individual scans further captured parts of turbulent structures such as Kelvin–Helmholtz billows. These results confirmed that the quality-controlled lidar dataset resolved the relevant spatial and temporal scales of the leeside flow, enabling for the first time a direct validation of LES results under realistic conditions.

Observations from two contrasting banner cloud episodes were selected for validation. One

featured near-neutral stratification with increased wind speed near the summit; the other exhibited weak stratification and high shear below the summit. In both cases, the model inflow conditions were tuned to match the time-averaged ambient flow to the upwind flow conditions from radiosonde observations. Model-based radial velocities were derived from time-averaged flow fields to enable direct comparison with observed lidar retrievals. The observed and simulated time-averaged radial velocities demonstrated a reasonable level of agreement in capturing the key mechanisms of banner cloud formation for both episodes. This agreement was further corroborated by the strong structural similarity between the diagnosed banner clouds based on plumes of large Lagrangian vertical displacement and the observed banner cloud. For example, the diagnosed banner cloud continuously shed downstream, resembling Kelvin–Helmholtz billows in accordance with the visual observations during the campaign. Together, these findings highlight that banner cloud formation at the Matterhorn is a robust phenomenon that can occur under a wide range of flow conditions. Moreover, the close agreement between LES and observations confirms that the model reliably captures the relevant leeside flow structures in highly complex terrain, demonstrating the applicability of model-based results to real-world conditions.

Through the synergetic use of observations and simulations, this thesis confirmed that previous model-based key mechanisms of banner cloud formation are relevant under real-world conditions, at least on the scale of the Matterhorn in the Swiss Alps. However, there were some limitations related to the design of the field campaign and the model configuration applied, which leave room for future investigations. For example, the temporal coverage of the field campaign was relatively short, and observations were largely confined to daylight hours, as webcam data were often unreliable at night. As a result, the number of documented banner cloud episodes was limited, and the dataset did not allow for an assessment of potential diurnal or seasonal trends. While the LES captured the essential dynamics, small discrepancies appeared near the surface in the basin between the Matterhorn and the lidar site. These might be caused by remnants of thermally driven circulations that may have developed during the day but were not represented in the model due to the absence of radiation and surface heat fluxes. Alternatively, local flow features in the radiosonde profiles may have affected the simulated flow via the prescribed initial and inflow conditions. Addressing this issue would require a more comprehensive characterization of the lower atmospheric flow through additional observations, such as ground-based instruments or additional radiosondes, which were not feasible during MatterHEX due to terrain constraints and logistical limits. Furthermore, although both the lidar scans and LES captured turbulent structures such as Kelvin-Helmholtz billows, a full characterization of the underlying dynamics would require more comprehensive measurements capable of resolving both the spatial structure and the high temporal variability of the flow. These turbulent flows and regions of upwelling are likely not confined to dry fair-weather cases but may also occur in conditions involving deep clouds and precipitation, possibly enhancing leeside snowfall. Investigating this potential link would require another field campaign deploying ground-based or airborne Doppler radar systems.

To conclude, this thesis makes an important contribution to the research of flow past steep mountains, with special focus on banner cloud formation mechanisms at the Matterhorn. While theoretical and idealized approaches are essential for developing conceptual understanding, their verification with observational reference is equally important. By bridging this gap, the thesis demonstrates the potential of the synergetic use of LES and observations to improve our understanding of flow structures under real-world conditions. It not only shows that simulations with extremely steep and realistic orography are feasible, but also how they can be tested against observations. This integrated approach sets a precedent for future studies aiming to resolve and validate small-scale atmospheric processes in complex terrain.

A Large-Eddy Simulation Model — EULAG

For the numerical simulations in this thesis it is used the EULAG (**EU**lerian/semi-**LAG**rangian) model, a computational fluid dynamics solver designed for multiscale atmospheric and geophysical flows (Prusa et al., 2008; Smolarkiewicz & Charbonneau, 2013; Smolarkiewicz et al., 2014). EULAG features a non-hydrostatic formulation on a generalized, time-dependent and curvilinear grid, and supports both Eulerian flux-form and Lagrangian advective-form equations (Smolarkiewicz & Margolin, 1997):

$$\frac{\partial}{\partial t}(\mathscr{G}\rho\psi) + \nabla\cdot(\mathscr{G}\rho\boldsymbol{u}\psi) = \mathscr{G}\rho R \tag{A.1}$$

$$\frac{\partial\psi}{\partial t} + \boldsymbol{u}\cdot\nabla\psi = R, \tag{A.2}$$

where $\mathscr{G} = \mathscr{G}(\boldsymbol{x},t)$ denotes the Jacobian of coordinate transformations, $\rho = \rho(\boldsymbol{x},t)$ represents the dependent or constant fluid density based on the utilized physical model, $\psi = \psi(\boldsymbol{x},t)$ represents a specific fluid property expressed per unit of mass, $\boldsymbol{u} = \boldsymbol{u}(\boldsymbol{x},t)$ represents the flow velocity, and R encapsulates all external and internal forces affecting the variable ψ. This flexibility makes EULAG versatile for diverse flow scenarios from laboratory and wind tunnel experiments (Smolarkiewicz et al., 2007; Waite & Smolarkiewicz, 2008) to global scales (Smolarkiewicz et al., 2001; Elliott & Smolarkiewicz, 2002). In this thesis, Large-Eddy Simulations are performed using EULAG with the Eulerian flux-form option.

In the following, section A.1 introduces the governing equations, based on the numerical framework outlined in Smolarkiewicz et al. (2014), with a focus on the mathematical formulations and EULAG configurations relevant to this work. Section A.2 describes the numerical integration scheme used to solve the governing equations. Section A.3 explains how the steep and complex orography is implemented into the EULAG model. Finally, section A.4 describes how subgrid-scale turbulence is represented.

A.1 Governing Equations

It is employed the compressible dynamical core with dry flows, excluding surface heat fluxes and radiation effects, in a non-rotating reference frame on a Cartesian grid ($\mathscr{G} = 1$). The orography is represented through an immersed boundary method (see section A.3). In addition, absorbers at the model domain boundaries are used to damp the flow velocity and potential temperature to the ambient state in order to minimize wave reflections. This results in the following system of

compressible equations:

$$\frac{d\boldsymbol{u}}{dt} = -\frac{\theta}{\theta_0}\nabla\varphi - \boldsymbol{g}\frac{\theta'}{\theta_a} - \beta\boldsymbol{u} - \alpha_m\boldsymbol{u}', \tag{A.1.1}$$

$$\frac{d\theta'}{dt} = -\boldsymbol{u}\cdot\nabla\theta_a - \beta(\theta-\theta_B) - \alpha_h\theta', \tag{A.1.2}$$

$$\frac{d\rho}{dt} = -\rho\nabla\cdot\boldsymbol{u}, \tag{A.1.3}$$

Here, $\boldsymbol{u}(\boldsymbol{x},t)$ represents the flow velocity, $\theta(\boldsymbol{x},t)$ the potential temperature, $\rho(\boldsymbol{x},t)$ the density of dry air, and $\boldsymbol{g}=(0,0,-g)$ the gravitational acceleration. In addition, $\varphi = c_p\theta_0\pi'$ denotes a perturbation in the generalized Exner pressure π, where c_p is the specific heat at constant pressure, and θ_0 is a constant reference value for θ. The differential operators d/dt and the nabla $\nabla=(\partial_x,\partial_y,\partial_z)$ are used in their generic form, where $d/dt = \partial/\partial t + \boldsymbol{u}\cdot\nabla$. The "$'$" denotes perturbations with respect to a balanced ambient state denoted by the subscript "a", expressed as $\boldsymbol{u}' = \boldsymbol{u}-\boldsymbol{u}_a$, $\theta' = \theta-\theta_a$ and $\pi' = \pi-\pi_a$. In the publications of this research the ambient state equals the initial and inflow profiles. The relaxation terms with the coefficients $\alpha_{m,h}$ and β represent fictious forcings, which attenuate the flow to the ambient state within absorber layers at the model domain boundaries and to the prescribed states within the orography (denoted by the subscript "B") (Smolarkiewicz et al., 2007).

From these equations, θ' is obtained prognostically, while π' is derived by $\rho\cdot$A.1.1 and forming the divergence. The resulting elliptical pressure equation is then solved iteratively:

$$\nabla^2\pi' = -\frac{1}{c_p\theta}\nabla\cdot\left[\boldsymbol{g}\frac{\theta'}{\theta_a} + \frac{\partial}{\partial t}(\rho\boldsymbol{u}) + \nabla\cdot(\rho\boldsymbol{u}\otimes\boldsymbol{u}) + \beta\boldsymbol{u} + \alpha_m\boldsymbol{u}'\right] \tag{A.1.4}$$

A.2 Numerical Integration Scheme

In the EULAG configuration used in this thesis, the prognostic equations (A.1.1-A.1.3) are solved by reformulating them into flux form. Therefore, it is combined $\rho\cdot$A.1.1 with $\boldsymbol{u}\cdot$A.1.3, and $\rho\cdot$A.1.2 with $\theta'\cdot$A.1.3, and the right-hand side of Eq. A.1.3 with the total derivative $d\rho/dt$ on the left-hand side of Eq. A.1.3 (Kurowski et al., 2014):

$$\frac{\partial\rho\boldsymbol{u}}{\partial t} + \nabla\cdot(\rho\boldsymbol{u}\otimes\boldsymbol{u}) = \rho\boldsymbol{R}^{\boldsymbol{u}}, \tag{A.2.1}$$

$$\frac{\partial\rho\theta'}{\partial t} + \nabla\cdot(\rho\theta'\boldsymbol{u}) = \rho R^{\theta'}, \tag{A.2.2}$$

$$\frac{\partial\rho}{\partial t} + \nabla\cdot(\rho\boldsymbol{u}) = 0. \tag{A.2.3}$$

Here, $\boldsymbol{R}^{\boldsymbol{u}}$ and $R^{\theta'}$ symbolize the forcings on the rhs of Eq. A.1.1 and Eq. A.1.2, respectively, and $\otimes$ denotes the tensor product. Then, the prognostic equations of momentum (Eq. A.2.1) and potential temperature (Eq. A.2.2) are generalized into a generic conservation law,

$$\frac{\partial\rho\psi}{\partial t} + \nabla\cdot(\rho\boldsymbol{u}\psi) = \rho R^{\psi}, \tag{A.2.4}$$

with ψ symbolizing the three components of the velocity vector $\boldsymbol{u}$ and the potential temperature perturbation θ', while R denotes the associated rhs of Eq. A.2.1 and Eq. A.2.2.

For the numerical integration EULAG utilizes a nonoscillatory forward-in-time (NFT) approach (Prusa et al., 2008):

$$\psi_i^{n+1} = LE_i\left(\widetilde{\psi}^n, \boldsymbol{V}^{n+1/2}, \rho^n, \rho^{n+1}\right) + 0.5\delta t R_i^{\psi}|^{n+1}, \tag{A.2.5}$$

with LE_i representing the second-order-accurate non-oscillatory advection scheme MPDATA (**M**ultidimensional **P**ositive **D**efinite **A**dvection **T**ransport **A**lgorithm) (Smolarkiewicz & Margolin, 1998) with the following dependencies: (1) the auxiliary field $\widetilde{\psi}_i^n \equiv \psi^n + 0.5\delta t R^n$, (2) an second-order-accurate estimate of the transportive momentum $\boldsymbol{V}^{n+1/2}$ at intermediate time levels $t^{n+1/2} = t^n + 0.5\delta t$, (3) the density $\rho(\boldsymbol{x},t)$, and (4) the preceding integration of the prognostic mass continuity Eq. A.2.3 with

$$\rho_i^{n+1} = \mathscr{A}_i\left(\rho^n, \boldsymbol{u}^{n+1/2}, \mathscr{I}, \mathscr{I}\right), \tag{A.2.6}$$

where $\mathscr{I}(\boldsymbol{x},t) \equiv 1$. The integration in Eq. A.2.6 provides the transportive momentum as the cumulative mass flux defined as $\boldsymbol{V}^{n+1/2} = \overline{\rho \boldsymbol{u}}^{n+1/2}$ (see Appendix B in Smolarkiewicz et al. (2014) for details). These updates ensure that the transport operator $\mathscr{A}$ in Eq. A.2.5 is consistent with mass conservation (Kurowski et al., 2014).

A.3 Implementation of Complex Orography

EULAG offers two approaches for handling topographical features: terrain-following coordinates (Fig. A.1a) and the immersed boundary method (Fig. A.1b). In the first approach model levels align with the terrain contours on a non-orthogonal grid. However, this method can result in numerical instabilities for very steep orography shapes like a Pyramid. Therefore, previous studies on banner clouds adopted the second option, the immersed boundary method (Voigt & Wirth, 2013; Schappert & Wirth, 2015; Prestel & Wirth, 2016). In this method the terrain is embedded within a Cartesian grid (Fig. A.1b). At grid points below the surface (red dots in Fig. A.1b) fictitious body forces are introduced into the equations of motion and the potential temperature perturbation (β in Eq. A.1.2 and Eq. A.1.1), which attenuate the flow to prescribed states, u_B and θ_B. To emulate the effect of an obstacle u_B is set to zero at the grid points below the surface (Goldstein et al., 1993; Mittal & Iaccarino, 2005; Smolarkiewicz et al., 2007). This approach effectively represents a no-slip boundary condition but lacks explicit control over surface friction. However, this limitation is no disadvantage for the investigation of banner clouds, as strong surface friction is required for their formation (Prestel & Wirth, 2016).

For simulations with "flat portions" of the implemented orography surface stress is parameterized as

$$\boldsymbol{\tau} = \rho_0 C_d \sqrt{u_0^2 + v_0^2}\, \boldsymbol{v_0}, \tag{A.3.7}$$

where $\boldsymbol{v_0} = (u_0, v_0)$ is the horizontal velocity at the surface, $C_d = 0.01$ is the drag coefficient and ρ_0 is the air density at the surface.

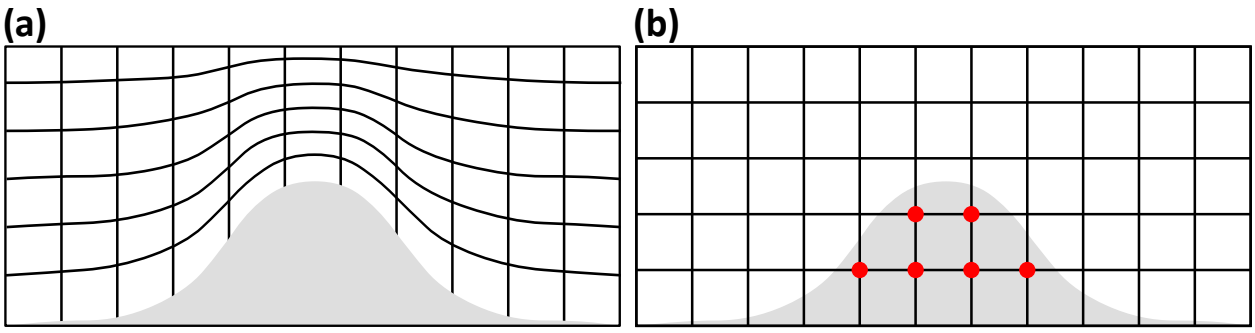

FIGURE A.1: Terrain-following coordinate system versus immersed boundary method.

A.4 Subgrid-Scale Modeling

In this thesis, LES are carried out, which is a compromise between Direct Numerical Simulations (DNS), where all turbulent motions are fully resolved, and Reynolds-Averaged Navier-Stokes (RANS) simulations, which resolve only ensemble-averaged quantities while modeling all turbulent motions (Fröhlich, 2006). LES explicitly resolves the larger, energy-containing eddies while modeling smaller-scale eddies as subgrid-scale motions. This approach is based on the assumption of an energy cascade, where larger eddies extract kinetic energy from the mean flow and transfer it to smaller eddies, which ultimately dissipate turbulent kinetic energy (TKE) into internal energy through molecular viscosity (Stull, 1988). In EULAG the grid spacing serves as the cutoff length scale to isolate the resolved from the unresolved eddies.

The effects of unresolved eddies on the dynamics of the resolved scales are represented by a TKE scheme (Deardorff, 1973; Schumann, 1991; Sorbjan, 1996):

$$\tau_{ij} = -k_m \left(\frac{\partial \overline{u}_i}{\partial x_j} + \frac{\partial \overline{u}_j}{\partial x_i} \right) \tag{A.4.8}$$

$$\mathscr{H}_j = -k_h \frac{\partial \overline{\theta}}{\partial x_j}. \tag{A.4.9}$$

Here, τ_{ij} represents the subgrid-scale stress and $\mathscr{H}_j$ the turbulent heat flux, which involve the resolved velocity $\overline{u}$ and potential temperature $\overline{\theta}$. The eddy viscosity k_m and the eddy diffusivity k_h are functions of the subgrid-scale turbulent kinetic energy tke, the mixing length λ, and the Prandtl number Pr:

$$k_m = c_m \lambda \sqrt{tke} \quad \text{with} \quad \lambda = min(\Delta, c_l z) \tag{A.4.10}$$

$$k_h = \frac{k_m}{Pr}, \tag{A.4.11}$$

where $\Delta = 1/3(\Delta x + \Delta y + \Delta z)$, and Δx, Δy, and Δz are grid spacings in the three spatial dimensions. The subgrid-scale turbulent kinetic energy tke is retrieved by solving the transport equation

$$\frac{\partial tke}{\partial t} + \frac{\partial \left(\overline{u}_j tke \right)}{\partial x_j} = \underbrace{\tau_{ij} \frac{\partial \overline{u}_i}{\partial x_j}}_{\text{I}} \underbrace{- \frac{g}{\theta_0} H_3^T}_{\text{II}} \underbrace{- \frac{\partial T_j + P_j}{\partial x_j}}_{\text{III}} \underbrace{- \varepsilon}_{\text{IV}}, \tag{A.4.12}$$

where term I is the shear production, II is the buoyancy production, III is the turbulent transport and redistribution by pressure, and IV is the dissipation. Then, term III and IV are parameterized

the following:

$$T_j + P_j = -c_e k_m \frac{\partial tke}{\partial x_j} \tag{A.4.13}$$

$$\varepsilon = c_\varepsilon \frac{tke^{3/2}}{\lambda}. \tag{A.4.14}$$

The equations above contain closure coefficients, which are determined empirically. Their values in the used EULAG configuration are based on Schumann (1991):

$$c_\varepsilon = 0.845,\ c_L = 0.845,\ c_m = 0.0856,\ c_h = 0.2038\, c_e = 0.2 \tag{A.4.15}$$

This TKE scheme is characterized by its ability to dynamically adapt to local flow conditions by taking into account the subgrid-scale TKE. Consequently, it can mitigate the overestimation of dissipation commonly associated with the Smagorinsky model (Smagorinsky, 1963), particularly in regions of strong shear or under stable stratification (Fröhlich, 2006).

A.5 Time Averaging

The analysis in this thesis focuses on temporal averages of the LES flow fields. Therefore, a recursive online time-averaging method is applied, following the approach of Fröhlich (2006). The mean value $\langle \Psi \rangle^{n+1}$ of a model variable Ψ at time step t_{n+1} is recursively computed as:

$$\langle \Psi \rangle^{n+1} = \alpha \cdot \Psi^{n+1} + (1-\alpha)\langle \Psi \rangle^{n} \tag{A.5.16}$$

$$\text{with} \quad \alpha = \frac{\Delta_t^{n+1}}{t_n - t_s}. \tag{A.5.17}$$

Here, t_n denotes the current time, t_s marks the start time of the averaging process, and Δ_t^{n+1} represents the integration time step.

Simulations with the realistic orography of the Matterhorn revealed that an adaptive integration time step, guided by the Courant-Friedrichs-Lewy (CFL) condition, is essential to prevent EULAG crashes. To evaluate the consistency of the recursive averaging method with regard to a constant and an adaptive integration time step, the behavior of the coefficient α and the time-averaged variable $\langle \Psi \rangle^{n+1}$ was analyzed over time, as shown in Fig. A.2.

As expected, the coefficient α fluctuates when an adaptive time step is applied but asymptotically approaches zero as t_n increases. Similar behaviour is observed for the case with a constant time step. While noticeable differences in the time-averaged field $\langle \Psi \rangle^{n+1}$ occur over shorter averaging periods, these differences decrease significantly.

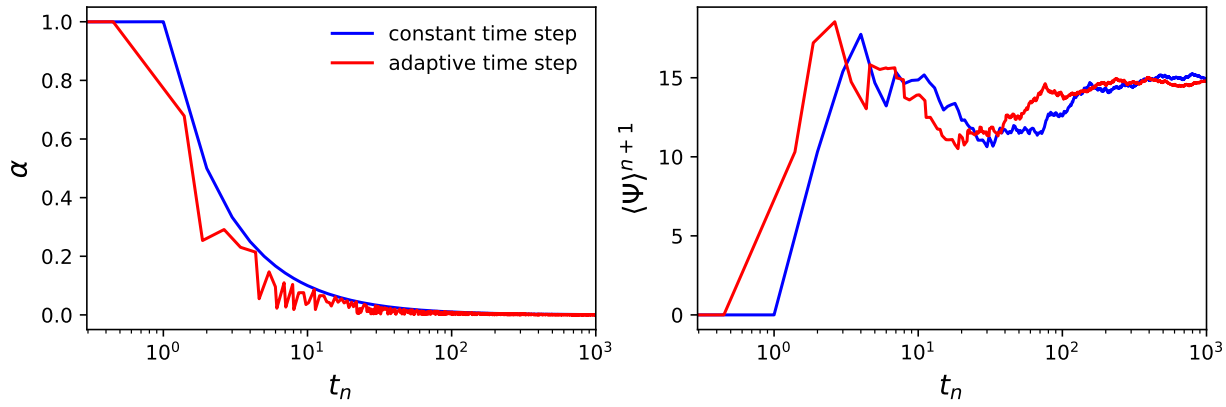

FIGURE A.2: Recursive time averaging based on Eq. A.5.16 for a constant time step $\Delta_t^{n+1} = 1$ s (blue) and an adaptive time step Δ_t^{n+1} in $(0.1, 1]$ (red).

References

Alcayaga, L. (2020). Filtering of pulsed lidar data using spatial information and a clustering algorithm. *Atmospheric Measurement Techniques*, 13(11), 6237–6254. https://doi.org/10.5194/amt-13-6237-2020

Ambaum, M. H. P. & Marshall, D. P. (2005). The effects of stratification on flow separation. *Journal of the Atmospheric Sciences*, 62(7), 2618 – 2625. https://doi.org/10.1175/JAS3485.1

Baines, P. G. (1995). *Topographic Effects in Stratified Flows*. Cambridge University Press.

Baines, P. G. & Hoinka, K. P. (1985). Stratified flow over two-dimensional topography in fluid of infinite depth: A laboratory simulation. *Journal of Atmospheric Sciences*, 42(15), 1614 – 1630. https://doi.org/10.1175/1520-0469(1985)042<1614:SFOTDT>2.0.CO;2

Berg, J., Reynolds, D., Quéno, L., Jonas, T., Lehning, M., & Mott, R. (2024). A seasonal snowpack model forced with dynamically downscaled forcing data resolves hydrologically relevant accumulation patters. *Frontiers in Earth Science*, 12(1393260). https://doi.org/10.3389/feart.2024.1393260

Cherukuru, N. W., Calhoun, R., Lehner, M., Hoch, S. W., & Whiteman, C. D. (2015). Instrument configuration for dual-Doppler lidar coplanar scans: METCRAX II. *Journal of Applied Remote Sensing*, 9(1), 096090. https://doi.org/10.1117/1.JRS.9.096090

Comola, F., Giometto, M. G., Salesky, S. T., Parlange, M. B., & Lehning, M. (2019). Preferential deposition of snow and dust over hills: Governing processes and relevant scales. *Journal of Geophysical Research: Atmospheres*, 124(14), 7951–7974. https://doi.org/https://doi.org/10.1029/2018JD029614

Connolly, A., Chow, F. K., & Hoch, S. W. (2021). Nested large-eddy simulations of the displacement of a cold-air pool by lee vortices. *Boundary-Layer Meteorology*, 178(1), 91–118. https://doi.org/10.1007/s10546-020-00561-6

De Wekker, S. F. J. & Kossmann, M. (2015). Convective boundary layer heights over mountainous terrain—a review of concepts. *Frontiers in Earth Science*, 3. https://doi.org/10.3389/feart.2015.00077

Deardorff, J. W. (1973). The Use of Subgrid Transport Equations in a Three-Dimensional Model of Atmospheric Turbulence. *Journal of Fluids Engineering*, 95(3), 429–438. https://doi.org/10.1115/1.3447047

Durran, D. (2003). Lee waves and mountain waves. *Encyclopedia of Atmospheric Sciences*, 1161–1169. Academic Press. https://doi.org/10.1016/B0-12-227090-8/00202-5

Duscha, C., Pálenik, J., Spengler, T., & Reuder, J. (2023). Observing atmospheric convection with dual-scanning lidars. *Atmospheric Measurement Techniques*, 16(21), 5103–5123. https://doi.org/10.5194/amt-16-5103-2023

Elliott, J. R. & Smolarkiewicz, P. K. (2002). Eddy resolving simulations of turbulent solar convection. *International Journal for Numerical Methods in Fluids*, 39(9), 855–864. https://doi.org/https://doi.org/10.1002/fld.333

Epifanio, C. C. & Rotunno, R. (2005). The dynamics of orographic wake formation in flows with upstream blocking. *Journal of the Atmospheric Sciences*, 62(9), 3127 – 3150. https://doi.org/10.1175/JAS3523.1

Ester, M., Kriegel, H.-P., Sander, J., & Xu, X. (1996). A density-based algorithm for discovering clusters in large spatial databases with noise. *Proceedings of the Second International Conference on Knowledge Discovery and Data Mining*, KDD'96, 226–231.

Fritts, D. C., Smith, R. B., Taylor, M. J., Doyle, J. D., Eckermann, S. D., Dörnbrack, A., Rapp, M., Williams, B. P., Pautet, P.-D., Bossert, K., Criddle, N. R., Reynolds, C. A., Reinecke, P. A., Uddstrom, M., Revell, M. J., Turner, R., Kaifler, B., Wagner, J. S., Mixa, T., Kruse, C. G., Nugent, A. D., Watson, C. D., Gisinger, S., Smith, S. M., Lieberman, R. S., Laughman, B., Moore, J. J., Brown, W. O., Haggerty, J. A., Rockwell, A., Stossmeister, G. J., Williams, S. F., Hernandez, G., Murphy, D. J., Klekociuk, A. R., Reid, I. M., & Ma, J. (2016). The deep propagating gravity wave experiment (deepwave): An airborne and ground-based exploration of gravity wave propagation and effects from their sources throughout the lower and middle atmosphere. *Bulletin of the American Meteorological Society*, 97(3), 425 – 453. https://doi.org/10.1175/BAMS-D-14-00269.1

Fröhlich, J., editor (2006). *Large Eddy Simulation turbulenter Strömungen*, volume 1. Teubner.

Geiger, R. (2013). *Das Klima der bodennahen Luftschicht: ein Lehrbuch der Mikroklimatologie*. Wiesbaden: Springer Vieweg.

Gerber, F., Lehning, M., Hoch, S. W., & Mott, R. (2017). A close-ridge small-scale atmospheric flow field and its influence on snow accumulation. *Journal of Geophysical Research: Atmospheres*, 122(15), 7737–7754. https://doi.org/10.1002/2016JD026258

Glickman, T. S., editor (2000). *Glossary of Meteorology* (2nd ed.). American Meteorological Society, 855 pp.

Goldstein, D., Handler, R., & Sirovich, L. (1993). Modeling a no-slip flow boundary with an external force field. *Journal of Computational Physics*, 105(2), 354–366. https://doi.org/https://doi.org/10.1006/jcph.1993.1081

Gryning, S.-E., Floors, R., Peña, A., Batchvarova, E., & Brümmer, B. (2016). Weibull wind-speed distribution parameters derived from a combination of wind-lidar and tall-mast measurements over land, coastal and marine sites. *Boundary-Layer Meteorology*, 159(2), 329–348. https://doi.org/10.1007/s10546-015-0113-x

Haller, G. (2005). An objective definition of a vortex. *Journal of Fluid Mechanics*, 525, 1–26. https://doi.org/10.1017/S0022112004002526

Hill, M., Calhoun, R., Fernando, H. J. S., Wieser, A., Dörnbrack, A., Weissmann, M., Mayr, G., & Newsom, R. (2010). Coplanar doppler lidar retrieval of rotors from t-rex. *Journal of the Atmospheric Sciences*, 67(3), 713 – 729. https://doi.org/10.1175/2009JAS3016.1

Hunt, J. C. R. & Snyder, W. H. (1980). Experiments on stably and neutrally stratified flow over a model three-dimensional hill. *Journal of Fluid Mechanics*, 96(4), 671–704. https://doi.org/10.1017/S0022112080002303

Hunter, J. D. (2007). Matplotlib: A 2D Graphics Environment. *Computing in Science and Engineering*, 9(3), 90–95. https://doi.org/10.1109/MCSE.2007.55

Jeong, J. & Hussain, F. (1995). On the identification of a vortex. *Journal of Fluid Mechanics*, 285, 69–94. https://doi.org/10.1017/S0022112095000462

Krishnamurthy, R., Choukulkar, A., Calhoun, R., Fine, J., Oliver, A., & Barr, K. (2013). Coherent doppler lidar for wind farm characterization. *Wind Energy*, 16(2), 189–206. https://doi.org/https://doi.org/10.1002/we.539

Kristianti, F., Dujardin, J., Gerber, F., Huwald, H., Hoch, S. W., & Lehning, M. (2023). Combining weather station data and short-term lidar deployment to estimate wind energy potential with machine learning: A case study from the swiss alps. *Boundary-Layer Meteorology*, 188(1), 185–208. https://doi.org/10.1007/s10546-023-00808-y

Kristianti, F., Gerber, F., Gonzàlez-Herrero, S., Dujardin, J., Huwald, H., Hoch, S. W., & Lehning, M. (2024). Influence of air flow features on alpine wind energy potential. *Frontiers in Energy Research*, 12. https://doi.org/10.3389/fenrg.2024.1379863

Kurowski, M. J., Grabowski, W. W., & Smolarkiewicz, P. K. (2014). Anelastic and compressible simulation of moist deep convection. *Journal of the Atmospheric Sciences*, 71(10), 3767 – 3787. https://doi.org/10.1175/JAS-D-14-0017.1

Kurowski, M. J., Grabowski, W. W., & Smolarkiewicz, P. K. (2015). Anelastic and compressible simulation of moist dynamics at planetary scales. *Journal of the Atmospheric Sciences*, 72(10), 3975 – 3995. https://doi.org/10.1175/JAS-D-15-0107.1

Lareau, N. P. & Clements, C. B. (2017). The mean and turbulent properties of a wildfire convective plume. *Journal of Applied Meteorology and Climatology*, 56(8), 2289 – 2299. https://doi.org/10.1175/JAMC-D-16-0384.1

Lehner, M., Whiteman, C. D., Hoch, S. W., Adler, B., & Kalthoff, N. (2019). Flow separation in the lee of a crater rim. *Boundary-Layer Meteorology*, 173(2), 263–287. https://doi.org/10.1007/s10546-019-00466-z

Lehning, M., Löwe, H., Ryser, M., & Raderschall, N. (2008). Inhomogeneous precipitation distribution and snow transport in steep terrain. *Water Resources Research*, 44(7). https://doi.org/https://doi.org/10.1029/2007WR006545

Lundquist, K. A., Chow, F. K., & Lundquist, J. K. (2012). An immersed boundary method enabling large-eddy simulations of flow over complex terrain in the wrf model. *Monthly Weather Review*, 140(12), 3936 – 3955. https://doi.org/10.1175/MWR-D-11-00311.1

Martinuzzi, R. J. & AbuOmar, M. (2003). Study of the flow around surface-mounted pyramids. *Experiments in Fluids*, 34(3), 379–389. https://doi.org/10.1007/s00348-002-0573-x

Mittal, R. & Iaccarino, G. (2005). Immersed boundary methods. *Annual Review of Fluid Mechanics*, 37(1), 239–261. https://doi.org/10.1146/annurev.fluid.37.061903.175743

Musy, M., Jacquenot, G., Dalmasso, G., neoglez, de Bruin, R., Pollack, A., Claudi, F., Badger, C., icemtel, Sullivan, B., Hrisca, D., Volpatto, D., Schlömer, N., Zhou, Z.-Q., & ilorevilo (2020). *marcomusy/vedo: 2020.4.2*. https://doi.org/10.5281/zenodo.4287635

Newsom, R. K., Berg, L. K., Shaw, W. J., & Fischer, M. L. (2015). Turbine-scale wind field measurements using dual-doppler lidar. *Wind Energy*, 18(2), 219–235. https://doi.org/https://doi.org/10.1002/we.1691

Prestel, I. (2018). *Dynamik von Bannerwolken: Theoriebildung und Simulationen mit realistischer Orografie*. Johannes Gutenberg-Universität Mainz. https://doi.org/http://doi.org/10.25358/openscience-2658

Prestel, I. & Wirth, V. (2016). What flow conditions are conducive to banner cloud formation? *Journal of the Atmospheric Sciences*, 73(6), 2385 – 2402. https://doi.org/10.1175/JAS-D-15-0319.1

Prusa, J. M., Smolarkiewicz, P. K., & Wyszogrodzki, A. A. (2008). Eulag, a computational model for multiscale flows. *Computers & Fluids*, 37(9), 1193–1207. https://doi.org/https://doi.org/10.1016/j.compfluid.2007.12.001

Reinert, D. & Wirth, V. (2009). A new large-eddy simulation model for simulating air flow and warm clouds above highly complex terrain. part ii: The moist model and its application to banner clouds. *Boundary-Layer Meteorology*, 133(1), 113–136. https://doi.org/10.1007/s10546-009-9419-x

Reynolds, D., Haugeneder, M., Lehning, M., & Mott, R. (2024a). Intermediate complexity atmospheric modeling in complex terrain: is it right? *Frontiers in Earth Science*, 12. https://doi.org/10.3389/feart.2024.1388416

Reynolds, D., Quéno, L., Lehning, M., Jafari, M., Berg, J., Jonas, T., Haugeneder, M., & Mott, R. (2024b). Seasonal snow–atmosphere modeling: let's do it. *The Cryosphere*, 18(9), 4315–4333. https://doi.org/10.5194/tc-18-4315-2024

Roe, G. H. (2005). Orographic precipitation. *Annual Review of Earth and Planetary Sciences*, 33(Volume 33, 2005), 645–671. https://doi.org/https://doi.org/10.1146/annurev.earth.33.092203.122541

Rotunno, R., Grubišić, V., & Smolarkiewicz, P. K. (1999). Vorticity and potential vorticity in mountain wakes. *Journal of the Atmospheric Sciences*, 56(16), 2796 – 2810. https://doi.org/10.1175/1520-0469(1999)056<2796:VAPVIM>2.0.CO;2

Rotunno, R. & Smolarkiewicz, P. K. (1991). Further results on lee vortices in low-froude-number flow. *Journal of Atmospheric Sciences*, 48(19), 2204 – 2211. https://doi.org/10.1175/1520-0469(1991)048<2204:FROLVI>2.0.CO;2

Schappert, S. & Wirth, V. (2015). Origin and flow history of air parcels in orographic banner clouds. *Journal of the Atmospheric Sciences*, 72(9), 3389 – 3403. https://doi.org/10.1175/JAS-D-14-0300.1

Schnur, R. (2022). *pygranite*. https://github.com/catheart97/pygranite

Schumann, U. (1991). Subgrid length-scales for large-eddy simulation of stratified turbulence. *Theoretical and Computational Fluid Dynamics*, 2(5), 279–290.

Schween, J. H., Kuettner, J., Reinert, D., Reuder, J., & Wirth, V. (2007). Definition of "banner clouds" based on time lapse movies. *Atmospheric Chemistry and Physics*, 7(8), 2047–2055. https://doi.org/10.5194/acp-7-2047-2007

Scorer, R. S. (1955). Theory of airflow over mountains: Iv-separation of flow from the surface. *Quarterly Journal of the Royal Meteorological Society*, 81(349), 340–350. https://doi.org/https://doi.org/10.1002/qj.49708134905

Serafin, S., Adler, B., Cuxart, J., De Wekker, S. F. J., Gohm, A., Grisogono, B., Kalthoff, N., Kirshbaum, D. J., Rotach, M. W., Schmidli, J., Stiperski, I., Večenaj, Ž., & Zardi, D. (2018). Exchange processes in the atmospheric boundary layer over mountainous terrain. *Atmosphere*, 9(3). https://doi.org/10.3390/atmos9030102

Smagorinsky, J. (1963). General circulation experiments with the primitive equations: I. the basic experiment. *Monthly Weather Review*, 91(3), 99 – 164. https://doi.org/10.1175/1520-0493(1963)091<0099:GCEWTP>2.3.CO;2

Smith, R. B. (1979). The influence of mountains on the atmosphere. volume 21 of *Advances in Geophysics*, 87–230. Elsevier. https://doi.org/https://doi.org/10.1016/S0065-2687(08)60262-9

Smith, R. B. (1989). Comment on "low froude number flow past three-dimensional obstacles. part i: Baroclinically generated lee vortices". *Journal of Atmospheric Sciences*, 46(23), 3611 – 3613. https://doi.org/10.1175/1520-0469(1989)046<3611:COFNFP>2.0.CO;2

Smolarkiewicz, P. K. & Charbonneau, P. (2013). Eulag, a computational model for multiscale flows: An mhd extension. *Journal of Computational Physics*, 236, 608–623. https://doi.org/https://doi.org/10.1016/j.jcp.2012.11.008

Smolarkiewicz, P. K., Deconinck, W., Hamrud, M., Kühnlein, C., Mozdzynski, G., Szmelter, J., & Wedi, N. P. (2016). A finite-volume module for simulating global all-scale atmospheric flows. *Journal of Computational Physics*, 314, 287–304. https://doi.org/https://doi.org/10.1016/j.jcp.2016.03.015

Smolarkiewicz, P. K., Kühnlein, C., & Wedi, N. P. (2014). A consistent framework for discrete integrations of soundproof and compressible pdes of atmospheric dynamics. *Journal of Computational Physics*, 263, 185–205. https://doi.org/https://doi.org/10.1016/j.jcp.2014.01.031

Smolarkiewicz, P. K. & Margolin, L. G. (1997). On forward-in-time differencing for fluids: an eulerian/semi-lagrangian non-hydrostatic model for stratified flows. *Atmosphere-Ocean*, 35(sup1), 127–152. https://doi.org/10.1080/07055900.1997.9687345

Smolarkiewicz, P. K. & Margolin, L. G. (1998). Mpdata: A finite-difference solver for geophysical flows. *Journal of Computational Physics*, 140(2), 459–480. https://doi.org/https://doi.org/10.1006/jcph.1998.5901

Smolarkiewicz, P. K., Margolin, L. G., & Wyszogrodzki, A. A. (2001). A class of nonhydrostatic global models. *Journal of the Atmospheric Sciences*, 58(4), 349 – 364. https://doi.org/10.1175/1520-0469(2001)058<0349:ACONGM>2.0.CO;2

Smolarkiewicz, P. K. & Rotunno, R. (1989). Low froude number flow past three-dimensional obstacles. part i: Baroclinically generated lee vortices. *Journal of Atmospheric Sciences*, 46(8), 1154 – 1164. https://doi.org/10.1175/1520-0469(1989)046<1154:LFNFPT>2.0.CO;2

Smolarkiewicz, P. K., Sharman, R., Weil, J., Perry, S. G., Heist, D., & Bowker, G. (2007). Building resolving large-eddy simulations and comparison with wind tunnel experiments. *Journal of Computational Physics*, 227(1), 633–653. https://doi.org/https://doi.org/10.1016/j.jcp.2007.08.005

Sogachev, A., Üllar Rannik, & Vesala, T. (2004). Flux footprints over complex terrain covered by heterogeneous forest. *Agricultural and Forest Meteorology*, 127(3), 143–158. https://doi.org/https://doi.org/10.1016/j.agrformet.2004.07.010. Flux and Concentration Footprints

Sorbjan, Z. (1996). Numerical study of penetrative and "solid lid" nonpenetrative convective boundary layers. *Journal of Atmospheric Sciences*, 53(1), 101 – 112. https://doi.org/10.1175/1520-0469(1996)053<0101:NSOPAL>2.0.CO;2

Stull, R. B., editor (1988). *An introduction to boundary layer meteorology* (1 ed.), volume 13. Kluwer Academic Publishers. https://doi.org/https://doi.org/10.1007/978-94-009-3027-8

swisstopo (2017). *Dhm25*. https://www.swisstopo.admin.ch/de/geodata/height/dhm25.html

Tarquini, S., Isola, I., Favalli, M., Battistini, A., & Dotta., G. (2023). *Tinitaly, a digital elevation model of italy with a 10 meters cell size (version 1.1)*. https://doi.org/https://doi.org/10.13127/tinitaly/1.1

Teixeira, M. A. C., Kirshbaum, D. J., Ólafsson, H., Sheridan, P. F., & Stiperski, I. (2016). Editorial: The atmosphere over mountainous regions. *Frontiers in Earth Science*, 4. https://doi.org/10.3389/feart.2016.00084

Thomas, M. L. & Wirth, V. (2023). Sensitivity of banner cloud formation to orography and the ambient atmosphere: Transition from idealized to more realistic scenarios. *Journal of the Atmospheric Sciences*, 80(11), 2653 – 2668. https://doi.org/10.1175/JAS-D-23-0106.1

van Schaik, B., Huwald, H., & Lehning, M. (2025). Resolving three-dimensional wind velocity fields with sequential wind-doppler lidar for wind energy in the complex terrain - gotthard pass, switzerland [version 1; peer review: 1 approved with reservations, 2 not approved]. *Open Research Europe*, 5(9). https://doi.org/10.12688/openreseurope.19095.1

Voigt, M. & Wirth, V. (2013). Mechanisms of banner cloud formation. *Journal of the Atmospheric Sciences*, 70(11), 3631 – 3640. https://doi.org/10.1175/JAS-D-12-0353.1

Waite, M. L. & Smolarkiewicz, P. K. (2008). Instability and breakdown of a vertical vortex pair in a strongly stratified fluid. *Journal of Fluid Mechanics*, 606, 239–273. https://doi.org/10.1017/S0022112008001912

Wang, Y., Hocut, C. M., Hoch, S. W., Creegan, E., Fernando, H. J. S., Whiteman, C. D., Felton, M., & Huynh, G. (2016). Triple Doppler wind lidar observations during the mountain terrain atmospheric modeling and observations field campaign. *Journal of Applied Remote Sensing*, 10(2), 026015. https://doi.org/10.1117/1.JRS.10.026015

Whiteman, C. D. (2000). *Mountain Meteorology: Fundamentals and Applications*. Oxford University Press. https://doi.org/10.1093/oso/9780195132717.001.0001

Whiteman, C. D., Lehner, M., Hoch, S. W., Adler, B., Kalthoff, N., & Haiden, T. (2018). Katabatically driven cold air intrusions into a basin atmosphere. *Journal of Applied Meteorology and Climatology*, 57(2), 435 – 455. https://doi.org/10.1175/JAMC-D-17-0131.1

Wirth, V., Bubel, P., Eichhorn, J., Schömer, E., Kremer, T., Erbes, R., Schappert, S., & Prestel, I. (2020). The role of wind speed and wind shear for banner cloud formation. *Journal of the Atmospheric Sciences*, 77(4), 1199 – 1212. https://doi.org/10.1175/JAS-D-18-0354.1

Wirth, V., Kristen, M., Leschner, M., Reuder, J., & Schween, J. H. (2012). Banner clouds observed at mount zugspitze. *Atmospheric Chemistry and Physics*, 12(8), 3611–3625. https://doi.org/10.5194/acp-12-3611-2012

Wood, N. (1995). The onset of separation in neutral, turbulent flow over hills. *Boundary-Layer Meteorology*, 76(1), 137–164. https://doi.org/10.1007/BF00710894